NANOSTRUCTURE FORMATION OF INORGANIC MATERIALS FROM THE SELF-ASSEMBLY OF HIGHLY AMPHIPHILIC BLOCK COPOLYMERS

A dissertation

Presented to the Faculty of the Graduate School

of Cornell University

In Partial Fulfillment of the Requirements for the Degree of

Doctor of Philosophy

by

Ju Ho Song

August 2012

© 2012 Ju Ho Song

NANOSTRUCTURE FORMATION OF INORGANIC MATERIALS FROM THE SELF-ASSEMBLY OF HIGHLY AMPHIPHILIC BLOCK COPOLYMERS

Ju Ho Song, Ph. D.

Cornell University 2012

High performance catalysts or energy devices such as solar cells and batteries which involve reactions and transport problems require nanostructured functional materials that are highly ordered mesoporous and crystalline materials. The self-assembly based structure direction of functional inorganic materials by block copolymers (BCPs) is a promising route because it combines mesoporosity at the 2-50 nm length scale, high surface areas and full control over morphology. This work explored solubility design guidelines that facilitate the coassembly of titania and poly(isoprene-*b*-ethylene oxide) (PI-*b*-PEO) which is a highly amphiphilic block copolymer. This approach enabled the fabrication of highly ordered crystalline titania. The pore size control of mesoporous crystalline titania was also accomplished by applying different molecular weight PI-*b*-PEOs, and the highly ordered titania with the largest cylindrical pores (>30 nm) was reported without the use of pore-expanders.

Nanostructured titania membranes were developed for water purification applications based on the knowledge from the previous part because inorganic membranes have superior thermal and chemical stabilities over polymer membranes. The mesoporous titania membranes with different pore size were successfully fabricated on porous disc substrates from both large and small molar mass PI-*b*-PEOs

and presented an excellent molecular weight cut-off performances with high permeability, which would provide a huge potential to be applied in many ultrafiltration areas due to its self-cleaning characteristics from the photocatalytic activity.

Finally, an ABC triblock terpolymer system was studied as an extension of the BCP self-assembly based structure direction of inorganic materials because these terpolymers allow wider composition windows for ordered network structures that have advantages such as 3-D connectivity and enhanced mechanical properties. In this work, the ternary morphology map of PI-*b*-PS-*b*-PEO and aluminisolicate sols was successfully constructed, which reveals 10 distinct morphologies along with particularly wide composition windows (2-13 vol%) for ordered network morphologies. This morphology map could be used as a model to predict the structure direction of other functional inorganic materials and a highly ordered network titania composite with core-shell double gyroid structure (cs-G^D) was demonstrated as an example.

BIOGRAPHICAL SKETCH

Ju Ho Song entered Pohang University of Science and Technology (Postech) in Pohang, South Korea in 1991 to pursue a Bachelor of Science degree in Chemical Engineering. Ju Ho started his professional career as a chemical engineer at GS Caltex Corporation, South Korea after he received a Master of Science degree in Chemical Engineering, Postech in 1997. He worked in the oil refinery plant where he operated a crude distillation unit for the first two years. He married his wife, Hwa Yeong Kim in October, 1998 and his son, Jeong Hun and daughter, Ji-Eun were born in 2000 and 2002. After Ju Ho spent about a year in the petrochemical plant, he moved to the process technology team at the company where he worked for about 5 years on the catalysts of the heavy oil upgrading processes. He participated in the catalyst reformulation project in collaboration with the catalyst suppliers and achieved a huge profit increase after applying the optimized catalyst to the plant. Based upon this achievement, the company decided to support him for the Ph. D. program and he moved to Ithaca, NY with his family to join the School of Chemical and Biomolecular Engineering at Cornell University in 2007. In July of 2012, he passed his B-exam and moved toward completion of his Ph. D. by the summer of 2012.

To my wife, Hwa Yeong, for her support and understanding

ACKNOWLEDGEMENTS

First and foremost, I would like to thank my advisor Ulrich Wiesner for his warm and insightful guidance. His continuing devotion and innovative ideas in the research have been truly inspiring and motivating.

I would also like to thank Professor Frank DiSalvo. He has always been very supportive and gave some helpful suggestions. I learned a lot about solid state chemistry thanks to him. Professor Yong Joo was the one who I have discussed with academically and personally and I truly appreciate that.

I would not be able to accomplish what I wanted without the people of the Wiesner and DiSalvo research groups. In particular, I would like to thank Dr. Morgan Stefik, Rachel Dorin and Hiroaki Sai for the close collaborations. And I also have to acknowledge the energy subgroup people, Kwan Tan, Spencer Robbins and Joerg Werner for the cooperation and also Zihui Li and Kahyun Hur for many valuable discussions we had for the past years.

I am sincerely grateful to GS Caltex Corporation and Dr. Dong-Soo Hur for the support of my Ph. D. program.

Last but not least, I thank my wife and my children who love and support me in every way.

TABLE OF CONTENTS

CHAPTER 1

INTRODUCTION

High performance energy devices such as fuel cells, solar cells and batteries which involve reactions and transport problems require nanostructured functional materials that are highly ordered mesoporous and crystalline materials. The self-assembly based structure direction of functional inorganic materials by block copolymers (BCPs) is a promising route to energy devices because it combines mesoporosity at the 2-50 nm length scale, high surface areas and full control over morphology. Titania is a particularly interesting transition metal oxide, and it has been applied in many areas such as photocatalysis, membranes, optics, photovoltaics and so forth. Although block copolymer based mesoporous and crystalline titania materials have been studied for more than a decade, they are mostly limited to water and alcohol soluble polymers which only give the structures of small dimensions and few morphologies. This work explored solubility design guidelines that facilitate the coassembly with poly(isoprene-*b*-ethylene oxide) (PI-*b*-PEO) which is a highly amphiphilic block copolymer. This approach along with the CASH (combined assembly of soft and hard chemistries) method enabled the fabrication of highly ordered crystalline titania with an inverse hexagonally arranged cylindrical morphology. The pore size control of mesoporous crystalline titania was also accomplished by applying different molecular weight PI-*b*-PEOs, and the highly ordered and crystalline titania with the largest cylindrical pores (>30 nm) was reported without the use of pore-expanders.

In chapter 2 of this dissertation, nanostructured titania thin films were

developed for water purification membrane applications based on the knowledge from the previous part about PI-*b*-PEO and titania sol-gel chemistry for nanostructure formation along with the pore size tunability because inorganic membranes have advantages such as superior thermal and chemical stabilities over polymer membranes. The mesoporous titania membranes with different pore size were successfully fabricated on porous disc substrates from both large and small molar mass PI-*b*-PEOs and presented an excellent molecular weight cut-off performances with high permeability, which would provide a huge potential to be applied in many ultrafiltration areas due to its self-cleaning characteristics from the photocatalytic activity.

The next part explored the mesoporous mixed oxide formation of $Ti_{1-x}W_xO_2$ structure-directed from PI-b-PEO combined with a two-step heat processing approach. $Ti_{1-x}W_xO_2$ has been investigated as an alternative to conventional carbon materials for the catalyst support in proton-exchange membrane (PEM) fuel cells. Although as-made hybrids and amorphous metal oxide/carbon composites were well ordered, the second higher temperature step caused problems such as collapse of mesoporosity and segregation of metal oxide crystalline phases. To avoid these problems, two suggestions were made, i.e. (1) milder reduction conditions to prevent excessive diffusion of metal oxides and (2) a non-chlorine containing system as even trace amounts of chlorine promote the transport of tungsten causing phase segregation.

Finally, an ABC triblock terpolymer system was studied as an extension of the BCP self-assembly based structure direction of inorganic materials. ABC triblock terpolymers have been previously reported to enable a greater variety of morphologies

than simple AB diblock copolymers and allow wider composition windows for ordered network structures that have advantages such as 3-D connectivity and enhanced mechanical properties. In this work, the morphology space of inorganic nanocomposites was investigated comprehensively and systematically using poly(isoprene-*b*-styrene-*b*-ethylene oxide) (ISO) and aluminosilicate sol nanoparticles as a model system. Over eighty nanocomposites with different compositions were synthesized and the morphologies were characterized by a combination of small-angle X-ray scattering (SAXS) and transmission electron microscopy (TEM) measurements. The ternary morphology map of ISO and aluminisolicate sols was successfully constructed, which reveals 10 distinct morphologies. In particular, this triblock terpolymer was able to provide wide composition windows (2-13 vol%) for ordered network morphologies, allowing these network structures to be more easily accessible experimentally. This morphology map could be used as a model to predict the structure direction of other functional inorganic materials and a highly ordered network titania composite with core-shell double gyroid structure (cs-G^D) was demonstrated as an example.

CHAPTER 2

ORDERED MESOPOROUS TITANIA FROM HIGHLY AMPHIPHILIC BLOCK COPOLYMERS: TUNED SOLUTION CONDITIONS ENABLE HIGHLY ORDERED MORPHOLOGIES AND ULTRA-LARGE MESOPORES

Abstract

Crystalline transition metal oxides with controlled mesopore architectures are in increasing demand to enhance the performance of energy conversion and storage devices. Solvent evaporation induced block copolymer coassembly routes to achieve ordered mesoporous and crystalline titania have been studied for more than a decade, but have thus far mostly been limited to water and alcohol dispersible polymers. This constraint has limited the demonstrated structures to have small dimensions and few morphologies. We present solubility design guidelines that facilitate coassembly with highly amphiphilic block copolymers, enabling the formation of ordered structures with diverse length scales (d_{10}=13.8-63.0 nm) and bulk-type morphologies. Thus highly ordered and crystalline titania with the largest reported cylindrical pores (d=32.3 nm) was demonstrated for such a coassembly approach without the use of pore-expanders. Furthermore, the use of an ABC triblock terpolymer system lead to a 3D ordered network morphology. In all cases, subsequent calcination treatments, such as the CASH procedure, enabled the formation of highly crystalline mesoporous materials while preserving the mesostructure.

Introduction

Over the past two decades significant advances have been made in the fabrication of

ordered inorganic materials with organic structure directing agents (SDA). Typically amphiphilic structure directing agents are used where a selective interaction, e.g. driven by electrostatics or or hydrogen bonding, leads to the selective association of hydrophilic inorganic entities with the hydrophilic portion of the SDA; at the same time the hydrophobic portion of the SDA phase separates from the hydrophilic components with nanoscale periodicity. Under certain controlled conditions the free energy balance of the inorganic-SDA coassembly leads to the equilibration of highly ordered nanoscale domains. The first example of such an approach utilized a surfactant to swell the spacing between ordered kanemite sheets in 1990[1]. This approach was then greatly expanded to enable the assembly of other silicate materials with multiple ordered morphologies by utilizing micellar surfactant assemblies[2].

Increasing efforts have focused on the nanostructure control of transitional metal oxides which have a diverse range of (photo)catalytic, transport (electron/ion), electronic (insulator/semiconductor/conductor), and optical properties. Indeed, transition metal oxide nanostructures are of great interest for numerous applications including, e.g., battery, supercapacitor, dye-sensitized solar cell, fuel cell, and electrochromic devices[3-8]. The controlled coassembly of transition metal oxides with SDAs is more difficult than silicates due to the multiple stable coordination states and much greater chemical reactivity (e.g. hydrolysis of $Ti(OR)_4$ is 10^5 faster than $Si(OR)_4$)[9]. Hydrolytic sol-gel routes were typically employed under acidic conditions that promote hydrolysis and severely slow the condensation reactions to allow time for coassembly with the SDA before gelation. Chelating ligands and non-hydrolytic sol-gel approaches have also been employed to slow these reaction rates.

Among the many transition metal oxides, titania is one of the most common one due to its use in diverse applications including all of those listed above. Although other metal oxides were first accomplished[10], similar methodologies later yielded ordered titania nanostructures[11]. Often the SDAs were removed from such hybrid materials to yield micro/mesoporous (IUPAC pore-size naming convention[12, 13]) materials preserving the ordered inorganic morphology. The pore sizes in surfactant based materials were typically ~1-5 nm due to their small molar mass (~150-350 g/mol). This limited range of pore sizes was expanded up to ~7 nm ordered pores and up to 12 nm irregular pores by swelling the hydrophobic domains with hydrophobic "pore-expanding" molecules[14].

Amphiphilic block copolymers circumvent this feature size limitation with larger SDA molar masses (~1,000-70,000 g/mol). Most block copolymer SDAs utilize a non-ionic poly(ethylene oxide) block to coordinate with the inorganic species[15, 16]. Block copolymers were first applied towards structure directing ordered silicates[17, 18] and were then adapted to many transition metal oxides, including titania[19]. Pluronic poly(ethylene oxide-*b*-propylene oxide-*b*-ethylene oxide), (PEO-b-PPO-PEO)s are commercially available and thus commonly used polymers of relatively low molar mass, ~2,000-13,000 g/mol[20] (Table 2.1). It follows that the resulting ordered oxide structures typically had 4-7 nm pores which were only slightly larger than those obtained from conventional surfactants. Similar to surfactants, larger pores became accessible with disordered films[21] or when pore expanders were added[22].

Many applications utilizing transition metal oxides require the electronic or catalytic properties of specific crystal structures. Thus significant effort has been

turned towards crystallization heat treatments of the amorphous transition metal oxide structures that typically result from hydrolytic sol-gel processes. Such heat treatments of titania films structure-directed with Pluronics were typically limited to low temperatures which resulted in anatase crystallites embedded in amorphous walls[19]. Although Pluronic SDAs can lead to highly crystalline ordered titania nanostructures when supported thin films were calcined, there remains a general challenge to achieve highly crystalline and ordered bulk films[23-25]. Successful crystallization requires that the amorphous oxide particles are well interconnected and that the resulting crystallite size is similar to or smaller than the wall thickness.

An alternative polymeric SDA called KLE was utilized to yield thicker walls that enabled higher temperature treatments and larger crystallites with less amorphous content. For example, KLE led to mesoporous titania thin films with 10 nm pores stable up to 600 °C[26, 27]. KLE polymers, based on hydrogenated poly(butadiene-*b*-ethylene oxide), (PB-b-PEO), have similar molar masses to Pluronics, but have a much larger Flory Hugins monomer-monomer interaction parameter, χ. The resulting increased enthalpic penalty for A-B interfacial area of KLE polymers diminishes the entropic penalty for chain stretching leading to slightly larger mesostructures than Pluronic polymers. However, only spherical micellar morphologies have been demonstrated with KLE SDAs thus far[26-28]. There are indeed numerous reports of coassembled titania with the mentioned SDAs[5, 11, 19, 21-53].

Extension to larger structures and/or novel ordered morphologies suggests transitioning to new structure directing agents. In fact this is where ultimately the biggest benefit for such approaches may come from, i.e. from the combination of

creative polymer chemistry with inorganic/solid-state chemistry. However, most polymers are hydrophobic and thus immiscible with the typically used alcohol and water based sol-gel processes (in fact water and alcohol are commonly used as precipitation agents for polymers). For example, in the past the coassembly of titania with poly(styrene-*b*-ethylene oxide) (PS-b-PEO) in the presence of such poor solvents lead to either disordered structures[50, 54, 55] or to ordered macroporous emulsions[56]. The formation of equilibrated bulk morphologies based on block copolymer thermodynamics requires that the polymer does not become kinetically trapped in a selective-solution morphology such as spherical micelles. As another example, large ~30,000 g/mol and highly amphiphilic poly(isoprene-*b*-ethylene oxide)s (PI-*b*-PEO) with majority PI blocks were recently used to structure direct inverse-hexagonal niobium oxide and worm-like titania nanostructures[57]. The use of non-hydrolytic sol-gel processes and organic solvents were key to enabling solvent evaporation induced coassembly with such hydrophobic polymers. In the same study, the so called combined assembly by soft and hard (CASH) chemistries approach enabled oxide crystallization without collapse by *in-situ* creating a hard template from the carbon resulting from polymer pyrolysis in inert atmosphere. The carbon was subsequently removed yielding crystalline oxide nanostructures with large ~24 nm pores and 10 nm thick walls. While such PI-*b*-PEO SDAs have demonstrated over 8 different morphologies in aluminosilicates[58] including bicontinuous networked structures[59-62], such morphological diversity in titania nanostructures is still lacking. Finally, an emerging trend to achieve ordered network morphologies is to take advantage of ABC triblock terpolymer SDAs which have large composition windows

for network coassembly[63]. Here again, however, full use of the morphological diversity of triblock terpolymer self-assembly to direct transition metal oxide nanostructures, including large pore mesoporous materials, would require better control of the structure formation in solvent evaporation induced self-assembly.

From all of the above it is apparent that there is a need to develop a better understanding of the thermodynamics that controls (transition metal) oxide structure formation directed from large molar mass SDAs and various solvents. In particular, for the general practice it would be desirable to have quantitative, or at least semi-quantitative guidelines for how to best conduct experiments, which could replace chemical intuition-based trial and error. To this end here, we provide a framework to semi-quantitatively describe the solvent evaporation induced coassembly of titania into ordered bulk morphologies using highly amphiphilic block copolymers over a broad range of molecular weights. This framework, which is based on solubility parameters, provides experimental guidelines to avoid kinetically trapped solution structures (such as spherical micelles) thereby enabling the fine-tuning of titania nanostructure and pore size. This semi-quantitative approach allowed us to achieve a highly ordered crystalline titania structure with the largest reported cylindrical mesopores without the use of pore-expanding agents to date. The extension of this approach away from simple AB diblock copolymer to ABC triblock terpolymer SDA based titania with ordered network nanostructures suggests that this framework may be generalized to many new SDAs.

Experimental Procedures

Reagents.

Tetrahydrofuran (HPLC grade, J.T. Baker) was stored over activated 3 Å molecular sieves until use, or anhydrous tetrahydrofuran (>99.9%, Aldrich) was used as received. Titanium isopropoxide (97%, Aldrich) and concentrated hydrochloric acid (37wt% ACS grade, BDH Aristar) were used as received. Block copolymers were prepared by anionic polymerization using reported procedures[64, 65]. Poly(isoprene-*b*-ethylene oxide)s (PI-*b*-PEO) were synthesized with different molar masses from 7 to 92 kg/mol. They will be referred to in the following as IOXK, with X denoting the polymer molar mass.. Characterization results are summarized in Table 2.2. All polymers showed narrow molar mass distributions with PDIs (polydispersity index) less than 1.11. Poly(isoprene-*b*-styrene-*b*-ethylene oxide) (ISO1) was synthesized as described elsewhere [63] with molar mass of 53.4 kg/mol with 14.6 kg/mol of PI, 29.0 kg/mol of PS, and 9.8 kg/mol of PEO and a PDI of 1.05.

Hybrid synthesis.

Block copolymers were dissolved in THF with stirring for at least 1 hour. Hydrochloric acid was then added to the polymer solution followed by titanium isopropoxide. The resulting orange to red solution was stirred for 24 hrs during which the solution became slightly yellow to clear. The solution was cast in an 8 cm teflon dish which was placed within a glass dish on a hotplate to slow the loss of HCl due to reaction with the steel hotplate surface. This assembly was then covered with a glass hemisphere to slow evaporation and limit exposure to ambient humidity. The hot plate was set to 50 °C creating an effective casting temperature of ~40 °C. After 24 hrs of

drying, the films were moved to an oven set to 100 °C for a minimum of 3 days to enhance the condensation reaction. The films were then subjected to calcination heat treatments to crystallize the titania. The crystallization heat treatments were performed either in air to oxidatively remove the polymer or in nitrogen to convert the polymer into a carbonaceous framework using the CASH approach, *vide supra*. The inverse hexagonal hybrids were heated to 700 °C and the networked hybrids were heated to 400 °C. The carbon residue in some composites was subsequently removed by heating to 450 °C in air for at least 1 hour. All heat treatments utilized a 1-5 °C/min heating ramp rate with a 1-4 hour hold followed by natural furnace cooling to room temperature.

As-made samples prepared with IO28K were named IO28K-hx where x was the wt% of water in the THF solution prior to addition of the titanium isopropoxide. These casting solutions were all prepared with 50 mg of IO28K, 0.119 mL HCl(aq), 0.371 mL titanium(IV) isopropoxide, and a specific quantity of THF for a given x wt% water. Thus 2.44, 3.28, 4.97, and 9.27 mL of THF were used to prepare samples IO28K-h4, IO28K-h3, IO28K-h2, and IO28K-h1 with 4.0, 3.0, 2.0 and 1.08 wt.% water, respectively. Please note that the molar ratios for all recipes had $Ti:H_2O:HCl=1.0:4.0:1.16$ which is the minimum water content for complete hydrolysis of the titanium alkoxide.

For pore size control experiments, the hybrids from different molar mass PI-*b*-PEOs were synthesized as follows. 50 mg of PI-*b*-PEO was dissolved in 8 ml of THF with stirring for about 1 hour. A titanium-containing sol was prepared separately by the addition of 0.4 ml titanium(IV) isopropoxide to 0.129 ml hydrochloric acid (37%)

under vigorous stirring followed by addition of 2 ml THF after 5 min stirring. After another 5 min, the sol was added to the polymer solution and subsequently stirred for an hour. Then the films were cast and annealed as described before.

Hybrids from ISO1 were prepared similarly. 75 mg of ISO1 was dissolved in 2.9 mL of dry THF with stirring for at least 1 hr. A dilute sol stock solution was prepared to enable accurate addition of a small quantity of titania: 5 mL of titanium isopropoxide was added to a quickly stirred vial containing 1.6 mL of concentrated HCl(aq). The vial was closed after combining alkoxide with acid and was left to stir for 5 min before 10 mL of dry THF was added to dilute the sol (orange color) and left to stir for an additional 2 min. A syringe was used to immediately measure 0.388 mL of the dilute sol stock solution and the aliquot was added directly to the stirred polymer solution. This combined solution was left to stir for at least 30 min and was then cast as previously described for the IO28K-hx samples. After 24 hrs of casting the film was moved to an oven set to 100 °C for 3 days to enhance the condensation reaction. Portions of this film were calcined under different temperature and atmospheric conditions to optimize the crystallization process while preserving the ordered mesostructure. Samples ISO1-N_2 and ISO1-air were both prepared directly from sample ISO1- TiO_2 by heating at 1 °C/min to 400 °C with a 1 hr hold followed by natural furnace cooling in either N_2 or air, respectively.

Characterization

TEM. Ultrathin ~70 nm sections were prepared with wet, cryo microtoming using a Leica UC7/FC7 cryo-ultramicrotome. Sections were cut at -55 °C onto a 60:40

dimethylsulfoxide : water solution and then transferred to bare copper grids. A FEI Tecnai T12 twin transmission electron microscope was operated at 120 kV for microscopic inspection of the ultrathin sections. A Gatan Orius dual-scan CCD was used for image acquisition.

SEM. A LEO 1550 SEM with a field emission source was utilized to acquire images of calcined samples using an accelerating voltage of 2 kV and an in-lens secondary electron detector.

SAXS. Small-angle x-ray scattering (SAXS) patterns of samples were obtained at Cornell High Energy Synchrotron Source (CHESS) G1 station with a beam energy of 9 keV as well as at a home-built Rigaku RU300 CuKα rotating anode beamline. The details of both SAXS beamline configurations are described elsewhere[60]. For acquiring time-resolved SAXS patterns at CHESS G1 station, portions of films were transferred from Teflon dishes to 1.0 mm glass capillaries or on a Kapton tape immediately before the measurements. Degree of solvent evaporation at each time point was estimated by measuring the weight of the film in the dish. Acquired 2D patterns were radially integrated around the beam center to produce plots of intensity versus scattering vector magnitude, q, defined as $q=4\pi\sin\theta/\lambda$, where 2θ is the total scattering angle and λ is the x-ray wavelength.

Physisorption. Nitrogen physisorption isotherms were measured at -196 °C using a Micromeritics ASAP 2020 system. All samples were degassed under high vacuum at

150 °C overnight. The Brunauer, Emmett, and Teller (BET) and Brunauer, Jonyer, and Halenda (BJH) analysis were performed using Micromeritics ASAP 2020 V1.05 software.

XRD. Wide-angle X-ray diffraction measurements were performed using a Rigaku Ultima VI diffractometer at 40 kV and 44 mA where samples were scanned from 10 to 90 degrees with a 5 degrees/min speed.

Results and Discussion

Solvent evaporation induced structure formation

The dissolution of an SDA and an inorganic material is the fundamental first step towards their evaporative coassembly. However, typical hydrolytic sol-gel protocols for the coassembly of ordered titania films start with ~2-21 wt% SDA solutions of Pluronic[34, 49] or KLE[28] in ethanol with ~8-21 wt% water. Such alcohol and water rich solutions are incompatible with the dissolution of a tremendous diversity of potential polymer systems, including most derivatives of acrylates, methacrylates, styrenes, or dienes. The solubility of a particular component may be predicted from the Hildebrand solubility parameter (δ) which for a given molecule is the square root of its cohesive energy density and is measured in SI units of $\sqrt{(Jm^{-3})}$ or equivalently in √Pa. Most δ values range from 14.9 to 47.9 √MPa, intermediate between hexanes and water, respectively[66]. It follows that ethanol (δ=26.6 √MPa) is too hydrophilic to dissolve many common polymers such as polyisoprene, polystyrene, or poly(methyl methacrylate) (δ=16.5, 18.6, and 22.7 √MPa respectively). However, the simple

substitution of ethanol with common hydrophobic solvents such as hexane, toluene, or chloroform (δ=14.9, 18.2, and 19.0 √MPa respectively) leads to the precipitation of the titania sol since these solvents are all poor at hydrogen bonding. The solubility parameter for acetylacetonate modified titania particles[67] and bare rutile particles[68] are 20.5 and 30.1√MPa, respectively. The dissolution of all species requires the selection of a solvent or a mixture of solvents with a similar δ value and an appropriate hydrogen bonding strength. Thus solvents such as tetrahydrofuran with a low δ=18.6 √MPa value and a moderate ability to hydrogen bond should be appropriate for many systems involving hydrophobic polymer blocks. Indeed, tetrahydrofuran is a great solvent for many polymers including all of those mentioned thus far and for this reason is one of the most common eluent solvents for gel permeation chromatography of polymers. Thus tetrahydrofuran was chosen as the principle solvent for the coassembly of titania sols with the highly amphiphilic PI-*b*-PEO.

Dissolution of all coassembled species is required but not sufficient for the formation of equilibrated coassemblies. For example, the water associated with hydrolytic sol-gel processes may be concentrated as volatile organic solvents preferentially evaporate sometimes leading to the precipitation of hydrophobic polymers. The measured precipitation point for IO28K was ~4.1 wt.% water in THF determined using HCl(aq). Additionally, the composition of a mixed solvent system must remain favorable to all species present throughout the entire evaporation process. Relative evaporation rates and any azeotropic conditions should be considered for such mixed solvent systems. For example, mixtures of THF and water at atmospheric

pressure form an azeotrope with a lowered boiling point of 64 °C and a composition of 5.3 wt.% water. However, please note that deviations from the azeotropic temperature or the addition of other reagents will change the relative evaporation rates. Adaptation of reported titania coassembly protocols with a simple substitution of THF in place of ethanol resulted in film IO28K-h4. Note that before the addition of titanium isopropoxide the solution was close to, but slightly below, the threshold for polymer precipitation. Hydrolysis was expected to proceed quickly once the alkoxide was added, consuming all of the free water (TiR_4:H_2O=4.0:1.0)[9], though some of this consumed water was expected to be released from the slow condensation reaction during stirring and casting. The initially orange color fading to clear overtime was consistent with initial THF coordination to the in situ formed $Ti(O^iPr)_aCl_b(OH)_{4-a-b}$ followed by less coordination as the sol particles grew and had less specific surface area[69]. A titania:PI-*b*-PEO mass ratio of 2.0:1.0 was chosen to result in an inverse hexagonal morphology based on the previously established morphology map for the coassembly of PI-*b*-PEO with an aluminosilicate sol[58]. However, bright field TEM observations of the resulting film consisted of hollow dark circles consistent with an inverse spherical micelle (iSM) morphology containing PI cores (light) and PEO-TiO_2 coronas (dark) (Figure 2.1b and c). Quantitative TEM image analysis indicated that these crew cut micelles had a diameter of 30±3 nm, which was similar to values obtained from the first order peak located at 27 nm in SAXS measurements (Figure 2.1a). A second higher order SAXS peak was also observed at twice the reciprocal spacing of the first peak which was consistent with a simple cubic lattice, though not with either BCC nor FCC packing. However, no long-range order was apparent in the

TEM observations, so the second SAXS peak was attributed to random packing of spheres. Extensive previous experiments indicate that the utilized IO28K should result in about 16 nm diameter iH cylinders. The larger than expected micelle diameters and deviation from the expected morphology suggest that sample IO28K-h4 was not equilibrated, but rather kinetically trapped due to solvent selectivity for just the PEO block.

Solvent composition likely plays a key role as the system transitions from solution dynamics to bulk behavior. If the solvent composition is favorable to all components, i.e., non-selective then the block copolymer chains exist as non-aggregated unimers evenly distributed throughout the solution. If a solvent system is non-selective throughout the entire evaporation process then the hybrid would gradually enter bulk behavior from a random mixed state. In contrast, when the solvent composition favors one portion of an amphiphile, the solvo-phobic portions aggregate leading to micelle formation typically with a spherical morphology. Published examples indicate that the addition of 3-11 wt.% of a selective solvent to a block copolymer solution in a non-selective solvent is sufficient to induce micellization, depending on the particular blocks, block lengths, and solvents involved[70-73]. Indeed, the IO28K used in this study was significantly longer (28 kg/mol) and more hydrophobic (72 wt% PI), than the block copolymers typically used for micellization studies. One may anticipate such a polymer to be more sensitive to the presence of selective hydrophilic solvents, *vide infra*.

To elucidate the role of residual water throughout structure formation several nearly identical films were prepared, only varying the quantity of THF added. With

increasing THF content the starting weight fraction of water was lowered sequentially from IO28K-h4, IO28K-h3, IO28K-h2, to IO28K-h1. The iSM morphology of the sample with the least THF, IO28K-h4, was already described, *vide supra*. Before describing the intermediate samples, we focus on IO28K-h1, the sample with the most THF added, i.e. the lowest water concentration. The SAXS pattern for IO28K-h1 was consistent with an inverse hexagonally arranged cylinders (iH) morphology (Figure 2.1j). The allowed peaks for hexagonal symmetry are indicated in the figure at $(q/q_{10})^2$=1, 3, 4, 7, 9 and 11. Additionally, significant sample texturing was evidenced by a pair of spots for $(q/q_{10})^2$=4 peaks. TEM observations confirmed the presence of an iH morphology having PI cylinders (light) hexagonally arranged within a PEO-TiO_2 matrix (dark) (Figure 2.1k and j). Quantitative TEM measurements indicated a d_{10} spacing of 26±2 nm, compared to the SAXS d_{10} dimension of 31.5 nm. The cylinder diameter and titania wall thickness as determined from TEM measurements were 16±2 nm and 14±1 nm, respectively. Such a large hexagonal structure with thick walls is expected to be more thermally stable than the smaller ones typically obtained from Pluronic or KLE polymers (Table 2.1).

The intermediate samples exhibited mixed morphologies between the two boundary cases of IO28K-h4 and IO28K-h1. The SAXS pattern of sample IO28K-h3 was similar to that of IO28K-h4, but with the addition of a shoulder consistent with the q_{10} peak of IO28K-h1 (Figure 2.1d). TEM images of sample IO28K-h3 contained primarily ~30 nm inverse spherical micelles, just like sample IO28K-h4, but with the addition of minority domains with iH morphology (Figure 2.1e and f). The SAXS pattern for IO28K-h2 was similar to the bimodal pattern of IO28K-h3, however

intensity distribution in the convoluted first peak indicated a decreased content of iSM and an increased content of iH (Figure 2.1g). This trend was confirmed by TEM imaging which revealed primarily domains with iH morphology with a minority of ~30 nm iSMs (Figure 2.1h and f). The structural analysis of tis series of samples indicates a strong morphological dependence on solution conditions during evaporation.

The predominant mechanisms of micelle equilibration, both unimer expulsion-insertion and micelle fusion-fission, are dependent upon the interaction strength between the solvophobic block and the solvent[74]. Though there is still discussion as to whether just one or a combination of these mechanisms is active[74-76], the equilibration rates and effecting factors were nonetheless measurable. The exchange kinetics for block copolymer micelles generally range from slow, i.e. 1-100 billion times slower than small molecule surfactants[77], to immeasurably slow[78-83]. The unimer exchange rate was found to depend exponentially on the surface tension penalty for solvophobe-solvent contact[84, 85]. Lodge *et al.* recently found that unimer exchange was hypersensitive to the length of the solvophobic chains with a double exponential dependence enabling the precise measurement of polydispersity from the ensemble[86]. For the present study, the differences in morphological behavior could be attributed to the different starting points for solvent composition before evaporation (Figure 2.2b). All samples are expected to increase in water composition during evaporation with the particular starting water composition establishing a trajectory to the final water composition. Thus the evolution dynamics and morphology should depend on the selectivity of the solvent mixture during

coassembly. To further elucidate the structural changes during casting, *in situ* SAXS measurements were performed. Sample IO28K-h1 did not exhibit any scattering patterns in solution until a broad hump appeared 80 minutes after casting (10% retained mass) just prior to becoming a semisolid and then proceeded directly to the iH scattering pattern at the next measurement at 86 minutes (Figure S1). Although the temporal resolution was insufficient to elucidate the molecular dynamics, the measurements did indicate that the key period for structure formation is in the last minutes of casting as the semisolid films formed.

Considering these findings it is surprising that ordered aluminosilicate morphologies were ever achieved with PI-*b*-PEOs. Typical recipes for such hybrids start with a 5 wt.% polymer solution and utilize an inorganic:organic ratio of 2 leading to 12.7 wt.% water before hydrolysis and 2.3 wt.% water after complete hydrolysis. The apparent insensitivity to water could be due to at least two factors: 1) Silicate sols undergo condensation much slower than transition metal oxides which would result in less water release after hydrolysis. 2) Silicate sols formed under acidic conditions tend to form fractal networks with high internal surface area. Such a porous sol might physisorb much of the free-water from solution enabling the PI-*b*-PEO to avoid micellization. Furthermore, these results elucidate the morphological behavior of KLE structure directing agents, which regardless of inorganic:organic ratio seem to always form spherical micellar morphologies. It is likely that the use of water and alcohol rich solutions to prepare these hybrids leads to trapping the KLE in a selective-solvent induced morphology and preventing the evolution of other morphologies.

Mesoporous materials

The conversion of sample IO28K-h1 to mesoporous crystalline titania was tested with the CASH procedure described previously in detail[57]. The first calcination of IO28K-h1 was to 700 °C under N_2 leading to sample IO28K-h1-C. The resulting material was black consistent with the expected carbon residue. SEM images of IO28K-h1-C indicated that the highly ordered iH morphology of IO28K-h1 survived the high temperature heat treatment (Figure S2a). Quantitative measurements from the SEM images indicated an average unit cell of dimension d_{10}=23.2±3.2 nm with cylinder diameter of 12.4±2.7 nm and a wall thickness of 12.8±2.0 nm. SAXS measurements similarly confirmed 25.7 % shrinkage with a smaller d_{10}=23.4 nm (Figure S2c). Many coassembled oxide structures have mesostructural compression along the film normal[23, 60, 62, 63, 87, 88]. This compression complicates SAXS analysis since the orientation of the powdered sample was unknown and thus the longest real-space d_{10} dimension from the elliptical scattering pattern was assumed to coincide with the film normal and was thus used for comparison. Wide angle XRD analysis of IO28K-h1-C confirmed the presence of anatase titania (PDF#21-1272) with a Debye-Sherrer average domain size of 9.7 nm calculated from the non-convoluted (101) and (200) peaks (Figure S2e). Though the diffraction pattern was dominantly anatase, there was a trace quantity of rutile (PDF#1088-1172). Nitrogen physisorption of IO28K-h1-C exhibited a classic type IV isotherm with an H_2 hysteresis loop[12] (Figure S2h) indicative of mesopores with restricted pathways (ink bottle). A heterogeneous carbon distribution throughout the cylindrical pores could be the cause of this hysteresis loop. Application of the BET model led to a calculated

overall surface area of 124.7 m^2/g. BJH analysis of the adsorption branch lead to an average mesopore size of 12.5 nm (Figure S2i). The carbon was removed from IO28K-h1-C by heating to 450 °C in air resulting in IO28K-h1-CASH. The white product was consistent with oxidative removal of the carbon. SEM imaging of IO28K-h1-CASH indicated that the ordered iH mesostructure survived removal of the carbon (Figure S2b). Analysis of the SEM images indicated a cylinder diameter of 12.7±1.8 nm, a wall thickness of 10.2±1.7nm, with d_{10}=22.1±2.6 nm. This compared to a d_{10}=22.3 nm determined by SAXS measurements. The SAXS pattern again contained a broad first-order peak suggesting the preservation of the mesostructure although higher ordered peaks were no longer detected (Figure S2d). Again wide angle XRD confirmed the presence of anatase titania with a Debye-Sherrer average domain size of 10.8 nm and again a trace of rutile. Physisorption analysis of IO28K-h1-CASH exhibited a classical type IV isotherm with a very small hysteresis, consistent with long cylindrical pores of homogeneous diameter (Figure S2h). Application of the BJH model to the adsorption isotherm led to an average mesopore size of 16.1 nm consistent with additional densification of the titania after carbon removal (Figure S2i). BET analysis was consistent with this densification indicating a reduced overall surface area of 82.4 m^2/g. This data set indicates that the CASH method was successfully applied to the materials described herein.

The previous examples demonstrate that these solubility design principles enable ordered mesoporous transition metal oxide structures from highly amphiphilic block copolymers. Exploiting different molecular weight PI-*b*-PEOs together with the solubility design guidelines and the CASH method described above enabled the pore

size control of mesoporous crystalline titania. To this end different TiO_2-IO hybrid materials from PI-b-PEOs with molar masses between 92 and 7 kg/mol but with identical inorganic/organic ratio were synthesized aiming for an inverse hexagonal morphology. Indeed, bright field TEM images and SAXS measurements of all hybrids were consistent with a highly ordered iH morphology (Figure 2.3). The SAXS spectra show higher order peaks at $(q/q_{10})^2$=4 and 7 for all hybrid materials while the d-spacing decreased from 63.0 to 13.8 nm consistent with the decrease of the PI-*b*-PEO molar masses.

Highly ordered mesoporous and crystalline titania were synthesized from these hybrids via the CASH method. When the hybrids were heated to 700 °C and dwelled for 4 hrs in nitrogen with subsequent calcinations at 450 °C in air, crystalline titania was formed as confirmed by wide angle XRD analysis. XRD spectra indicate mostly anatase phase with a trace amount of rutile for IO92K-CASH, IO41K-CASH and IO13K-CASH samples (Figure S4). A purely anatase crystalline phase was achieved by adjusting the temperature and time of the first heat treatment step of the CASH method, as confirmed by the XRD spectra for IO92K-CASH (Figure 2.4c), IO41K-CASH, IO13K-CASH and IO7K-CASH (Figure S5). Details of the respective heat processing conditions are described in Table S1 showing that block copolymer directed titania can be transformed into highly crystalline and pure anatase phase upon heat treatments at 600~700 °C for 2~4 hrs.

Characterization results of the largest pore titania with a highly ordered and crystalline structure are presented in Figure 2.4. The SEM imaging verified a highly ordered hexagonally arranged cylindrical morphology of the anatase titania after

removal of the block copolymer template (Figure 2.4a), consistent with TEM results (Figure S3). TEM analysis was performed after the brittle titania samples were ground and put on carbon-coated grids. The crushed particles were neither uniform in thickness nor ultrathin and only the edges could be imaged. The highly ordered mesostructure was further confirmed by SAXS analysis showing higher order peaks at $(q/q_{10})^2$=1, 4 and 7 as in the IO92K-h hybrid material (Figure 2.4b). The SAXS d_{10} spacing was determined as 48.5 nm suggesting a 23 % shrinkage upon removal of the block copolymer template from the hybrid material and crystallization of titania (d_{10}= 63.0 nm) via the CASH method. Nitrogen physisorption measurements revealed a narrow pore size distribution with average pore size of 32.3 nm along with a classical type IV isotherm that is typical of mesoporous materials with cylindrical pore geometry and a highly uniform pore size distribution (Figure 2.4e). The anatase crystallite domain size was calculated to be 11.9 nm using the Scherrer equation.

The structural characteristics of block copolymer derived titania hybrids and resulting mesoporous crystalline titania with pore size control are summarized in table 2.3. The surface areas obtained from BET analysis of nitrogen adsorption-desorption data are high, i.e. 64-85 m^2/g for all mesoporous titania. The narrow pore size distributions and the type IV isotherms of titania for IO41K-CASH, IO13K-CASH and IO7K-CASH are consistent with the results described for IO92K-CASH (Figure S6). Figure 2.5 displays the dependence of SAXS derived d-spacings and BJH derived pore sizes on PI-*b*-PEO molar mass for the various titania/PI-*b*-PEO hybrids and resulting mesoporous crystalline titania materials ($R^2 > 0.99$) investigated. To the best of our knowledge we report here the largest pore size to date (32.3 nm) of highly ordered

crystalline titania from a block copolymer-inorganic self assembly approach without the use of a pore expanding agent.

The solubility principles are generalizable to more complex ABC triblock terpolymers. Poly(isoprene-*b*-styrene-*b*-ethylene oxide) (ISO) was selected since it contains two common hydrophobic blocks, i.e., polyisoprene and polystyrene, and has recently been used for the production of 3D networked aluminosilicate morphologies with a wide composition window[63]. Such networked morphologies have unique advantages in that they have three-dimensional continuity of all domains and can maintain such percolation pathways with low <30 vol.% of oxide. Casting solutions were prepared with very low ~1 wt.% water content to enhance solubility of the hydrophobic blocks during casting (Figure 2.2c). The successful production of ordered network morphologies from ISO1 combined with titania sols is demonstrated by sample ISO1-TiO_2. Microtomed sections of this sample clearly showed the ordered network connectivity (Figure 2.6a,b) with both four-fold and three-fold symmetry, consistent with a cubic network morphology. The SAXS pattern for ISO1-TiO2 contained two broad peaks that were rather equivocal to interpret directly (Figure 2.6c). However, previous experiments with the same ISO1 polymer and niobia sols exhibited a similar scattering pattern and was determined by electron tomography to be consistent with an O^{70} morphology having an equilateral unit cell[89]. Quantitative TEM measurements from these projections corresponded to a d_{100} spacing of 37-48 nm compared to d_{100}=57.0 nm determined by interpreting the first SAXS peak as d_{110}. Such smaller than expected TEM measurements have been observed before for similar samples containing low T_g blocks that can reflow after microtoming causing structural

distortions[17, 63, 89]. The titania nanostructures from coassembly with ISO1 demonstrate that the solubility design guidelines enable the use of complex triblock terpolymers to synthesize highly ordered nanocomposites.

The crystallization of the ISO1-TiO_2 network was studied with a combination of electron microscopy, SAXS, and XRD. Initial experiments calcining ISO1-TiO_2 indicated that this mesostructure with a minority of oxide is not able to survive high temperature heat treatments, with significant collapse after heating bulk films to 450 °C. Thus we compare two lower temperature heat treatments to 400 °C, in either N_2 or air resulting in samples ISO1-TiO_2-N_2 and ISO1-TiO_2-air, respectively. The mesostructure of both samples survived the heat treatment as evidenced by both SEM images and SAXS observations (Figure 2.7a-d). The d_{100} spacing of sample ISO1-TiO_2-N_2 was determined from SAXS and SEM to be 45.0 nm and 42.6±4.4 nm, respectively. Sample ISO1-TiO_2-air also had a smaller d_{100} spacing which was measured by SAXS and SEM to be 39.5 nm and 40.7±3.0 nm, respectively. Comparison of the SAXS d_{100} spacings indicates that ISO1-TiO_2-N_2 experienced the least contraction, 21% (compared to 31% for ISO1-TiO_2-air), likely due to the *in situ* formation of a carbonaceous hard template as in the CASH procedure. XRD spectra from both samples were consistent with nanocrystallites of anatase titania (Figure 2.5e-g). The low intensity of anatase peaks in sample ISO1-TiO_2-N_2 suggests that a significant amount of amorphous titania is present. The *in situ* formed carbonaceous material perhaps constrains the crystallization process by providing a diffusion barrier. Debye-Scherrer analysis of the non-convoluted (101) and (200) peaks of ISO1-TiO_2-air indicated an average crystallite size of 7.5 nm. These results indicate that when

constrained to lower temperature heat treatments, calcination in air yields more crystalline anatase. We anticipate that such ordered mesoporous networks of crystalline titania will enable better performance of next generation energy materials.

Table 2.1. Comparison of three structure directing agents for ordered mesoporous silicates

	Pluronic PEO-*b*-PPO-*b*-PEO	**KLE PHB-*b*-PEO**	**IO PI-*b*-PEO**
Flory Huggins χ at 50 °C	0.085[90]	~0.33*	0.33[91]
Mn (kg/mol)	2-13[20]	8-10[92]	10-84[93]
wt%PEO	30-70%[20]	37-57%[92]	8-38%[93]
Water / Alcohol Soluble	Yes	Yes**	No
Hybrid Morphologies	CM, iH, G, L[34, 94]	CM[92]	(i)CM, (i)H, PN, G, L[58]
Pore size range (nm)* **	5-10[18]	12-13[92]	11-50[93]

CM=cubic packing of spherical micelles, L=lamellar, H=hexagonally arranged cylinders, G=double gyroid, PN=plumber's nightmare

*χ for KLE is similar to that for IO

**PHB and PI homopolymers are not soluble in water or alcohols, but can be dispersed as aggregates in such solvents when of low molecular weight and attached to a large fraction of PEO

***Ordered mesopores without pore-expanders

Table 2.2. Synthesis and characterization of PI-b-PEO block copolymers

	IO7K	**IO13K**	**IO28K**	**IO41K**	**IO92K**
Overall M_n, g/mol	6,787	12,500	27,975	40,981	91,900
PI, g/mol	4,410	9,948	20,230	30,121	63,227
PEO, g/mol	2,377	2,552	7,745	10,860	28,673
PDI	1.11	1.10	1.06	1.07	1.09
χN[a]	39.2	67.3	156.0	227.3	521
R_o of PEO[b], nm	4.4	4.5	7.9	9.3	15.2

[a] χN was calculated using $\chi = 65/T + 0.125$.
[b] R_o was calculated based on the equation, $R_0 = 0.595\sqrt{N}$.

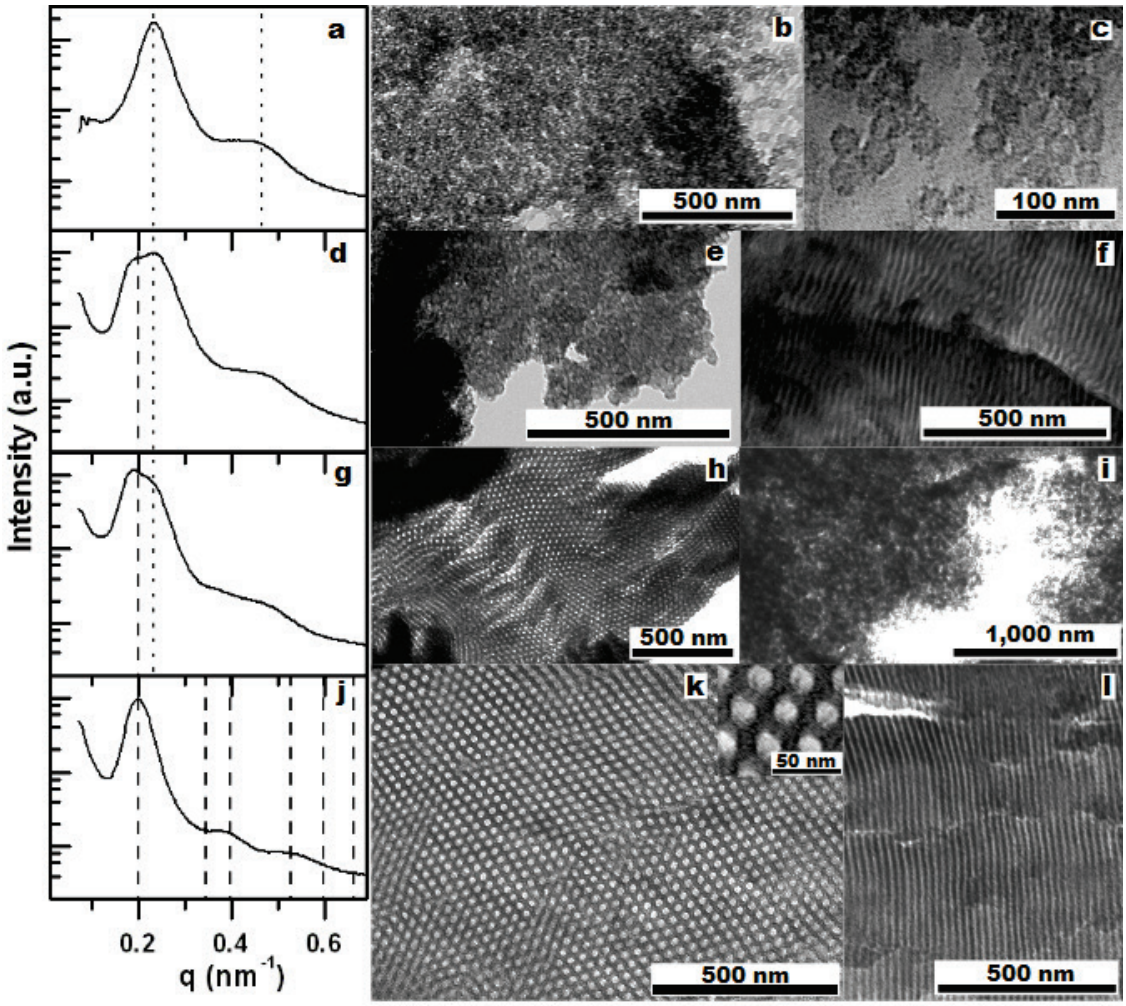

Figure 2.1. The SAXS patterns for samples IO28K-h4 (a), IO28K-h3 (d), IO28K-h2 (g), and IO28K-h1 (j) indexed with a random micellar lattice (dots), a hexagonal lattice (dashes), or a mixture of the two. Bright field TEM images of IO28K-h4 (b,c), IO28K-h3 (e,f), IO28K-h2 (h,i), and IO28K-h1 (k,l) are consistent with inverse spherical micelles (iSM), inverse hexagonally arranged cylinders (iH), or a mixture of the two. The data are presented as rows for each sample organized in order of increasing water content.

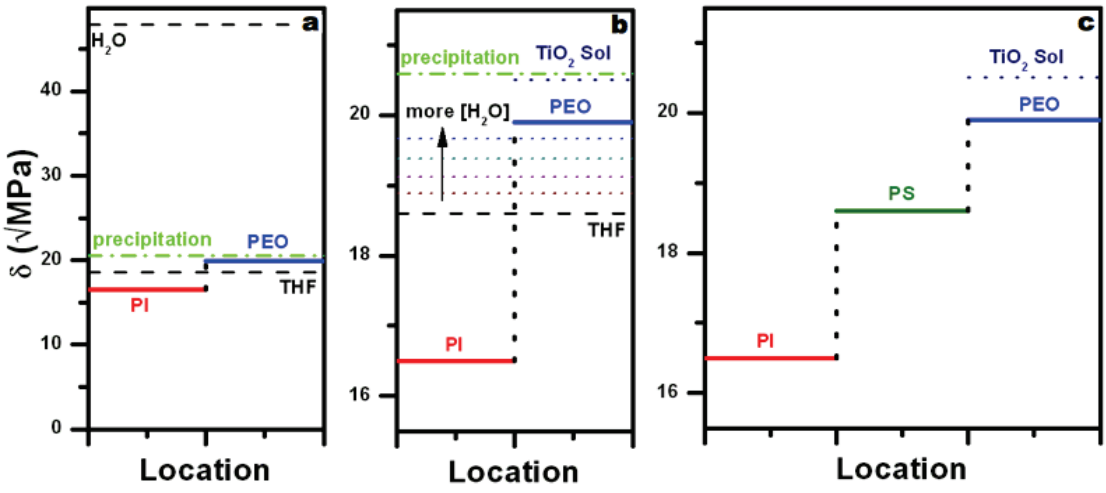

Figure 2.2. Plots of Hildebrand solubility parameters indicating the relative strength of intermolecular interactions and facilitating the prediction of miscibility. Though water is a precipitation agent for many polymers its use is required for numerous hydrolytic sol-gel procedures (a). Samples IO28K-h1, IO28K-h2, IO28K-h3, and IO28K-h4 were prepared with increasing initial water concentrations (b) leading to strikingly different morphologies (compare to Figure 2.1). Successful co-assembly with more complex triblock terpolymer structure directing agents requires attention to the solubility of all four species involved.

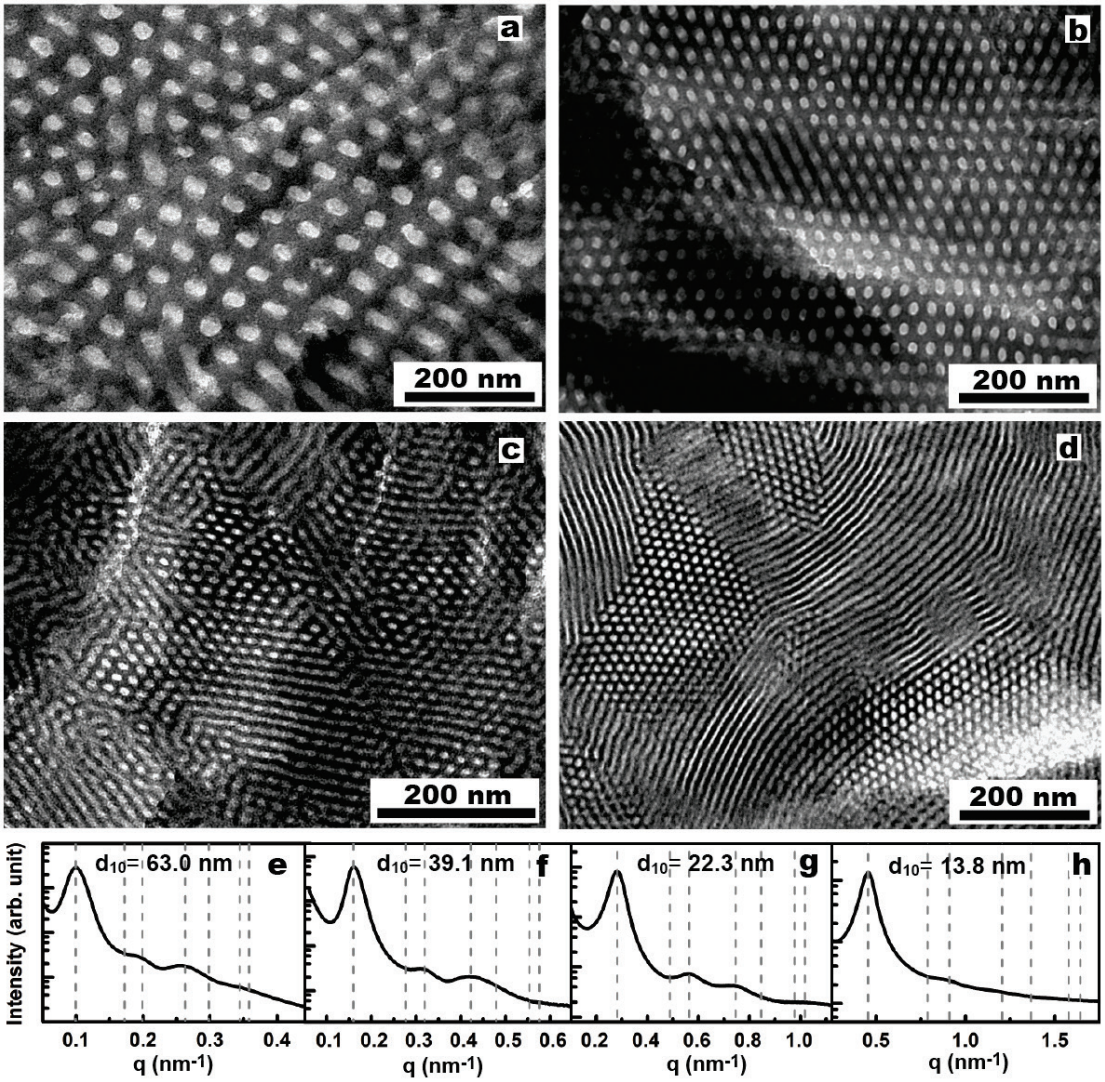

Figure 2.3. Bright field TEM images and SAXS patterns for BCP/titania hybrid samples: IO92K-h (a,e), IO41K-h (b,f), IO13K-h (c,g) and IO7K-h (d,h). The SAXS patterns are indexed with a hexagonal lattice (1, √3, √4, √7, √9, √12, √13) and q is defined as $q = 4\pi \sin\theta/\lambda$. The d-spacings from SAXS measurements were calculated from $d_{10} = 2\pi/q^*$ where q* is the q number at primary peak of each spectrum.

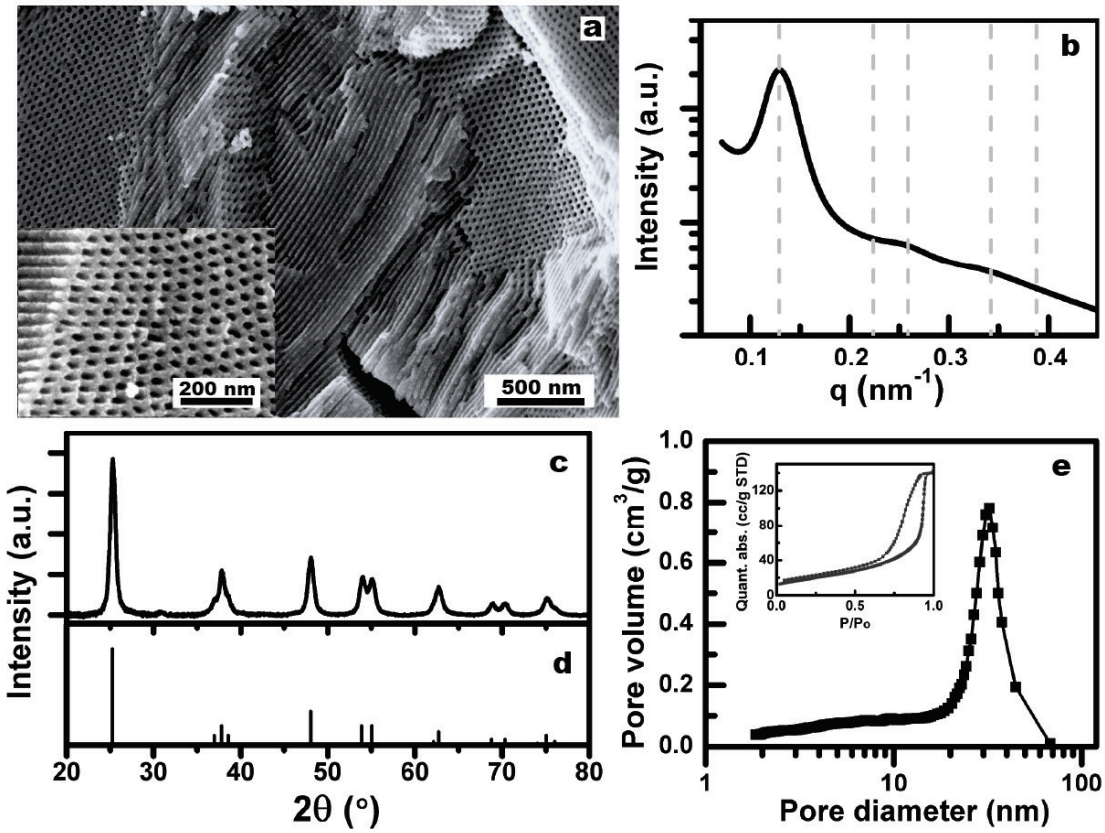

Figure 2.4. The ordered mesostructure of IO92K-CASH after the first calcinations in inert atmosphere followed by the subsequent calcination in air is confirmed by SEM (a) and SAXS (b). The d-spacing from SAXS was calculated as 48.5 nm. XRD analysis indicates that the mesoporous titania is highly crystalline (c), with peak assignments consistent with anatase titania (d, PDF#21-1272). Nitrogen physisorption measurements and analysis confirm that this sample is mesoporous with narrow BJH pore size distribution and average pore size of 32.3 nm (e).

Table 2.3. Summary of structure characteristics of PI-*b*-PEO derived hybrids and mesoporous titania

BCP/titania hybrids	IO7K-h	IO13K-h	IO28K-h[a]	IO41K-h	IO92K-h
SAXS d-spacing, nm	13.8	22.3	31.5	39.1	63.0
Mesoporous titania	IO7K-CASH	IO13K-CASH	IO28K-CASH	IO41K-CASH	IO92K-CASH
Pore size[b], nm	8.9	11.4	16.1	19.2	32.3
Surface area[c], m^2/g	70.0	84.9	82.4	69.2	64.1

[a] Inorganic/organic ratio (2.0) is slightly smaller than the other materials (2.15).
[b] Pore size is determined from the peak value of the BJH adsorption derived pore size distribution and [c] surface area is obtained from BET analysis of nitrogen adsorption-desorption data.

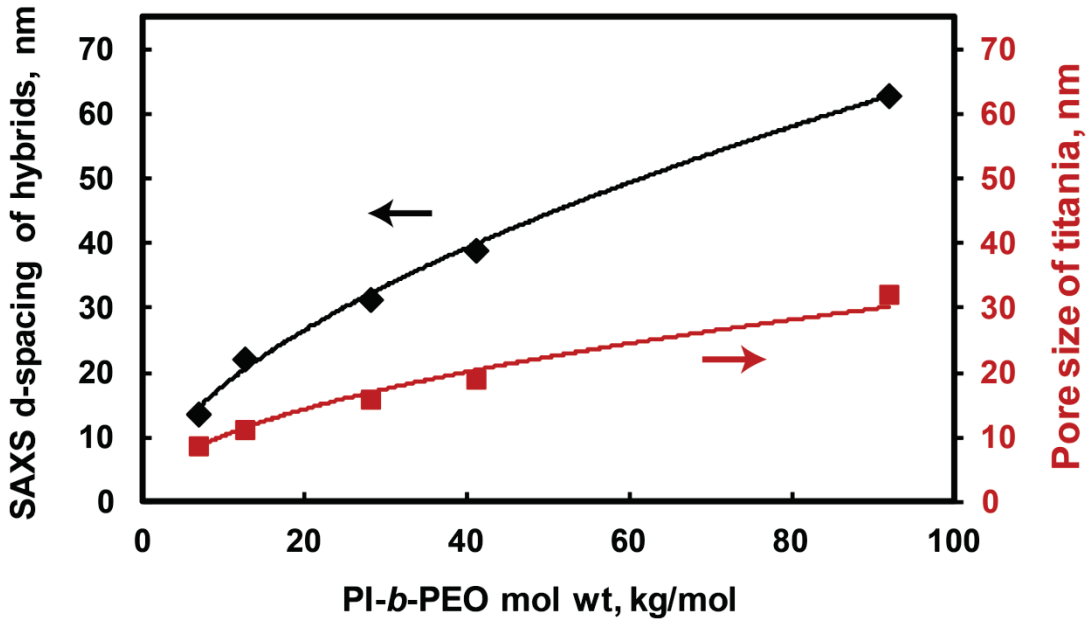

Figure 2.5. Dependence of d-spacings obtained from SAXS and BJH derived pore sizes on PI-*b*-PEO molar mass for titania/PI-*b*-PEO hybrids and resulting mesoporous crystalline titania, respectively.

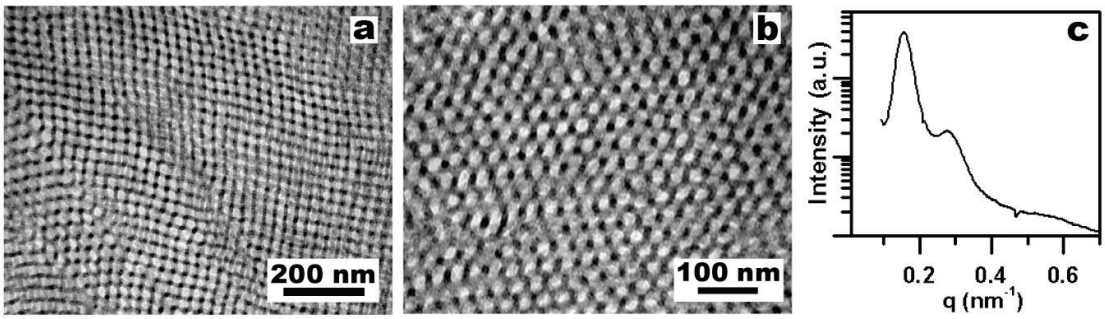

Figure 2.6. Bright field TEM images of microtomed sections of ISO1-TiO_2 showing four-fold (a) and three-fold projections (b), consistent with a cubic network morphology. The broad SAXS pattern for ISO1-TiO_2 (c) is similar to a previously reported pattern for networked hybrids derived from the same ISO1 polymer and niobia.

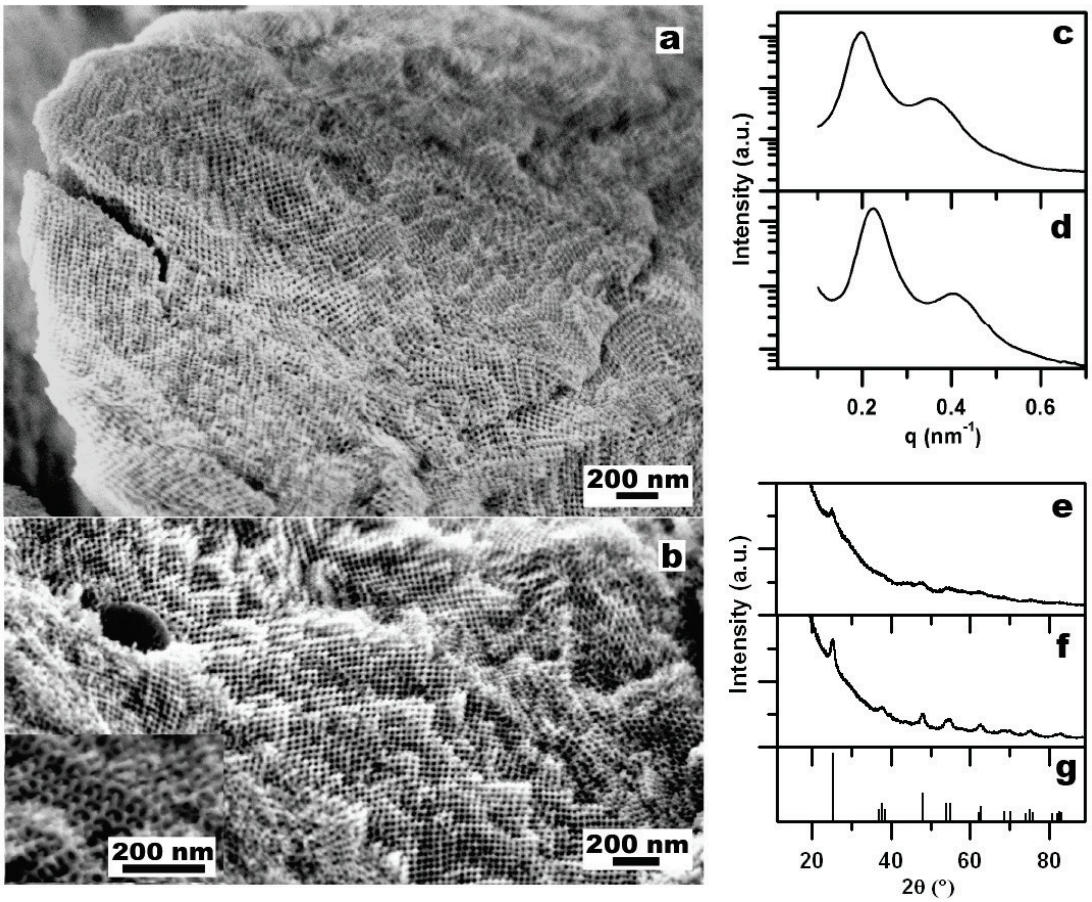

Figure 2.7. Sample ISO1-TiO_2 with ordered network mesostructure calcined at lower temperatures to avoid structural collapse. The preserved mesostructure after calcination in inert atmosphere with preserved long-range order is evidenced by SEM (a) and SAXS (c), however, according to XRD (e) the resulting titania is only slightly crystalline. Calcination of ISO1-TiO_2 directly in air results in similar structural preservation as evidenced by SEM (b) and SAXS (d), but from XRD results leads to a greater extent of crystallization to the anatase phase (f,g)..

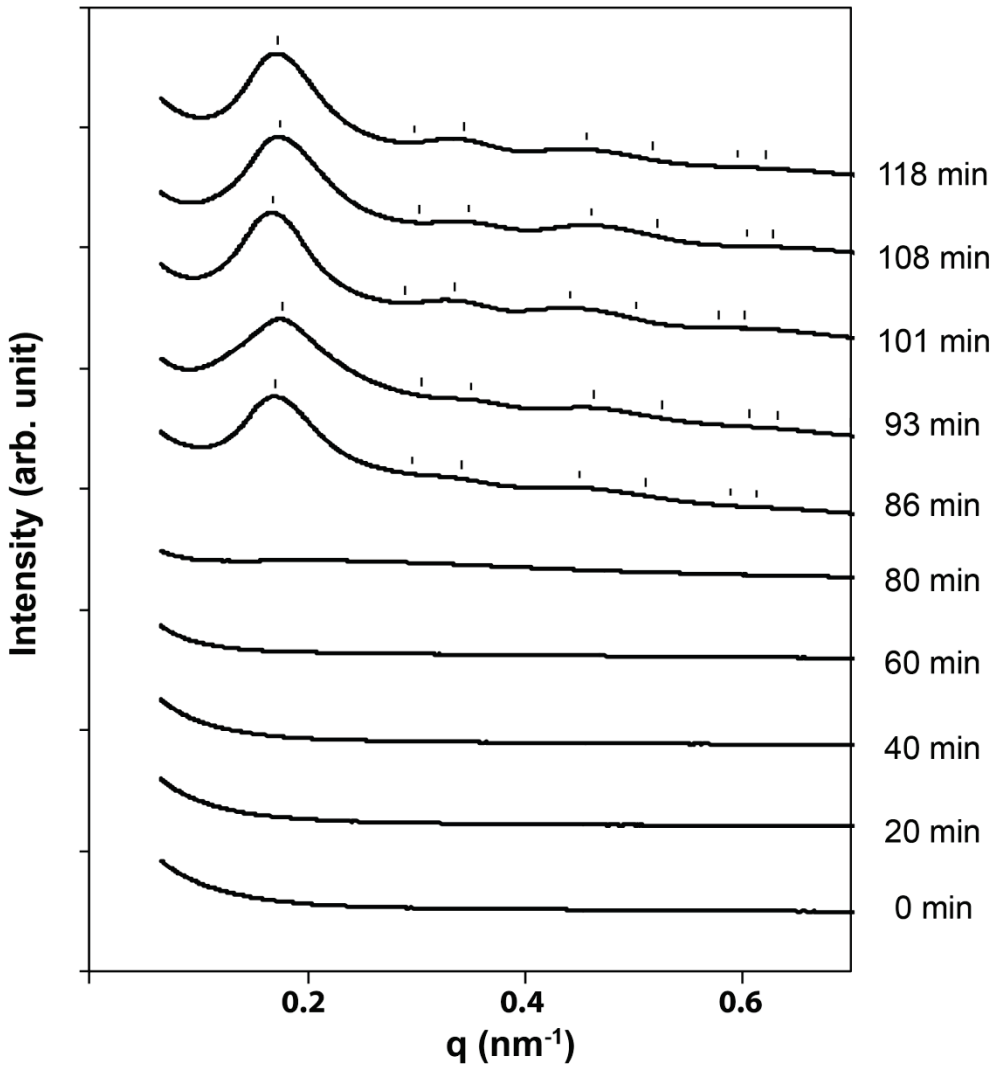

Figure S1.The Small Angle X-ray Scattering data: the evolution of hexagonally arranged mesostructure of IO28K-h1 hybrid material during the evaporation process.

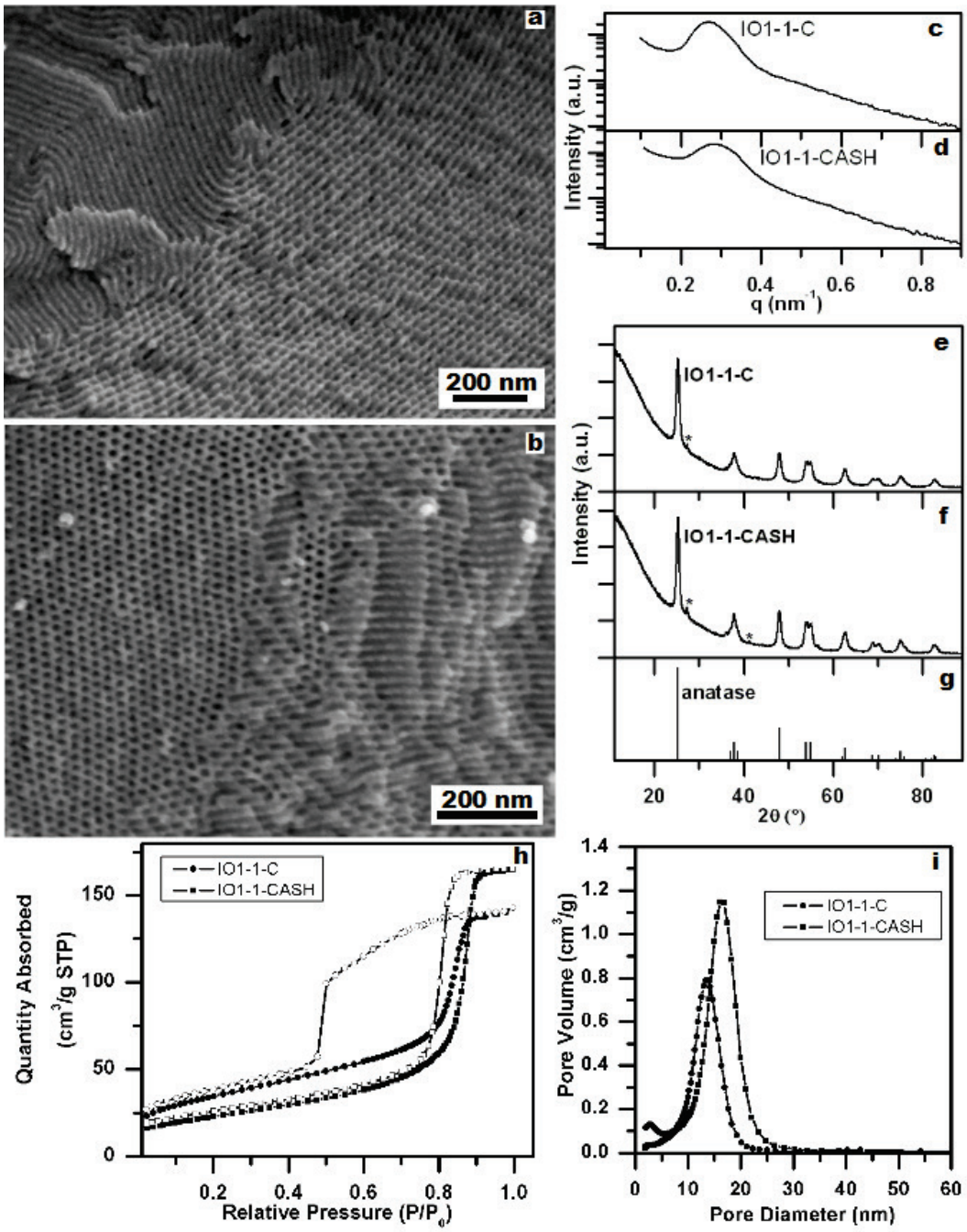

Figure S2. An ordered mesostructure of IO28K-h1-C after the first calcination in inert atmosphere is confirmed by SEM (a) and SAXS (c). The subsequent calcination in air also preserves the ordered mesostructure of IO28K-h1-CASH as confirmed by SEM (b) and SAXS (d). XRD analysis indicates that the first heat treatment results in crystallization of the amorphous titania sol to anatase (e), which is preserved after the second heat treatment (f). XRD peaks are consistent with anatase titania (g, PDF#21-1272) with the exception of trace rutile peaks (*). Nitrogen physisorption measurements indicate that both samples are mesoporous (h) with narrow BJH pore size distributions (i).

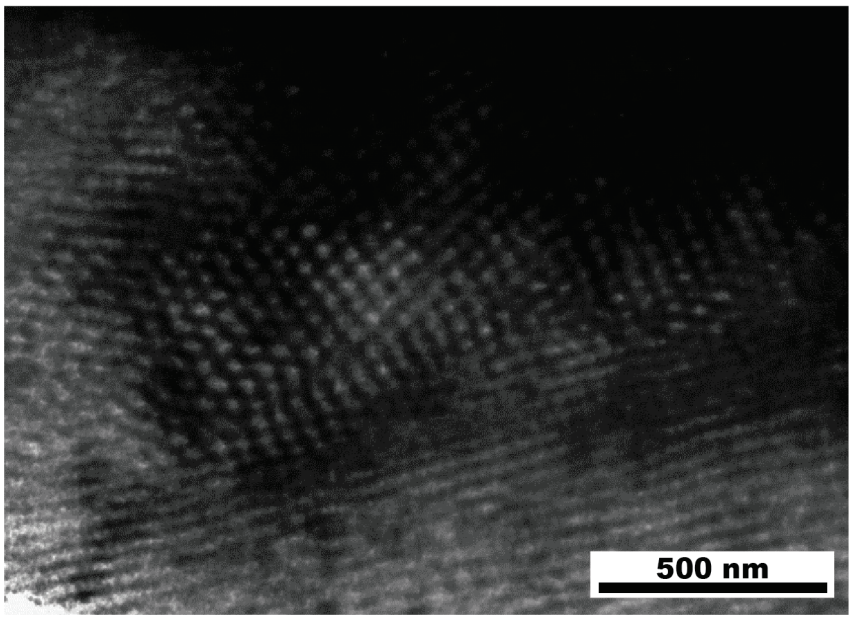

Figure S3. TEM image of IO92K-CASH indicating that mesoporosity is preserved after CASH heat treatments.

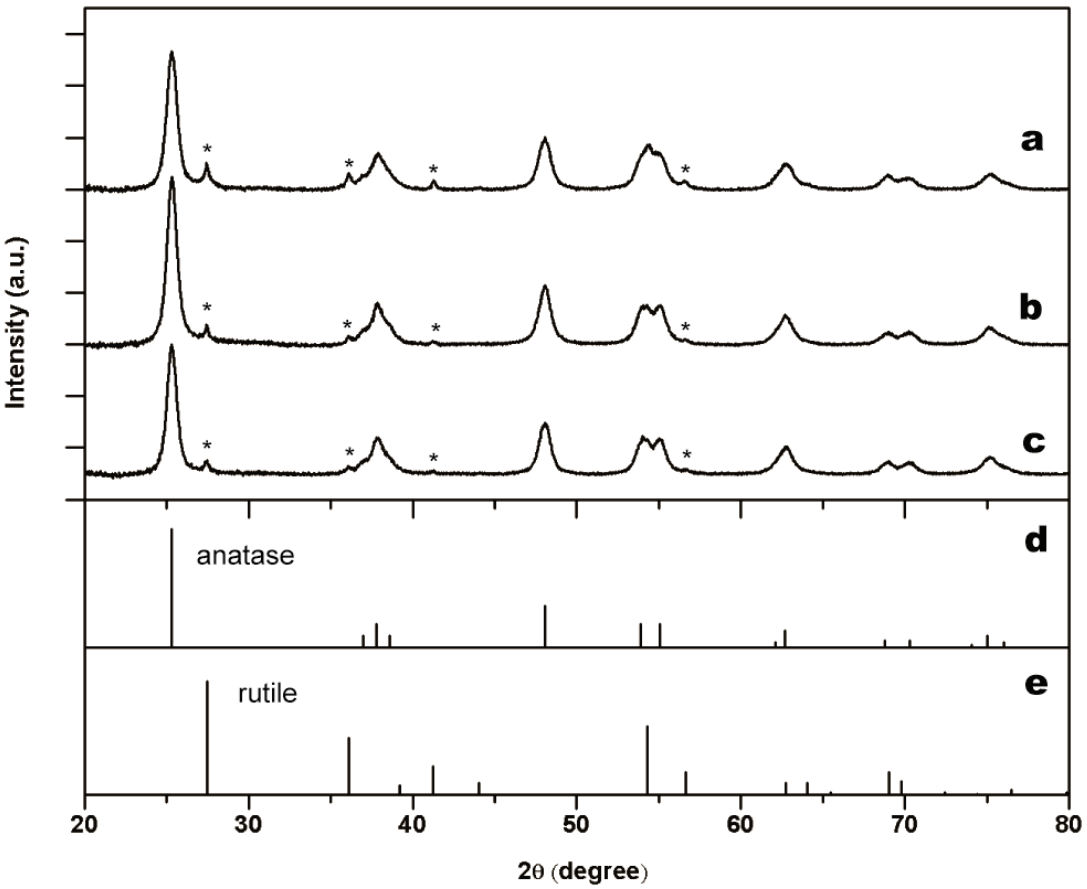

Figure S4. The XRD patterns for mesoporous crystalline titania after CASH heat treatments; IO92K-CASH (a), IO41K-CASH (b), IO13K-CASH (c), standard anatase TiO_2 (d, PDF#21-1272) and rutile TiO_2 (e, PDF#21-1276). Samples were first calcined at 700'C for 4 hrs under nitrogen atmosphere. The second calcination was then carried out at 450'C for 4 hrs in air.

Table S1. CASH heat processing conditions for PI-*b*-PEO/titania hybrid materials. The temperature and time of the first heat treatment step are adjusted to give pure anatase crystalline phase for titania from IO13K-h, IO41K-h and IO92K-h.

Titania-IO(PI-*b*-PEO)	**IO7K-CASH**	**IO13K-CASH**	**IO41K-CASH**	**IO92K-CASH**
Heat treatment -1 (under nitrogen)				
Temperature, ‘C	700	600	600	700
Dwelling time, hr	4	2	2	2
Ramp rate, ‘C/min	5	1	1	1
Heat treatment -2 (under air)				
Temperature, ‘C	450	450	450	450
Dwelling time, hr	4	2	2	2
Ramp rate, ‘C/min	5	1	1	1

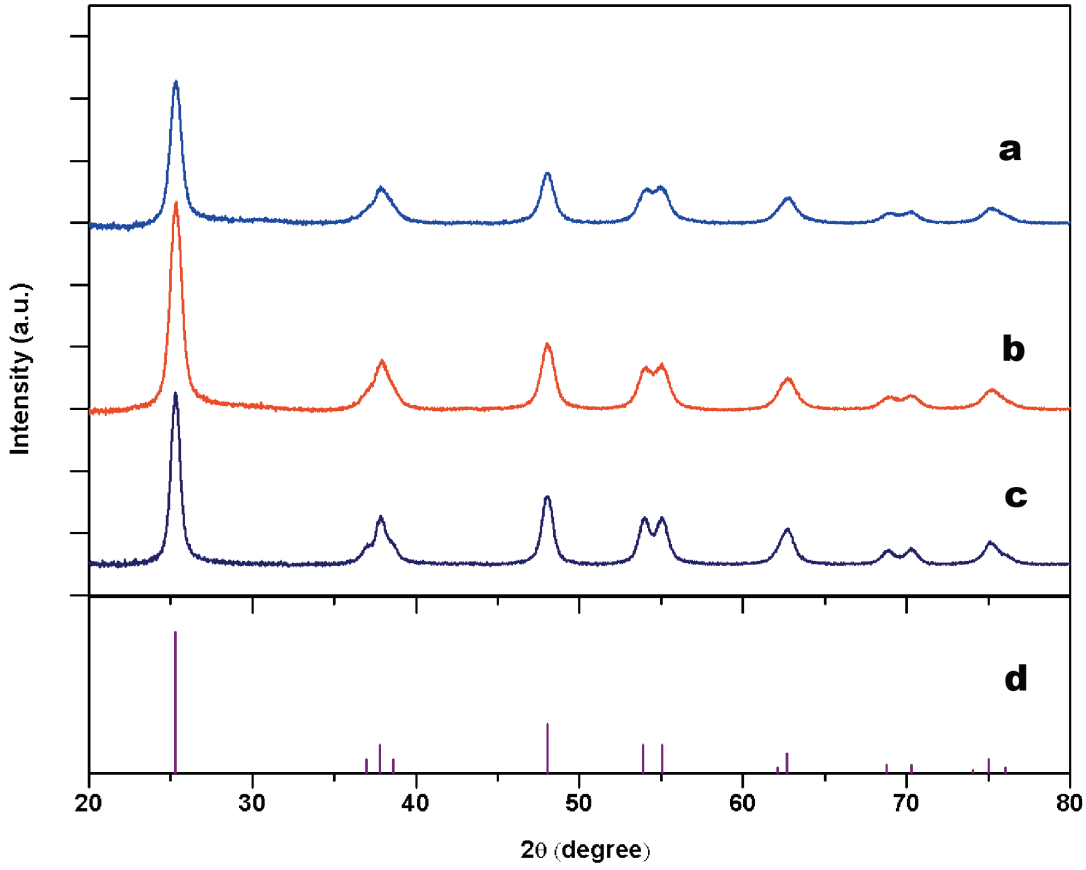

Figure S5. XRD patterns for mesoporous crystalline titania after CASH heat treatments as described in Table S1.; IO41K-CASH (a), IO13K-CASH (b) and IO7K-CASH (c). Bar markers indicate peaks for standard anatase TiO_2 structure (d, PDF#21-1272).

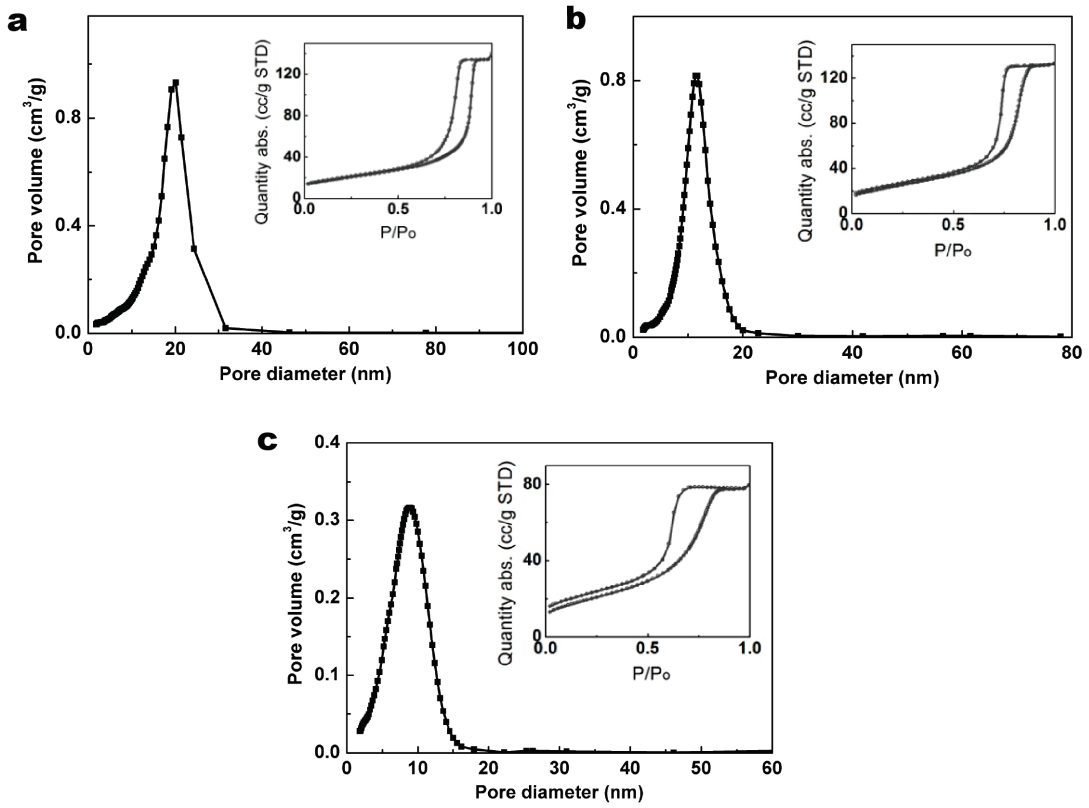

Figure S6. Pore size distributions of mesoporous titania from IO41K-CASH (a), IO13K-CASH (b) and IO7K-CASH (c). Pore sizes were calculated using the BJH adsorption pore analysis method. Insets show the corresponding nitrogen adsorption and desorption isotherms.

References

1. Yanagisawa, T., et al., *The preparation of alkyltrimethylammonium-kanemite complexes and their conversion to microporous materials.* Bulletin of the Chemical Society of Japan, 1990. **63**(4): p. 988-992.
2. Kresge, C.T., et al., *Ordered Mesoporous Molecular-Sieves Synthesized by a Liquid-Crystal Template Mechanism.* Nature, 1992. **359**(6397): p. 710-712.
3. Zukalova, M., et al., *Organized mesoporous TiO2 films exhibiting greatly enhanced performance in dye-sensitized solar cells.* Nano Letters, 2005. **5**(9): p. 1789-1792.
4. Nedelcu, M., et al., *Block copolymer directed synthesis of mesoporous TiO2 for dye-sensitized solar cells.* Soft Matter, 2009. **5**(1): p. 134-139.
5. Szeifert, J.M., et al., *"Brick and Mortar" Strategy for the Formation of Highly Crystalline Mesoporous Titania Films from Nanocrystalline Building Blocks.* Chemistry of Materials, 2009. **21**(7): p. 1260-1265.
6. Docampo, P., et al., *Control of Solid-State Dye-Sensitized Solar Cell Performance by Block-Copolymer-Directed TiO2 Synthesis.* Advanced Functional Materials, 2010. **20**(11): p. 1787-1796.
7. Guldin, S., et al., *Dye-Sensitized Solar Cell Based on a Three-Dimensional Photonic Crystal.* Nano Letters, 2010. **10**(7): p. 2303-2309.
8. Li, L., et al., *Enhanced photocatalytic properties in well-ordered mesoporous WO(3).* Chemical Communications, 2010. **46**(40): p. 7620-7622.
9. Brinker, C.J. and G.W. Scherer, *Sol-gel science : the physics and chemistry of sol-gel processing*. 1990, Boston: Academic Press.
10. Huo, Q.S., et al., *Generalized Synthesis of Periodic Surfactant Inorganic Composite-materials.* Nature, 1994. **368**(6469): p. 317-321.
11. Antonelli, D.M. and J.Y. Ying, *Synthesis of Hexagonally Packed Mesoporous TiO_2 by a Modified Sol-Gel Method.* Angewandte Chemie-International Edition in English, 1995. **34**(18): p. 2014-2017.
12. Sing, K.S.W., et al., *Reporting Physisorption Data for Gas Solid Systems with Special Reference to the Determination of Surface-Area and Porosity.* Pure and Applied Chemistry, 1985. **57**(4): p. 603-619.
13. Rouquerol, J., et al., *Recommendations for the Characterization of Porous Solids.* Pure and Applied Chemistry, 1994. **66**(8): p. 1739-1758.
14. Raman, N.K., M.T. Anderson, and C.J. Brinker, *Template-based approaches to the preparation of amorphous, nanoporous silicas.* Chemistry of Materials, 1996. **8**(8): p. 1682-1701.
15. Bagshaw, S.A., E. Prouzet, and T.J. Pinnavaia, *Templating of Mesoporous*

Molecular-Sieves by Nonionic Polyethylene Oxide Surfactants. Science, 1995. **269**(5228): p. 1242-1244.

16. Tanev, P.T. and T.J. Pinnavaia, *A Neutral Templating Route to Mesoporous Molecular Sieves.* Science, 1995. **267**(5199): p. 865-867.
17. Templin, M., et al., *Organically modified aluminosilicate mesostructures from block copolymer phases.* Science, 1997. **278**(5344): p. 1795-1798.
18. Zhao, D.Y., et al., *Triblock copolymer syntheses of mesoporous silica with periodic 50 to 300 angstrom pores.* Science, 1998. **279**(5350): p. 548-552.
19. Yang, P.D., et al., *Generalized syntheses of large-pore mesoporous metal oxides with semicrystalline frameworks.* Nature, 1998. **396**(6707): p. 152-155.
20. Wanka, G., H. Hoffmann, and W. Ulbricht, *Phase-Diagrams and Aggregation Behavior of Poly(oxyethylene)-Poly(oxypropylene)-Poly(oxyethylene) Triblock Copolymers in Aqueous-Solutions.* Macromolecules, 1994. **27**(15): p. 4145-4159.
21. Yang, P.D., et al., *Block copolymer templating syntheses of mesoporous metal oxides with large ordering lengths and semicrystalline framework.* Chemistry of Materials, 1999. **11**(10): p. 2813-2826.
22. Malfatti, L., et al., *One-Pot Route to Produce Hierarchically Porous Titania Thin Films by Controlled Self-Assembly, Swelling, and Phase Separation.* Chemistry of Materials, 2009. **21**(13): p. 2763-2769.
23. Crepaldi, E.L., et al., *Controlled formation of highly organized mesoporous titania thin films: From mesostructured hybrids to mesoporous nanoanatase TiO2.* Journal of the American Chemical Society, 2003. **125**(32): p. 9770-9786.
24. Grosso, D., et al., *Highly porous TiO2 anatase optical thin films with cubic mesostructure stabilized at 700 degrees C.* Chemistry of Materials, 2003. **15**(24): p. 4562-4570.
25. Choi, S.Y., et al., *Thermally stable two-dimensional hexagonal mesoporous nanocrystalline anatase, meso-nc-TiO2: Bulk and crack-free thin film morphologies.* Advanced Functional Materials, 2004. **14**(4): p. 335-344.
26. Smarsly, B., et al., *Highly crystalline cubic mesoporous TiO2 with 10-nm pore diameter made with a new block copolymer template.* Chemistry of Materials, 2004. **16**(15): p. 2948-2952.
27. Fattakhova-Rohlfing, D., et al., *Highly organized mesoporous TiO2 films with controlled crystallinity: A Li-insertion study.* Advanced Functional Materials, 2007. **17**(1): p. 123-132.
28. Brezesinski, T., et al., *Templated Nanocrystal-Based Porous TiO2 Films for Next-Generation Electrochemical Capacitors.* Journal of the American Chemical Society, 2009. **131**(5): p. 1802-1809.
29. Antonelli, D.M., *Synthesis of phosphorus-free mesoporous titania via templating*

with amine surfactants. Microporous and Mesoporous Materials, 1999. **30**(2-3): p. 315-319.

30. Khushalani, D., et al., *Glycometallate-surfactants Part 2: non-aqueous synthesis of mesoporous titanium, zirconium and niobium oxides*. Journal of Materials Chemistry, 1999. **9**(7): p. 1491-1500.
31. Soler-Illia, G. and C. Sanchez, *Interactions between poly(ethylene oxide)-based surfactants and transition metal alkoxides: their role in the templated construction of mesostructured hybrid organic-inorganic composites*. New Journal of Chemistry, 2000. **24**(7): p. 493-499.
32. Grosso, D., et al., *Highly organized mesoporous titania thin films showing mono-oriented 2D hexagonal channels*. Advanced Materials, 2001. **13**(14): p. 1085-+.
33. Soler-Illia, G., et al., *Design of meso-structured titanium oxo based hybrid organic-inorganic networks*. New Journal of Chemistry, 2001. **25**(1): p. 156-165.
34. Alberius, P.C.A., et al., *General predictive syntheses of cubic, hexagonal, and lamellar silica and titania mesostructured thin films*. Chemistry of Materials, 2002. **14**(8): p. 3284-3294.
35. Soler-Illia, G., A. Louis, and C. Sanchez, *Synthesis and characterization of mesostructured titania-based materials through evaporation-induced self-assembly*. Chemistry of Materials, 2002. **14**(2): p. 750-759.
36. Steunou, N., et al., *Synthesis of nanostructured polymer-titanium oxide composites through the assembly of titanium-oxo clusters and amphiphilic block copolymers micelles*. Journal of Materials Chemistry, 2002. **12**(12): p. 3426-3430.
37. Crepaldi, E.L., et al., *Nanocrystallised titania and zirconia mesoporous thin films exhibiting enhanced thermal stability*. New Journal of Chemistry, 2003. **27**(1): p. 9-13.
38. Dag, O., et al., *Solventless acid-free synthesis of mesostructured titania: Nanovessels for metal complexes and metal nanoclusters*. Advanced Functional Materials, 2003. **13**(1): p. 30-36.
39. Angelome, P.C., et al., *Hybrid non-silica mesoporous thin films*. New Journal of Chemistry, 2005. **29**(1): p. 59-63.
40. Bartl, M.H., et al., *3-D molecular assembly of function in titania-based composite material systems*. Accounts of Chemical Research, 2005. **38**(4): p. 263-271.
41. Boettcher, S.W., et al., *Structural analysis of hybrid titania-based mesostructured composites*. Journal of the American Chemical Society, 2005. **127**(27): p. 9721-9730.
42. Choi, S.Y., et al., *Evolution of nanocrystallinity in periodic mesoporous anatase thin films*. Small, 2005. **1**(2): p. 226-232.
43. Groenewolt, M., et al., *Polyisobutylene-block-poly(ethylene oxide) for robust*

templating of highly ordered mesoporous materials. Advanced Materials, 2005. **17**(9): p. 1158-+.

44. Shibata, H., et al., *Direct synthesis of mesoporous titania particles having a crystalline wall.* Journal of the American Chemical Society, 2005. **127**(47): p. 16396-16397.

45. Fan, J., S.W. Boettcher, and G.D. Stucky, *Nanoparticle assembly of ordered multicomponent mesostructured metal oxides via a versatile sol-gel process.* Chemistry of Materials, 2006. **18**(26): p. 6391-6396.

46. Fuertes, M.C. and G. Soler-Illia, *Processing of macroporous titania thin films: From multiscale functional porosity to nanocrystalline macroporous TiO2.* Chemistry of Materials, 2006. **18**(8): p. 2109-2117.

47. Sakatani, Y., et al., *Optimised photocatalytic activity of grid-like mesoporous TiO2 films: effect of crystallinity, pore size distribution, and pore accessibility.* Journal of Materials Chemistry, 2006. **16**(1): p. 77-82.

48. Boettcher, S.W., et al., *Harnessing the sol-gel process for the assembly of non-silicate mesostructured oxide materials.* Accounts of Chemical Research, 2007. **40**(9): p. 784-792.

49. Dong, W.Y., et al., *Controllable and repeatable synthesis of thermally stable anatase nanocrystal-silica composites with highly ordered hexagonal mesostructures.* Journal of the American Chemical Society, 2007. **129**(45): p. 13894-13904.

50. Park, O.H., et al., *Formation and photopatterning of nanoporous titania thin films.* Applied Physics Letters, 2007. **90**(23): p. 3.

51. Bass, J.D., et al., *Pyrolysis, crystallization, and sintering of mesostructured titania thin films assessed by in situ thermal ellipsometry.* Journal of the American Chemical Society, 2008. **130**(25): p. 7882-7897.

52. Sokolov, S., E. Ortel, and R. Kraehnert, *Mesoporous titania films with adjustable pore size coated on stainless steel substrates.* Materials Research Bulletin, 2009. **44**(12): p. 2222-2227.

53. Edler, K.J., et al., *Association of Titania with Nonionic Block Copolymers in Ethanol: The Early Stages of Templating and Film Formation.* Chemistry of Materials, 2010. **22**(16): p. 4579-4590.

54. Cheng, Y.J. and J.S. Gutmann, *Morphology phase diagram of ultrathin anatase TiO2 films templated by a single PS-b-PEO block copolymer.* Journal of the American Chemical Society, 2006. **128**(14): p. 4658-4674.

55. Perlich, J., et al., *Modification of the morphology of P(S-b-EO) templated thin TiO2 films by swelling with PS homopolymer.* Langmuir, 2007. **23**(20): p. 10299-10306.

56. Cheng, Y.-J., et al., *Surface-Supported, Highly Ordered Macroporous Crystalline*

TiO2 Thin Films Robust up to 1000 Â°C. Chemistry of Materials, 2008. **20**(21): p. 6580-6582.

57. Lee, J., et al., *Direct access to thermally stable and highly crystalline mesoporous transition-metal oxides with uniform pores.* Nature Materials, 2008. **7**(3): p. 222-228.
58. Garcia, B.C., et al., *Morphology Diagram of a Diblock Copolymer-Aluminosilicate Nanoparticle System.* Chemistry of Materials, 2009. **21**(22): p. 5397-5405.
59. Finnefrock, A.C., et al., *Metal oxide containing mesoporous silica with bicontinuous "Plumber's Nightmare" morphology from a block copolymer-hybrid mesophase.* Angewandte Chemie-International Edition, 2001. **40**(7): p. 1207-+.
60. Finnefrock, A.C., et al., *The plumber's nightmare: A new morphology in block copolymer-ceramic nanocomposites and mesoporous aluminosilicates.* Journal of the American Chemical Society, 2003. **125**(43): p. 13084-13093.
61. Jain, A., et al., *Direct access to bicontinuous skeletal inorganic plumber's nightmare networks from block copolymers.* Angewandte Chemie-International Edition, 2005. **44**(8): p. 1226-1229.
62. Toombes, G.E.S., et al., *A re-evaluation of the morphology of a bicontinuous block copolymer-ceramic material.* Macromolecules, 2007. **40**(25): p. 8974-8982.
63. Stefik, M., et al., *Ordered Three- and Five-ply Nanocomposites from ABC Block Terpolymer Microphase Separation with Niobia and Aluminosilicate Sols.* Chemistry of Materials, 2009. **21**(22): p. 5466-5473.
64. Allgaier, J., et al., *Synthesis and characterization of poly[1,4-isoprene-b-(ethylene oxide)] and poly[ethylene-co-propylene-b-(ethylene oxide)] block copolymers.* Macromolecules, 1997. **30**(6): p. 1582-1586.
65. Warren, S.C., F.J. Disalvo, and U. Wiesner, *Nanoparticle-tuned assembly and disassembly of mesostructured silica hybrids.* Nature Materials, 2007. **6**(2): p. 156-161.
66. Brandrup, J., et al. *Polymer handbook*. 1999.
67. Chen, L., et al., *Synthesis of well-ordered mesoporous titania with tunable phase content and high photoactivity.* Journal of Physical Chemistry C, 2007. **111**(32): p. 11849-11853.
68. Arellano, M., I. Manas-Zloczower, and D.L. Feke, *Effect of surfactant treatment on the formation of bound polymer on titanium dioxide powders.* Powder Technology, 1995. **84**(2): p. 117-126.
69. Manxzer, L.E., et al., *31. Tetrahydrofuran Complexes of Selected Early Transition Metals*. Inorganic Syntheses. 2007: John Wiley & Sons, Inc. 135-140.
70. Zhang, L.F. and A. Eisenberg, *Multiple morphologies of crew-cut aggregates of*

polystyrene-b-poly(acrylic acid) block-copolymers. Science, 1995. **268**(5218): p. 1728-1731.

71. Zhang, L.F. and A. Eisenberg, *Multiple morphologies and characteristics of "crew-cut" micelle-like aggregates of polystyrene-b-poly(acrylic acid) diblock copolymers in aqueous solutions.* Journal of the American Chemical Society, 1996. **118**(13): p. 3168-3181.
72. Yu, Y.S., L.F. Zhang, and A. Eisenberg, *Multiple morphologies of crew cut aggregates of polybutadiene-b-poly(acrylic acid) diblocks with low T-g cores.* Langmuir, 1997. **13**(9): p. 2578-2581.
73. Choucair, A. and A. Eisenberg, *Control of amphiphilic block copolymer morphologies using solution conditions.* European Physical Journal E, 2003. **10**(1): p. 37-44.
74. Haliloglu, T., et al., *Mechanisms of the exchange of diblock copolymers between micelles at dynamic equilibrium.* Macromolecules, 1996. **29**(13): p. 4764-4771.
75. Halperin, A. and S. Alexander, *Polymeric Micelles - Their Relaxation Kinetics.* Macromolecules, 1989. **22**(5): p. 2403-2412.
76. Dormidontova, E.E., *Micellization kinetics in block copolymer solutions: Scaling model.* Macromolecules, 1999. **32**(22): p. 7630-7644.
77. Creutz, S., et al., *Exchange of polymer molecules between block copolymer micelles studied by emission spectroscopy. A method for the quantification of unimer exchange rates.* Macromolecules, 1997. **30**(14): p. 4078-4083.
78. Schillen, K., et al., *Characterization by fluorescence energy transfer of the core of polyisoprene-poly(methylmethacrylate) diblock copolymer micelles. Strong segregation in acetonitrile.* Macromolecules, 1998. **31**(1): p. 210-212.
79. Won, Y.Y., H.T. Davis, and F.S. Bates, *Molecular exchange in PEO-PB micelles in water.* Macromolecules, 2003. **36**(3): p. 953-955.
80. Jain, S. and F.S. Bates, *Consequences of nonergodicity in aqueous binary PEO-PB micellar dispersions.* Macromolecules, 2004. **37**(4): p. 1511-1523.
81. Denkova, A.G., E. Mendes, and M.O. Coppens, *Non-equilibrium dynamics of block copolymer micelles in solution: recent insights and open questions.* Soft Matter, 2010. **6**(11): p. 2351-2357.
82. Hayward, R.C. and D.J. Pochan, *Tailored Assemblies of Block Copolymers in Solution: It Is All about the Process.* Macromolecules, 2010. **43**(8): p. 3577-3584.
83. Nicolai, T., O. Colombani, and C. Chassenieux, *Dynamic polymeric micelles versus frozen nanoparticles formed by block copolymers.* Soft Matter, 2010. **6**(14): p. 3111-3118.
84. Willner, L., et al., *Time-resolved SANS for the determination of unimer exchange kinetics in block copolymer micelles.* Europhysics Letters, 2001. **55**(5): p. 667-673.

85. Lund, R., et al., *Equilibrium chain exchange kinetics of diblock copolymer micelles: Tuning and logarithmic relaxation.* Macromolecules, 2006. **39**(13): p. 4566-4575.

86. Choi, S.H., T.P. Lodge, and F.S. Bates, *Mechanism of Molecular Exchange in Diblock Copolymer Micelles: Hypersensitivity to Core Chain Length.* Physical Review Letters, 2010. **104**(4): p. 4.

87. Klotz, M., et al., *The true structure of hexagonal mesophase-templated silica films as revealed by X-ray scattering: Effects of thermal treatments and of nanoparticle seeding.* Chemistry of Materials, 2000. **12**(6): p. 1721-1728.

88. Schuster, J., et al., *Two-Dimensional-Hexagonal Periodic Mesoporous Polymer Resin Thin Films by Soft Templating.* Chemistry of Materials, 2009. **21**(24): p. 5754-5762.

89. Stefik, M., et al., *Networked and chiral nanocomposites from ABC triblock terpolymer coassembly with transition metal oxide nanoparticles.* Journal of Materials Chemistry, 2012. **22**(3): p. 1078-1087.

90. Hamley, I.W., et al., *Melt phase behavior of poly(oxyethylene)-poly(oxypropylene) diblock copolymers.* Macromolecules, 2001. **34**(12): p. 4079-4081.

91. Floudas, G., R. Ulrich, and U. Wiesner, *Microphase separation in poly(isoprene-b-ethylene oxide) diblock copolymer melts. I. Phase state and kinetics of the order-to-order transitions.* Journal of Chemical Physics, 1999. **110**(1): p. 652-663.

92. Thomas, A., et al., *Replication of lyotropic block copolymer mesophases into porous silica by nanocasting: Learning about finer details of polymer self-assembly.* Langmuir, 2003. **19**(10): p. 4455-4459.

93. Simon, P.F.W., et al., *Block copolymer-ceramic hybrid materials from organically modified ceramic precursors.* Chemistry of Materials, 2001. **13**(10): p. 3464-3486.

94. Liu, X.Y., et al., *Room-temperature synthesis in acidic media of large-pore three-dimensional bicontinuous mesoporous silica with Ia3d symmetry.* Angewandte Chemie-International Edition, 2002. **41**(20): p. 3876-3878.

CHAPTER 3

MESOPOROUS TITANIUM DIOXIDE THIN FILMS WITH CONTROLLED PORE SIZES FOR WATER PURIFICATION MEMBRANES

Abstract

Block copolymer self-assembly based structure formation of organic and inorganic hybrid materials is a promising route to ultrafiltration membrane fabrication. Uniform porosity with controlled pore structure and size can be achieved typically on a scale between 5-50 nm combined with tunable mechanical properties. Inorganic materials are known to provide better thermal and chemical stability than polymer membranes. Here we successfully synthesized mesoporous titania membranes with varying pore sizes on asymmetric porous substrates either by adjusting the solution concentration or by using a layer-by-layer approach. The resulting mesoporous titania membranes showed excellent molecular weight cut-off performance and also high permeability of 293.5 and 426.9 $Lm^{-2}hr^{-1}bar^{-1}$ for membranes from copolymers IO7K and IO92K, respectively.

Introduction

Membrane filtration processes are usually classified into microfiltration (pore diameters between 50-10^4 nm), ultrafiltration (5-100 nm), nanofiltration (1-10 nm), and reverse osmosis (up to 1 nm). These membranes are used to separate materials with specific sizes and the separation process is driven by pressure depending on the applications as described in Figure 3.1 [1]. Ultrafiltration (UF) has been employed in

many industries such as chemical and pharmaceutical manufacturing, food processing, and water purification. Moreover, UF is widely used for a pre-treatment stage prior to reverse osmosis processes for seawater desalination in many water-stressed countries in the Middle Eastern area [2].

For UF membrane applications, various polymer materials such as polysulfone, polyacrylonitrile, polyvinylidene fluoride etc. have been utilized in mostly hollow fiber and flat sheet shapes [3]. Inorganic membranes from materials such as titania, zirconia and alumina, have also been investigated, which offer numerous advantages: thermal stability, chemical resistance, pressure resistance (i.e. no compression under pressure), longer life time, and so forth [4]. Titania films for filtration have been prepared using polymeric sol-gel methods and a good chemical stability was reported in a wide pH range [5].

Block copolymer (BCP) self-assembly based structure formation is a promising route for making UF membranes because it provides (1) mesoporosity at the 5-50 nm length scale that falls nicely into the UF pore size regime, (2) uniform porosity with tunable pore size and morphology, (3) high void volume fraction, and (4) tunable mechanical properties [6-9]. Block copolymers used for UF membrane fabrication include poly(styrene-*b*-lactide) and poly(isoprene-*b*-styrene-*b*-4-vinylpyridine) and were reported to provide highly ordered membrane structures [10, 11].

Mesoporous titania films structure-directed by BCPs have received increasing attention as they can be used in wide set of applications such as photovoltaics, photocatalysis, optics and so forth [12-23]. For filtration membranes, mesoporous titania was prepared using surfactants as structure directing agents and the crack-free

titania film with ~16 nm pore size showed good clean water permeability while the nanostructure was not well ordered [24]. Very recently, Jing *et al.* reported mesoporous titania membranes for ultrafiltration based on pluronic triblock copolymers (PEO-PPO-PEO) with different compositions, where the titania film appeared to be disordered while they showed some improvement in rejection performance [25, 26].

Here we report on mesoporous titania membranes structure-directed by highly amphiphilic block copolymers, i.e. poly(isoprene-*b*-poly ethylene oxide) (PI-*b*-PEO), using a sol-gel solution process described in Chapter 2 of this thesis. As the thin films (~200 nm) of titania are extremely fragile, here mesoporous titania thin films were cast onto porous ceramic disc substrates that provide the necessary mechanical strength. In order to use a wide range of BCP molar masses, a layer-by-layer (LbL) approach to mesoporous membrane formation was developed. Finally, transport measurements in the form of solute separation experiments were performed on mesoporous titania membranes with different pore sizes to establish good permeability and tunable molecular weight cut-off (MWCO).

Experimental Section

Materials

Tetrahydrofuran (anhydrous, >99.9%, Aldrich), titanium isopropoxide (97%, Aldrich), and concentrated hydrochloric acid (37wt% ACS grade, BDH Aristar) were used as received. Poly(isoprene-*b*-ethylene oxide) (PI-*b*-PEO) was synthesized by anionic polymerization using reported procedures [27, 28]. Different molar mass PI-*b*-PEOs

from 7 to 92 kg/mol were synthesized and results of their characterization is summarized in Table 3.1. All polymers were narrowly dispersed with PDIs (polydispersity index) less than 1.11.

Sample Preparation

Thin films of TiO_2 structure directed from different PI-*b*-PEO (IO) BCPs were fabricated as follows: 50 mg of IO was dissolved in a certain amount of tetrahydrofuran (THF) depending on the targeted solution concentration. A titanium-containing sol (Ti-sol) was prepared by the addition of 1.2 ml of titanium isopropoxide into 0.387 ml of concentrated hydrochloric acid (37 %) followed by stirring for 5 min. Subsequently, 1.5 ml of THF was added to stabilize the Ti-sol with stirring for another 5 min. Then, 1 ml of prepared Ti-sol was put into the polymer solution and the mixed solution was let stirring for an hour. The resulting mixture was spin-coated onto Si substrates and porous ceramic discs as described elsewhere [29, 30]. The porous ceramic disc is mainly made up of coarse alumina particles with a thin top layer of zirconia that has ~60 nm random pores as shown in Figure S1. The disc provides mechanical strength and is 1.5 mm thick and 24 mm in diameter. Another support was used to put the porous disc on as the porous disc itself could not be held via vacuum on the spin coater. The spun-coat films were calcined in air at 450 °C for 4 hrs with a heating ramp rate of 1-2 °C/min, which removed the BCP template and promoted crystallization of anatase TiO_2.

Characterization

Atomic Force Microscopy (AFM) images were captured on a Veeco Nanoscope III in tapping mode with TappingMode Etched Si probes (resonance frequency = 325 kHz, force constant = 37 N/m, tip radius of curvature = 10 nm; all values nominal) under ambient conditions. Scanning electron microscopy (SEM) was performed using a LEO-1550 field emission SEM instrument. Membrane transport measurements in the form of solute separation experiments were performed using a Sterlitech pressurized stirred cell with a dextran mixture of 10^3 - 2×10^6 daltons in molar mass as a feed solution because dextran molecules do not interact with each other in aqueous solution. The resulting permeate solution was analyzed by high performance liquid chromatography (HPLC Dionex) with a refractive index (RI) detector (Shodex RI-71).

Results and Discussion

A mesoporous titania thin film from large molar mass BCP IO92K was prepared first via spin-coating on a flat Si substrate as shown in Figure 3.2. For this film, 5.25 ml of THF was used to dissolve enough polymer to provide a polymer concentration of 0.9 wt.% in solution. SEM images indicate that a uniform mesoporous titania film with thickness of ~60 nm was formed on the Si substrate. The pore size as estimated from the SEM image was ~30 nm with relatively narrow size distribution (Figure 3.2b). AFM images reveal the morphology of the top surface for the as-cast hybrid film as a hexagonally packed array of pores (Figure S2a). A film did not form properly when the same solution was applied to a porous substrate, mostly likely because due to its low viscosity the relatively dilute solution infiltrated into the open pores of the substrate. In addition to spin-coating the drop cast method was attempted but did not

work either as it was very difficult to control film thickness. We ended up with very thick films of ~4 μm which had major cracks (Figure S3).

A mesoporous titania film with large pores was successfully cast onto a porous disc substrate after the concentration of the polymer in solution was adjusted to ~2.1 wt.%, i.e. more than 2 times higher than in the first attempts. Figure 3.3 shows a large pore titania film with good structure control and surface coverage. The film thickness was about 70 nm and did not lead to any significant cracks.

Next the work was extended to smaller pore titania membranes by utilizing lower molar mass PI-*b*-PEOs. Generally, casting films from small molar mass polymers onto porous substrates is expected to be challenging due to low solution viscosity that allows infiltration of the solution into the open substrate pores. First, BCPs IO7K and IO41K were tried on a plane Si substrate as shown in Figure 3.4. The resulting uniform films showed smaller pore sizes when compared to results from BCP IO92K and the crack-free films had thicknesses of 140 nm and 210 nm, respectively, for IO7K and IO41K. As expected, BCP IO7K did not provide mesoporous titania films on porous disc substrates even at higher concentrations, i.e. 2.7 wt.% (b), or 3.5 wt.% (c), see Figure S4. Sample discs were not completely covered with titania film although the highest concentration gave more titania residue on the top surface of the substrate than the lower concentrations.

In order to successfully fabricate a small pore titania film on the porous disc substrates, a layer-by-layer approach was applied where TiO2-IO7K hybrid film was cast on top of a pre-cast TiO2-IO92K hybrid film that would prevent substrate pore infiltration by the IO7 based solution. All polymer material was removed in a

subsequent calcination step resulting in a small pore titania top film as shown in the SEM images of Figure 3.5.

Transport measurements through BCP directed titania membranes in the form of solute separation experiments to determine permeability and molecular weight cut-off (MWCO) values were performed using a mixed dextran solution with different molar mass components. The small pore titania membrane from BCP IO7K showed good performance in solute selectivity with MWCO of ~17 kg/mol at 90 % solute rejection. The MWCO of the large pore titania membrane was measured at ~200 kg/mol while the bare porous disc substrate did not show a good selectivity in the solute rejection (Figure 3.6). These titania membranes also gave high pure water permeabilities of 293.5 and 426.9 $Lm^{-2}hr^{-1}bar^{-1}$ for the mesoporous films from IO7K and IO92K, respectively (Table 3.2).

In summary, we successfully synthesized mesoporous titania membranes from different molar mass PI-*b*-PEOs as structure directing agents, either by adjusting the solution concentration or by using a layer-by-layer approach. Pore structures with narrow size distributions is one of the critical factors for successful UF membrane performance and the small pore titania membrane from IO7K showed high permeability and an excellent molecular weight cut-off. In the future the tunability of the titania pore size in the membrane will be further studied by systematically varying the molar mass of the block copolymers. Besides hexagonally ordered structures, ordered network morphologies such as the gyroid structure as obtained e.g. via the use of ABC triblock terpolymers as structure directing agents are interesting subjects for inorganic membrane investigations. Such terpolymers have recently been reported to

provide facile access to inorganic network structures [31, 32].

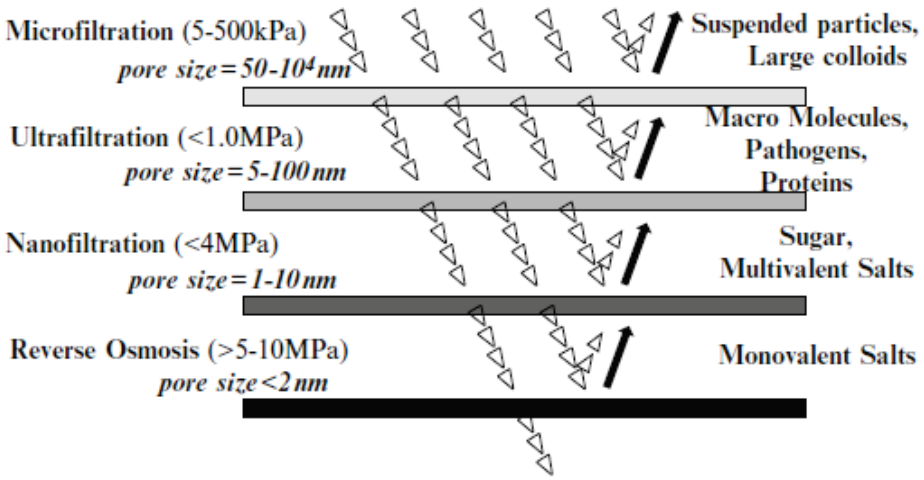

Figure 3.1. Membrane filtration classification in terms of pore size and corresponding applications [1].

Table 3.1. Synthesis and characterization of PI-b-PEO block copolymers used to structure-direct mesoporous titania filtration membranes

	IO7K	IO41K	IO92K
Overall Mn, g/mol	6,787	40,981	91,900
PI, g/mol	4,410	30,121	63,227
PEO, g/mol	2,377	10,860	28,673
Polydispersity index (PDI)	1.11	1.07	1.09

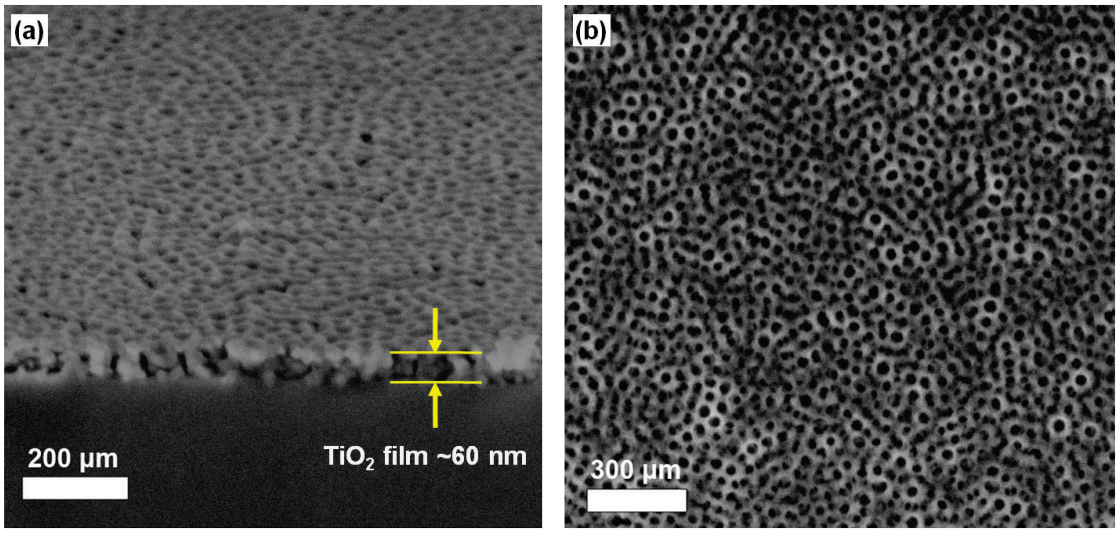

Figure 3.2. SEM images of titania film on Si substrate structure-directed from copolymer IO92K: cross sectional view (a) and top view (b). The mesoporous titania film formed a uniform ~60 nm thick film on the Si substrate..

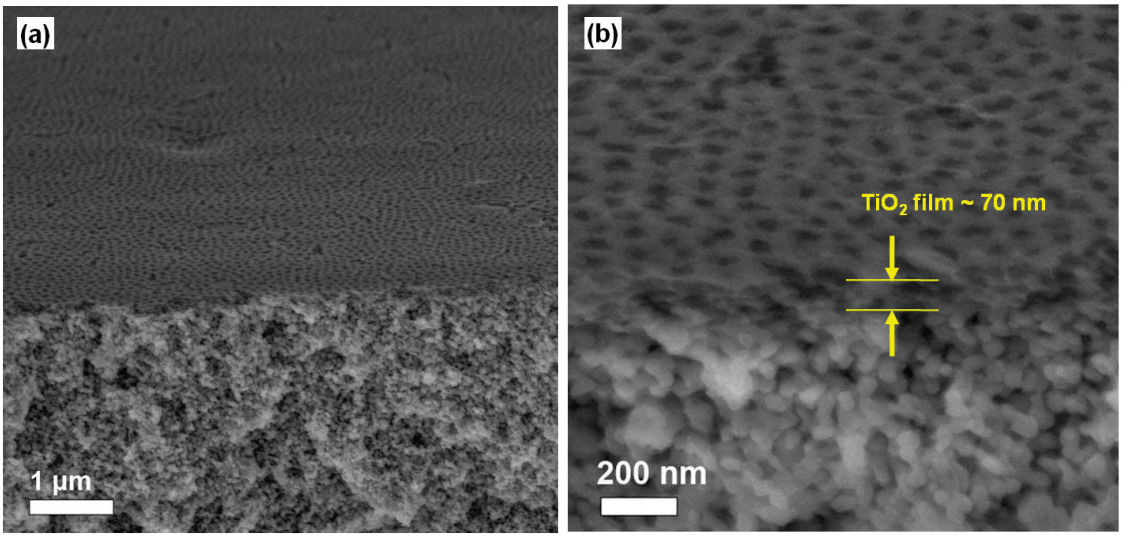

Figure 3.3. SEM images of a titania film on a porous substrate from copolymer IO92K spun from higher concentration and with lower spinning speed than the film shown in Figure 3.2. A mesoporous titania film of about 70 nm thicknes was uniformly formed on the substrate without any visible major cracks.

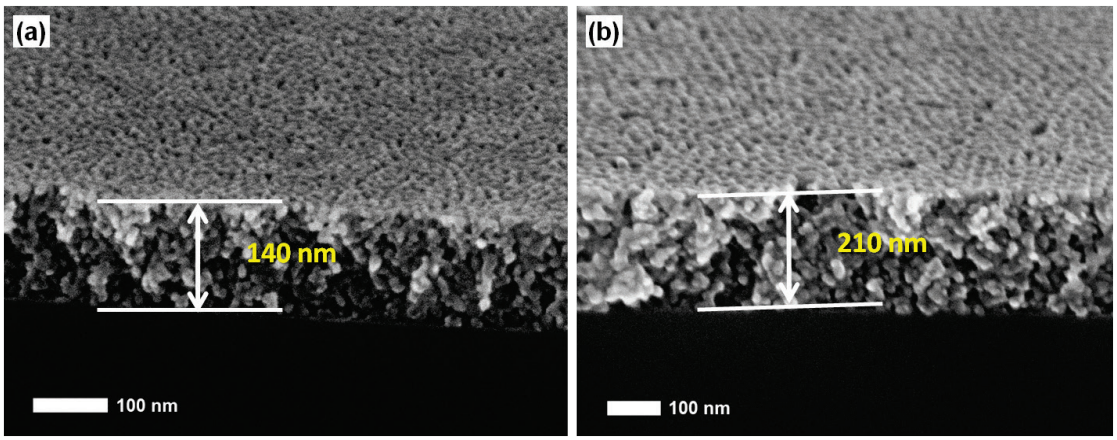

Figure 3.4. SEM images of titania films structure-directed from copolymers IO7K (a) and IO41K (b). Both films showed crack-free and uniform coverage of the substrate. From the SEM results the pore size appeared to be smaller than in titania films from IO92K.

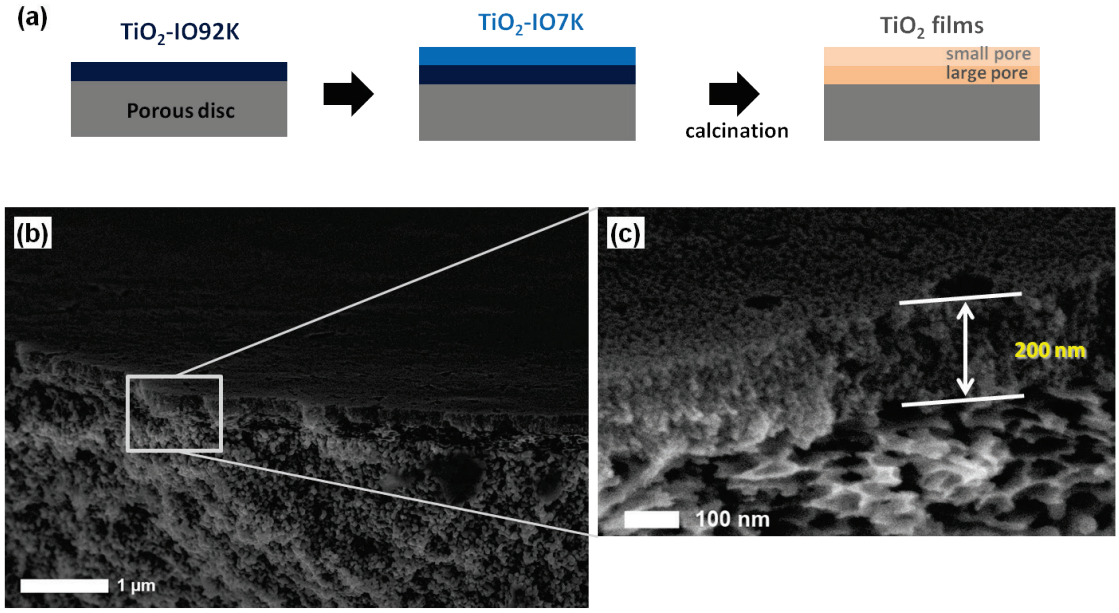

Figure 3.5. Schematic of layer-by-layer process for small pore titania thin film membrane formation from copolymer IO7K (a). To this end first a TiO_2-IO92K hybrid thin film and subsequently a TiO_2-IO7K thin layer are spin-coated on top of each other to prevent infiltration of the smaller polymer into the porous disc substrate. Calcination of the bilayer provides a mesoporous film with hierarchical porosity with a small pore size titania top layer from IO7K over a larger pore size titania layer from IO92K which itself sits on the yet larger pore size substrate as shown in SEM images (b,c).

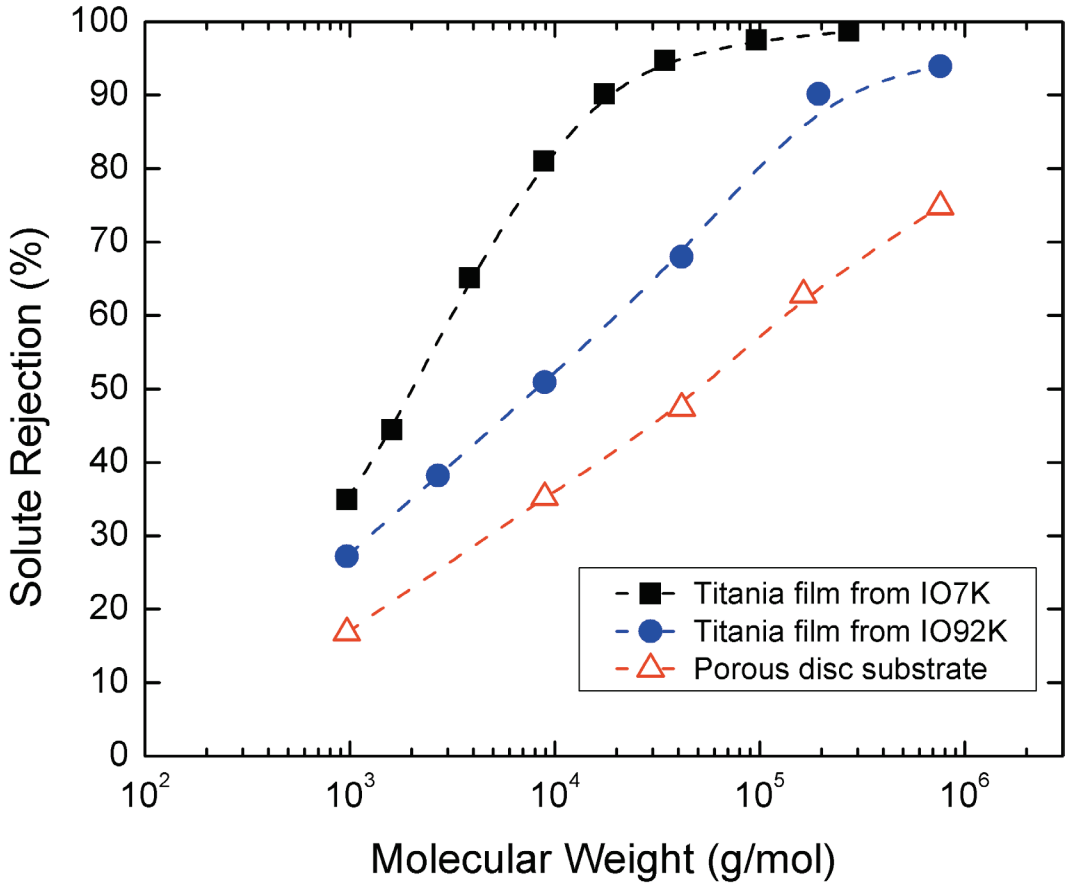

Figure 3.6. Transport behavior through mesoporous titania membranes structure directed from copolymers IO7K and IO92K on top of a porous disc substrate versus that of the parent substrate. A dextran mixture of various molar masses was used as a feed solution and the permeate solutions were analyzed by high performance liquid chromtography (HPLC). Values for the molecular weight cut-off (MWCO) at 90% rejection were ~17 kg/mol and ~200 kg/mol for the mesoporous titania films from IO7K and IO92K, respectively.

Table 3.2. The permeability of pure DI water for mesoporous titania membranes

	Titania film (IO7K)	Titania film (IO92K)
Permeability (L $m^{-2}hr^{-1}bar^{-1}$)	293.5	426.9

Supporting Information

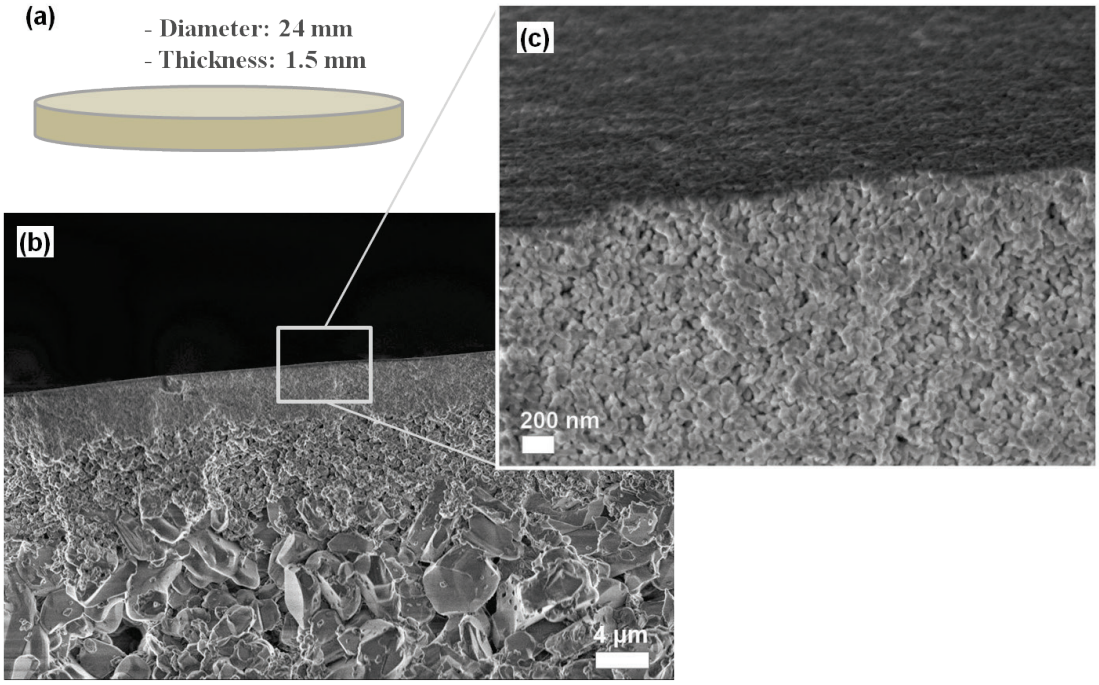

Figure S1. A schematic figure of the asymmetric porous ceramic disc (Keraflex) support (a) and SEM cross sectional images at two magnifications (b,c). The top surface of the disc has ~60 nm random pores while the substrate has an asymmetric pore structure that is composed of coarse ceramic particles of sizes up to several microns.

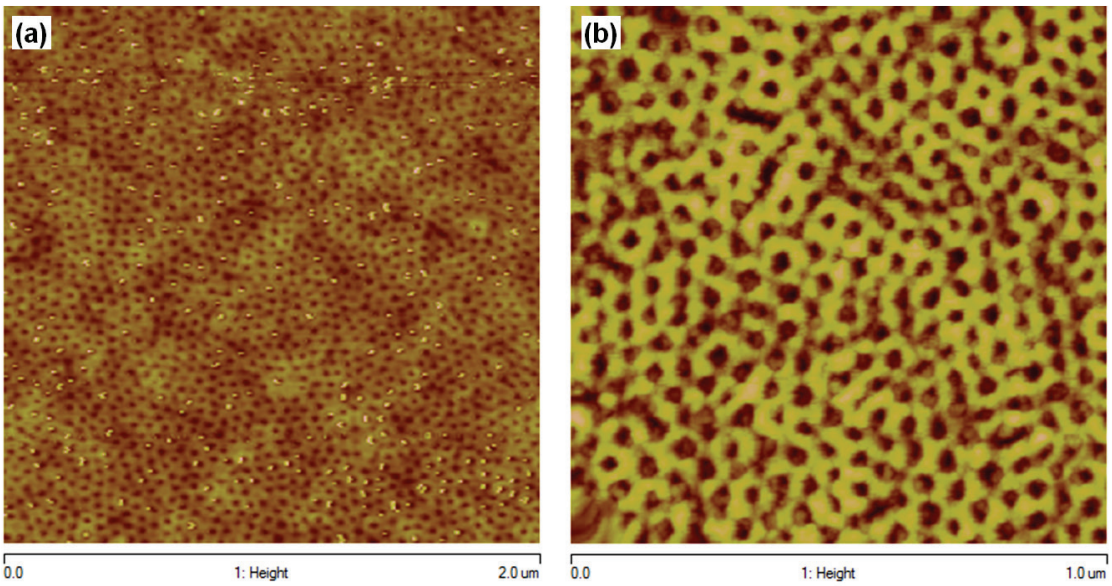

Figure S2. AFM images of as-coated TiO_2-IO92K hybrid film on Si substrate (a) and the corresponding titania film after calcination at 450 °C for 4 hrs (b). The pore size is about 30 nm with relatively narrow pore size distribution (b).

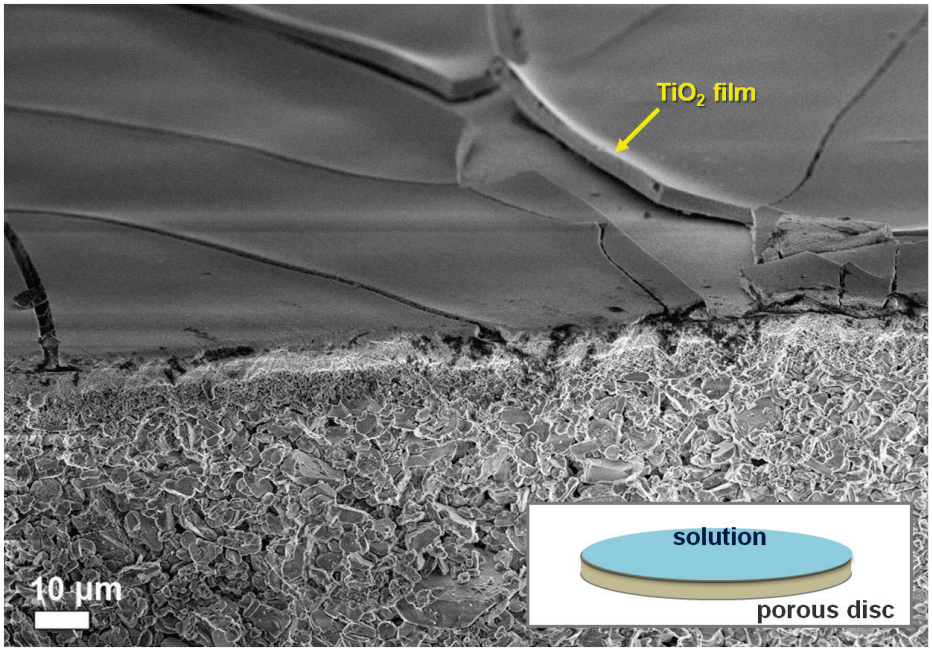

Figure S3. SEM cross-sectional view of TiO_2-IO92K drop-cast film on porous substrate (see schematic in inset). An over 4 µm thick film was formed on the substrate surface causing major cracks.

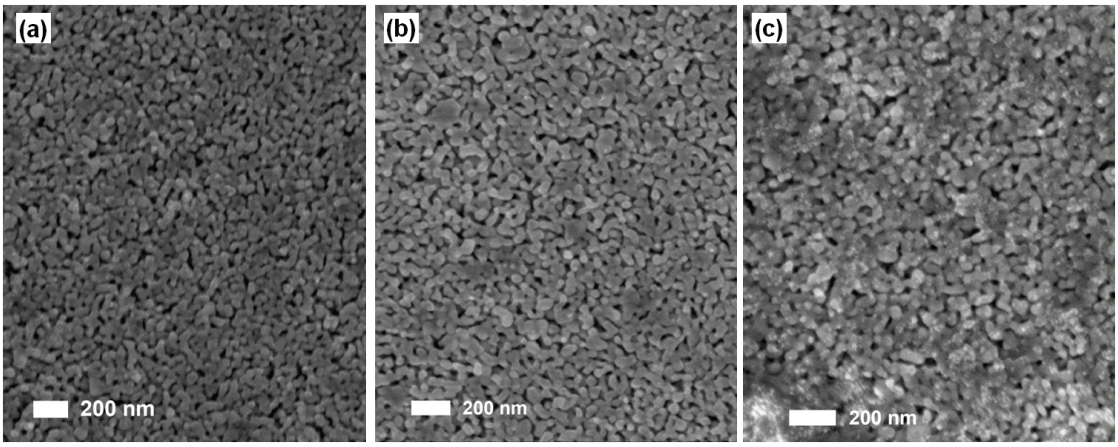

Figure S4. SEM images of top surface of spun-coat TiO_2-IO7K samples on porous discs: varying amounts of solvent were added to the same amount of polymer leading to the following polymer concentrations: 2.1 wt.% (a), 2.7 wt.% (b), and 3.5 wt.% (c). None of the disc substrates were completely covered with titania film. Higher polymer concentrations gave more surface roughness.

References

1. Wang, L.K., et al., *Membrane and Desalination Technologies (Handbook of Environmental Engineering)* 2010: Humana Press.
2. Elimelech, M. and W.A. Phillip, *The Future of Seawater Desalination: Energy, Technology, and the Environment.* Science, 2012. **333**(6043): p. 712-717.
3. Li, N.N., et al., *ADVANCED MEMBRANE TECHNOLOGY AND APPLICATIONS*. 2008: Wiley-AIChE.
4. Larbot, A., et al., *NEW INORGANIC ULTRAFILTRATION MEMBRANES - TITANIA AND ZIRCONIA MEMBRANES.* Journal of the American Ceramic Society, 1989. **72**(2): p. 257-261.
5. Sekulic, J., J.E. ten Elshof, and D.H.A. Blank, *A microporous titania membrane for nanofiltration and pervaporation.* Advanced Materials, 2004. **16**(17): p. 1546-+.
6. Bates, F.S., *Polymer-Polymer Phase-Behavior.* Science, 1991. **251**(4996): p. 898-905.
7. Bates, F.S. and G.H. Fredrickson, *BLOCK COPOLYMER THERMODYNAMICS - THEORY AND EXPERIMENT.* Annual Review of Physical Chemistry, 1990. **41**: p. 525-557.
8. Chatterjee, J., S. Jain, and F.S. Bates, *Comprehensive phase behavior of poly(isoprene-b-styrene-b-ethylene oxide) triblock copolymers.* Macromolecules, 2007. **40**(8): p. 2882-2896.
9. Floudas, G., et al., *Poly(ethylene oxide-b-isoprene) diblock copolymer phase diagram.* Macromolecules, 2001. **34**(9): p. 2947-2957.
10. Phillip, W.A., et al., *Self-Assembled Block Copolymer Thin Films as Water Filtration Membranes.* Acs Applied Materials & Interfaces, 2010. **2**(3): p. 847-853.
11. Phillip, W.A., et al., *Tuning Structure and Properties of Graded Triblock Terpolymer-Based Mesoporous and Hybrid Films.* Nano Letters, 2011. **11**(7): p. 2892-2900.
12. Alberius, P.C.A., et al., *General predictive syntheses of cubic, hexagonal, and lamellar silica and titania mesostructured thin films.* Chemistry of Materials, 2002. **14**(8): p. 3284-3294.
13. Cecilia Fuertes, M., et al., *Sorption properties of mesoporous multilayer thin films.* Journal of Physical Chemistry C, 2008. **112**(9): p. 3157-3163.
14. Chandra, D., et al., *Connectivity of PS-b-PEO templated spherical pores in titanium oxide films.* Physical Chemistry Chemical Physics, 2011. **13**(27): p. 12529-12535.

15. Coquil, T., et al., *Thermal Conductivity of Ordered Mesoporous Titania Films Made from Nanocrystalline Building Blocks and Sol-Gel Reagents.* Journal of Physical Chemistry C, 2010. **114**(29): p. 12451-12458.

16. Krins, N., et al., *Thick and Crack-Free Nanocrystalline Mesoporous TiO2 Films Obtained by Capillary Coating from Aqueous Solutions.* Chemistry of Materials, 2010. **22**(23): p. 6218-6220.

17. Malfatti, L., et al., *One-Pot Route to Produce Hierarchically Porous Titania Thin Films by Controlled Self-Assembly, Swelling, and Phase Separation.* Chemistry of Materials, 2009. **21**(13): p. 2763-2769.

18. Ortel, E., et al., *New Triblock Copolymer Templates, PEO-PB-PEO, for the Synthesis of Titania Films with Controlled Mesopore Size, Wall Thickness, and Bimodal Porosity.* Small, 2012. **8**(2): p. 298-309.

19. Schattka, J.H., et al., *Sol-gel templating of membranes to form thick, porous titania, titania/zirconia and titania/silica films.* Journal of Materials Chemistry, 2006. **16**(15): p. 1414-1420.

20. Szeifert, J.M., et al., *Multilayered High Surface Area "Brick and Mortar" Mesoporous Titania Films as Efficient Anodes in Dye-Sensitized Solar Cells.* Chemistry of Materials, 2012. **24**(4): p. 659-663.

21. Wu, Q.L., N. Subramanian, and S.E. Rankin, *Hierarchically Porous Titania Thin Film Prepared by Controlled Phase Separation and Surfactant Templating.* Langmuir, 2011. **27**(15): p. 9557-9566.

22. Scalarone, D., et al., *Porous and worm-like titanium dioxide nanostructures from PS-b-PEO block copolymer micellar solutions.* Materials Chemistry and Physics, 2011. **128**(1-2): p. 166-171.

23. Robben, L., et al., *Facile Synthesis of Highly Ordered Mesoporous and Well Crystalline TiO2: Impact of Different Gas Atmosphere and Calcination Temperatures on Structural Properties.* Chemistry of Materials, 2012. **24**(7): p. 1268-1275.

24. Ju, X.S., et al., *Studies on the preparation of mesoporous titania membrane by the reversed micelle method.* Journal of Membrane Science, 2002. **202**(1-2): p. 63-71.

25. Jing, W., et al., *Fabrication of Supported Mesoporous TiO2 Membranes: Matching the Assembled and Interparticle Pores for an Improved Ultrafiltration Performance.* Acs Applied Materials & Interfaces, 2009. **1**(7): p. 1607-1612.

26. Dong, Z., W. Jing, and W. Xing, *Triblock polymer template assisted sol-gel process for fabrication of multi-channel TiO2/ZrO2 ultrafiltration membrane.* Journal of Membrane Science, 2011. **373**(1-2): p. 167-172.

27. Warren, S.C., F.J. Disalvo, and U. Wiesner, *Nanoparticle-tuned assembly and disassembly of mesostructured silica hybrids.* Nature Materials, 2007. **6**(2): p.

156-U23.

28. Allgaier, J., et al., *Synthesis and characterization of poly[1,4-isoprene-b-(ethylene oxide)] and poly[ethylene-co-propylene-b-(ethylene oxide)] block copolymers.* Macromolecules, 1997. **30**(6): p. 1582-1586.

29. Arora, H., et al., *Block Copolymer Self-Assembly-Directed Single-Crystal Homo- and Heteroepitaxial Nanostructures.* Science, 2010. **330**(6001): p. 214-219.

30. Du, P., et al., *Additive-driven phase-selective chemistry in block copolymer thin films: The convergence of top-down and bottom-up approaches.* Advanced Materials, 2004. **16**(12): p. 953-+.

31. Stefik, M., et al., *Networked and chiral nanocomposites from ABC triblock terpolymer coassembly with transition metal oxide nanoparticles.* Journal of Materials Chemistry, 2012. **22**(3): p. 1078-1087.

32. Stefik, M., et al., *Ordered Three- and Five-ply Nanocomposites from ABC Block Terpolymer Microphase Separation with Niobia and Aluminosilicate Sols.* Chemistry of Materials, 2009. **21**(22): p. 5466-5473.

CHAPTER 4

MESOPOROUS TUNGSTEN-DOPED TITANIUM DIOXIDE FOR PEM FUEL CELL CATALYST SUPPORT MATERIALS

Abstract

One of the current issues for proton-exchange membrane (PEM) fuel cells to be commercially available for automotive applications is the durability of catalyst support materials. Carbon black materials are not thermodynamically stable at the fuel cell operating conditions and tungsten-doped titania in the rutile structure has been investigated as an alternative. It was previously reported that this material gives comparable activity as carbon blacks and would provide superior performance if the surface area could be increased by better mesostructure control that can be achieved by the self-assembly based structure formation of metal oxides from amphiphilic block copolymers. Here, we explored the mesoporous mixed oxide formation of $Ti_{1-x}W_xO_2$ structure-directed from PI-*b*-PEO combined with a two-step heat processing approach. As-made hybrid films as well as amorphous metal oxide/carbon composites after the first heat treatment were indeed well ordered. However, the second higher temperature step caused problems such as collapse of mesoporosity and segregation of metal oxide crystalline phases. To avoid these problems, we suggest (1) milder reduction conditions to prevent excessive diffusion of metal oxides and (2) a non-chlorine containing system as even trace amounts of chlorine promote the transport of tungsten causing phase segregation.

Introduction

As the world demand for energy has increased substantially alternative energy sources have been widely studied and developed over the past few decades [1]. Alternative energy devices such as batteries and fuel cells are electrochemical systems that convert chemical energy into electrical energy or vice versa, involving chemical reactions and transport problems. Self-assembly based nanostructure formation of inorganic materials by block copolymers (BCPs) is a promising route to materials for these applications as it provides mesoporosity at the 5-50 nm length scale, short transport distances and high surface area that are all beneficial to electrochemical devices [2, 3]. Numerous well-ordered inorganic nanomaterials structure directed by BCPs have been reported including silicates [4-7], transition metal oxides [8-20], non-oxide ceramics [21, 22], and metals [23, 24].

Proton-exchange membrane (PEM) fuel cells have been intensively investigated and developed in academia and industry for automotive and hand-held electronics applications due to their high efficiency, zero emission, and low temperature operation. Considerable challenges remain for PEM fuel cells in order to become commercially available and even competitive, however, including high materials costs from precious metal catalysts and durability problems [25, 26]. The current catalyst support, carbon black, imposes durability issues to PEM fuel cells. It has poor thermodynamic stability under fuel cell operation conditions: highly acidic, low pH and high electrode potentials up to at least 1.5 V with respect to the standard hydrogen electrode (SHE). Although the kinetics of corrosion can be quite slow depending on the type of carbon black, a 5% to 10% loss of carbon within 100 hours

was reported when operated at 1.2 V, which generally leads to commercially unacceptable fuel cell performance. This can imply that standard carbon supports (Vulcan-XC72 and Ketjen black) do not satisfy automotive requirements [27]. The requirements for catalyst supports include (1) stability or meta-stability at low pH (0-2) and high electrode potentials up to 1.5 V (vs SHE), (2) electrical conductivity which is greater than 0.1 S/cm, (3) high surface area for catalytic activity, and (4) mechanical strength.

Tungsten-doped titanium dioxide (titania) with rutile structure was reported to have the potential to replace conventional carbon black as catalyst support. Titania is known as a stable material under fuel cell operating conditions[28], but does not have good conductivity due to its semiconducting properties. Doping of tungsten was reported to lead to in-plane expansion and c-axis contraction of its rutile structure providing electrical conductivity at wide doping levels (10-50 %) [29]. More recently, Subban *et al.* reported tungsten-doped titania with rutile structure in the form of nanoparticles of 20-100 nm size derived from a sol-gel approach. Electrochemical testing of this catalyst support with Pt impregnation showed high activity per unit Pt surface area comparable to that of Pt/Vulcan, but the mass activity was low mainly due to low specific surface areas [30-32].

Here we report on tungsten-doped titanium oxide structure-directed by a highly amphiphilic block copolymer, poly(isoprene-*b*-ethylene oxide) (PI-*b*-PEO) using a solution process. First, an amorphous mixed oxide of titania (TiO_2) and tungsten oxide (WO_3) is prepared using PI-*b*-PEO as structure-directing agent, followed by two distinct heat-processing steps. In the first heat treatment referred to as the CASH

method,[10] the as-made material is converted into a mesoporous, but in the present case still amorphous, material with in-situ formed carbon providing a scaffold within the pores. In the second, higher temperature heat-treatment conducted in a sealed tube a reduction process leads to crystallized tungsten-doped titania, ideally under preservation of the mesostructure. The challenges here are (1) to synthesize the mesoporous mixed oxide with controlled morphology and (2) to obtain the desired doped crystalline oxide without structure collapse. The latter is non-trivial as the crystallization of the metal oxide into the rutile structure comes with a large change in density and thus volume leading to considerable internal stresses in the material. Synthesis efforts were conducted with doping levels of 10 % and 30 % tungsten. Materials obtained at different processing stages were characterized using a combination of small-angle X-ray scattering (SAXA), transmission electron microscopy (TEM), scanning electron microscopy (SEM), wide-angle X-ray diffraction (XRD) and nitrogen adsorption-desorption measurements.

Experimental Section

Materials

Tetrahydrofuran (anhydrous, >99.9%, Aldrich), titanium isopropoxide (97%, Aldrich), tungsten(VI) ethoxide (Alfa Aesar) and concentrated hydrochloric acid (37wt% ACS grade, BDH Aristar) were used as received. Poly(isoprene-*b*-ethylene oxide) (PI-*b*-PEO) was synthesized by anionic polymerization using reported procedures [33, 34]. The PI-*b*-PEO had a total molar mass of 28 kg/mol with 28 wt.% PEO and a polydispersity index, PDI, of 1.06.

Sample Preparation

Mixed oxide hybrid materials of TiO_2 and WO_3 with 10 % tungsten were synthesized as follows: 50 mg of PI-*b*-PEO was dissolved in 6 ml of tetrahydrofuran (THF) under stirring for about 1 hour. A tungsten-containing sol (W-sol) was prepared by the addition of 0.5 ml of anhydrous ethanol and 2 ml of THF into 0.055 g of tungsten(VI) ethoxide followed by stirring for about 20 min. In order to obtain a titanium-containing sol (Ti-sol), 0.32 ml of titanium(IV) isopropoxide was added into 0.103 ml of concentrated hydrochloric acid (37 %) and the solution was stirred for 5 min. Subsequently, 5 ml of THF were added to stabilize the Ti-sol with stirring for another 5 min. Then W-sol and Ti-sol were added to the polymer solution and subsequently stirred for an hour before the solution was cast in a teflon dish placed within a glass dish (bottom) and a glass hemisphere (top) on a hotplate to slow down evaporation. The hot plate was set to 50 °C so that the effective casting temperature was about 40 °C. After 24 hrs of drying, the films were moved to an oven set to 100 °C for 24 hrs to enhance the condensation reaction. The added chemicals were chosen to result in a mass ratio of inorganic to polymer components of ~2.2 thereby aiming at an inverse hexagonal structure according to similar and published systems [7]. For the hybrid materials with 30 % tungsten content, the amounts of tungsten and titanium precursors were adjusted to give the same inorganic to polymer ratio for the same amount of PI-*b*-PEO polymer used. Hybrid materials obtained from this preparation step are referred to as as-made films in this paper.

For obtaining doped crystalline materials with preserved mesoporous structure,

the as-made films were heat-treated in a two-step process as described in Figure 4.1. The first heat treatment was performed under nitrogen at 500 °C to form amorphous mixed oxides with carbon scaffold as previously reported [10]. The reduction of tungsten (+6) to (+4) oxidation state was subsequently carried out in a sealed and evacuated silica tube at 750 °C for a day in the presence of Zirconium metal as described in detail elsewhere[31], producing tungsen-doped rutile titania and carbon composites. All heat treatments utilized a 1-2 °C/min heating ramp rate followed by natural furnace cooling to room temperature.

Characterization

Transmission electron microscopy (TEM) was conducted using a Technai T12 instrument operating at 120 kV. As-made films were cut into thin slices of ~70 nm at -60 °C using a Leica Ultracut UCT microtome that were collected onto 400 mesh copper TEM grids. Small angle X-ray scattering (SAXS) data on nanocomposite samples were collected at the Cornell High Energy Synchrotron Source (CHESS) with a multilayer monochromater (λ=1.547 Å) with a 2D area detector and are presented as 1D plots of radially integrated intensity versus the scattering vector q, where $q=\frac{4\pi\sin\theta}{\lambda}$ and 2θ is the total scattering angle. Crystalline phases were characterized by powder X-ray diffraction (XRD) using a Rigaku Ultima VI diffractometer. Scanning electron microscopy (SEM) and energy dispersive X-ray analysis (EDX) were performed using a LEO-1550 field emission SEM instrument. Thermogravimetric analysis (TGA) was conducted using a TA Instruments Q50.

Nitrogen physisorption isotherms were measured at -196 °C using a Micromeritics ASAP 2020 system. All samples were degassed under high vacuum at 120 °C overnight prior to measurements. The Brunaure, Emmett, and Teller (BET) and Brunauer, Jonyer, and Halenda (BJH) analyses were performed using Micromeritics ASAP 2020 V1.05 software. Rotating disc electrode (RDE) electrochemical experiments were carried out for $Ti_{0.9}W_{0.1}O_2$/carbon composites in 0.1 M H_2SO_4 at room temperature using a Solartron electrochemistry station after the composites were mixed with Nafion solution. A detailed description of the electrochemical measurement procedure can be found elsewhere [30].

Results and Discussion

Highly ordered hybrid samples of mixed oxides of TiO_2 and 10 % WO_3 were prepared using PI-*b*-PEO as structure directing agent. The resulting material structure was characterized by a combination of SAXS and TEM measurements. The inorganic to polymer mass ratio for these hybrid films was aimed at 2.2 and was expected to lead to an inverse hexagonal structure according to a similar, previously reported PI-*b*-PEO based morphology diagram [7]. The representative radially integrated 1D SAXS pattern and TEM images in Figure 4.2 show that as-made films indeed have highly ordered inverse hexagonal morphology. The SAXS pattern was indexed with a hexagonal lattice with values of higher order peak positions at $q/q^* = 1, \sqrt{3}, \sqrt{4}, \sqrt{7}$ of the position of the first order maximum, q^*. The d_{10}-spacing for this sample was calculated as 32.2 nm corresponding to a unit cell parameter, a_0, of 37.2 nm. TEM images at different magnifications confirm the hexagonal mesostructure and suggest a

d_{10}-spacing of ~27 nm, see inset of Figure 4.2.

The first heat treatment was carried out on as-made films at 500 °C for 4 hrs under nitrogen as described in Figure 4.1. From previous results this step was expected to provide a graphitic carbon scaffold resulting from the carbonization of sp^2 hybridized carbon atoms of the PI block and preventing pore collapse from density changes during crystallization of metal oxides at higher temperatures during the second heat treatment [10]. Figure 4.3 shows characterization results of the metal oxide/carbon composites after the first heat treatment. The SEM image (a) reveals a preserved ordered hexagonal structure while TGA analysis (b) suggests about 8-9 % residual carbon material. An XRD spectrum (c) with only marginal crystalline features suggests that the composite is made of mostly amorphous material with a small amount of crystalline anatase phase. From these analyses it can be concluded that the materials after the first heating step are essentially mesoscopically ordered mixed oxide/carbon composites.

The subsequent high temperature reduction process was performed with the amorphous mixed oxide/carbon composites in an evacuated and sealed silica tube. Water was carefully removed by pulling vacuum under gentle heating using a heat gun before the tube was sealed, as water is known as a good transport agent of tungsten at high temperatures and would thus disturb the proper reduction of tungsten [35]. The SEM image of the final product in Figure 4.4(a) shows large nanoparticles of 20-100 nm size embedded in a mesoporous carbon-type structure. EDX analysis through line scans shows that Ti and W are distributed almost uniformly over the entire sample, suggesting a homogeneous mixture of the oxides (Figure S1). The XRD spectrum in

Figure 4.4(c) further suggests a single rutile phase crystalline material implying that the properly doped $Ti_{0.9}W_{0.1}O_2$/carbon composite was formed, consistent with the EDX results. From these results the carbon scaffold did not seem to be strong enough to prevent the growth of large crystalline oxide particles during the reduction step. To overcome this problem it may be helpful to perform the second heat processing at somewhat lower temperature or for shorter periods of time to prevent excessive diffusion of metal oxides. Another possible cause of the excessive particle growth is chlorine from hydrochloric acid (HCl) that was used to stabilize titania sols for the self-assembly process with PI-*b*-PEO. Chlorine is a very good tungsten-transport agent at high temperature and can promote the diffusion of tungsten oxide even if there is only a very small amount in the system. To avoid this problem, strong acids other than HCl would need to be utilized in the materials synthesis.

Although the desired mesostructure was not formed, nitrogen adsorption/desorption measurements (Figure 4.4b) showed large surface areas of around 90 m^2/g and average pore sizes of 17-18 nm with relatively narrow pore size distributions. Furthermore, rotating disc electrochemical (RDE) tests were carried out (Figure 4.5) after $Ti_{0.9}W_{0.1}O_2$/carbon composites were sonicated in a 5 wt % ethanol solution of Nafion and the solution subsequently put on a glassy carbon electrode of 5 mm size and dried in air. This simple electrochemical test at various electrode potentials (0.5-1.2 V) with constant sweep rate of 50 mV/s indicated that the composites are conducting materials.

Mesoporous mixed oxide hybrid films from 30 % tungsten were prepared using the same approach. The as-made films show highly ordered inverse hexagonal

morphology as confirmed by SAXS and TEM measurements (Figure S2). The first heat treatment using the same conditions as reported for the $Ti_{0.9}W_{0.1}O_2$/carbon composites showed an amorphous phase with preserved mesostructure (Figure S3a,b). The second heat processing gave a mixed crystalline phase of rutile $Ti_{0.7}W_{0.3}O_2$, WO_2 and anatase TiO_2 (Figure S4c) while the mesostructure was partially preserved as can be inferred from the TEM image in Figure S4a. Nitrogen physisorption measurements signaled large BET surface areas of around 100 m^2/g and average pore size of ~15 nm (Figure S4b).

In summary, we successfully synthesized mixed oxides from TiO_2 and 10 % and 30 % WO_3, respectively, structure-directed by a PI-*b*-PEO diblock copolymer. The ordered hexagonal mesostructure of the as-made composites was preserved upon a first heat treatment to 500 °C forming amorphous mixed metal oxides together with a carbon support. During a second heat treatment in a sealed tube to 750 °C in the presence of zirconium metal as a reducing agent the 30% W containing sample was converted to a single rutile phase crystalline material with large oxide nanoparticles embedded in a mesoporous carbonaceous matrix. The 10% doped sample formed a mesoporous mixed crystalline phase of both oxides. Both samples showed high surface areas around 100 m^2/g and average pore sizes of ~15-18 nm. Furthermore, the highly doped sample showed conductivity in electrochemical tests. In order to obtain well ordered single phase materials with high doping levels we suggest that (1) the reduction process is carried out at lower temperature and/or for shorter periods of time to minimize excessive diffusion of metal oxides, and (2) other strong acids besides HCl are utilized for titanium sol stabilization.

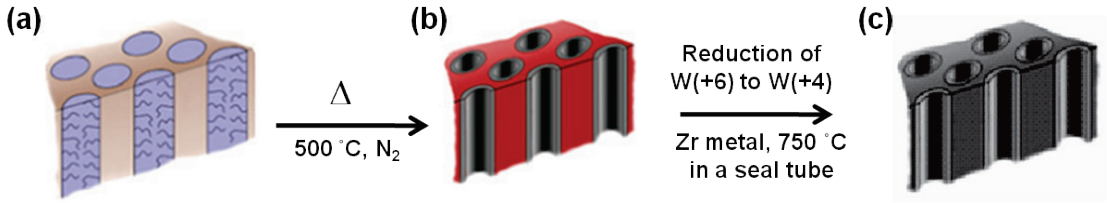

Figure 4.1. Schematic process for mesoporous tungsten-doped titania formation from as-made films (a). The first heat treatment is done under nitrogen at 500 °C to form amorphous mixed oxides with carbon scaffold (b) [Lee, Nat. Mater. 2008]. The second heat processing is carried out in a sealed tube at 750 °C for 24 hrs with zirconium metal foil reducing tungsten from oxidation state (+6) to (+4) providing a tungsten doped rutile/carbon composite $Ti_{1-x}W_xO_2$/carbon (c).

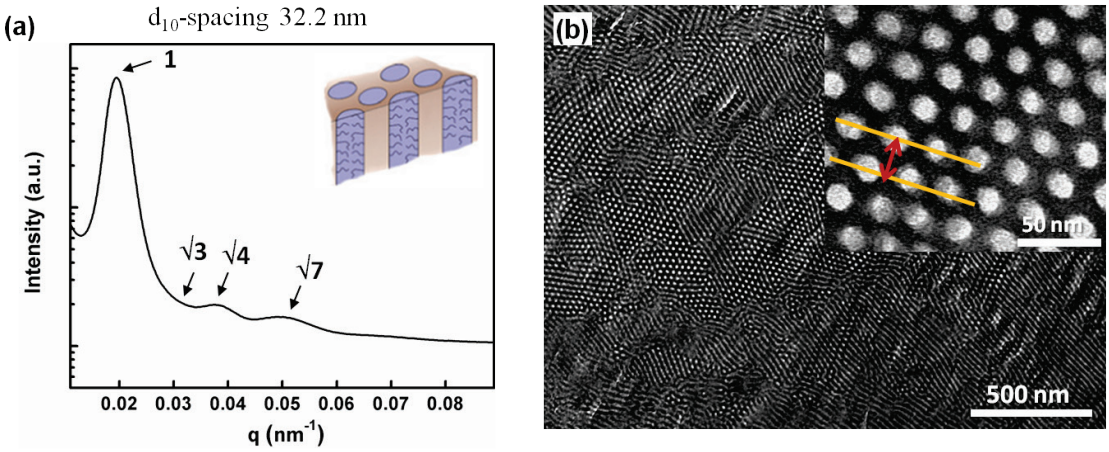

Figure 4.2. Representative SAXS pattern and corresponding TEM images for the as-made mixed oxide film with 10 % tungsten. The SAXS pattern was indexed with a hexagonal lattice ($q/q^* = 1, \sqrt{3}, \sqrt{4}, \sqrt{7}$ etc) and the first order peak at q^* reflects a d_{10}-spacing of 32.2 nm, corresponding to a unit-cell parameter $a_0 = 37.2$ nm. The TEM image shows a well-ordered hexagonal structure with an estimated d_{10}-spacing of ~ 27 nm, see inset in (b).

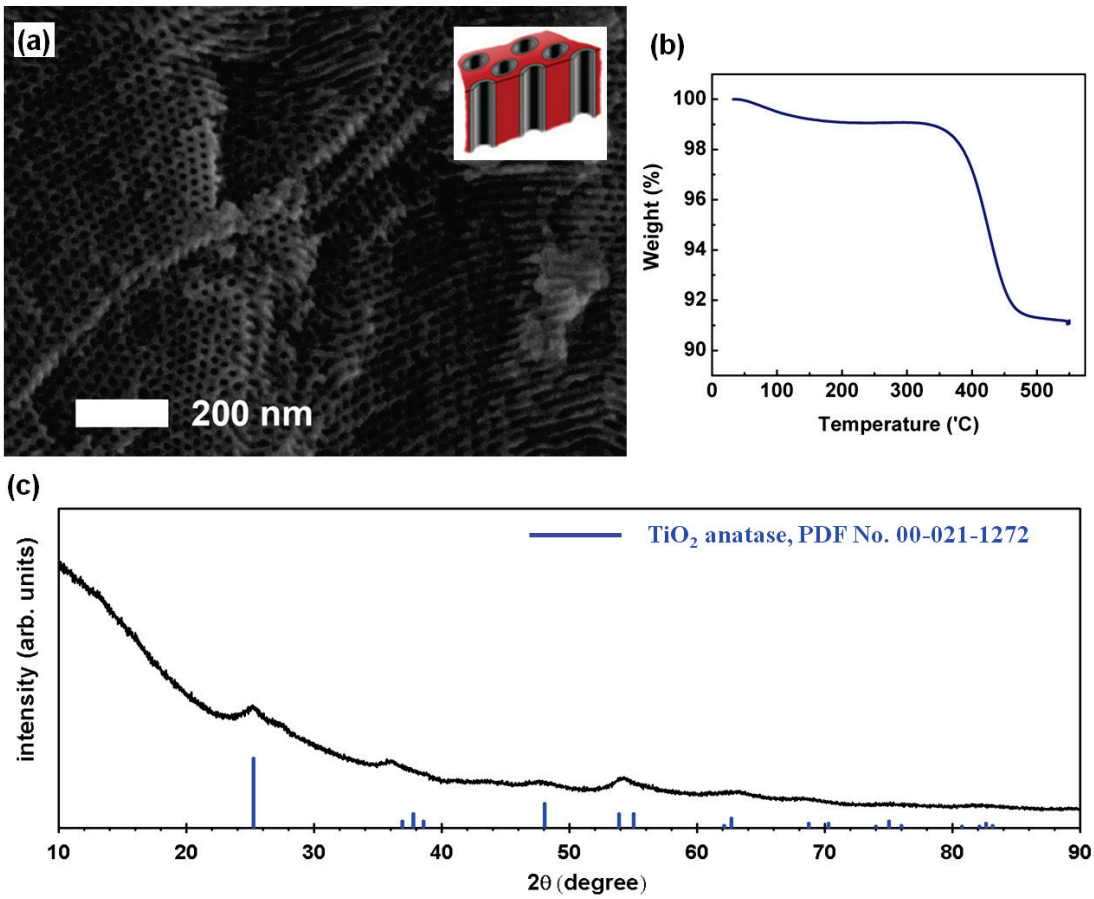

Figure 4.3. SEM image (a), TGA analysis (b), and wide angle X-ray diffraction (c) results for an amorphous mixed oxide/carbon composite with 10 % tungsten after the first heat treatment at 500 °C for 4 hrs under nitrogen. The SEM image shows a highly ordered hexagonal structure after heating with a corresponding weight loss of 8.8 % as obtained from TGA analysis. The XRD spectrum suggests that this composite mostly consists of amorphous material.

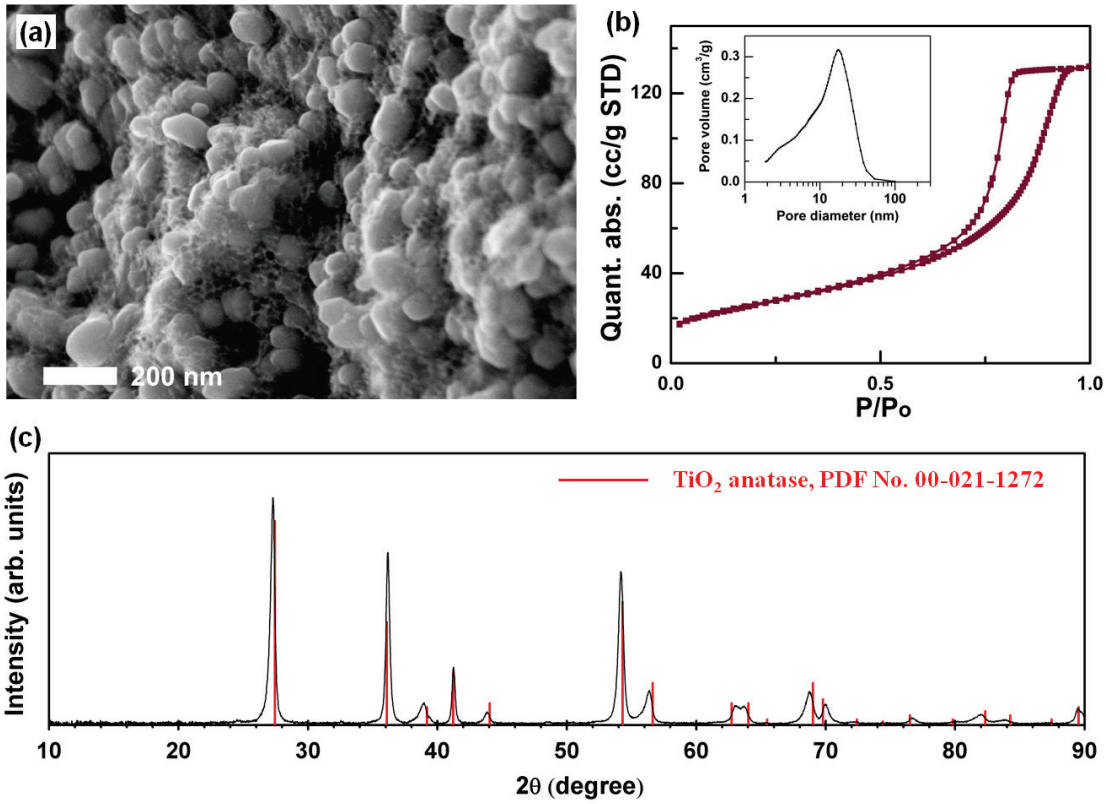

Figure 4.4. SEM image (a), Nitrogen adsorption/desorption measurement results (b), and wide angle X-ray diffraction pattern (c) for the reduced $Ti_{0.9}W_{0.1}O_2$/carbon composite. This composite appears to consists of nanoparticles of 20-100 nm size in the mesoporous network structure as shown in the SEM image (a). BET analysis of the adsorption/desorption measurments suggest a high BET surface area of 92.7 m^2/g and BJH average pore size of 17.6 nm (b). The XRD pattern shows that after reduction this composite consists of doped $Ti_{0.9}W_{0.1}O_2$ rutile crystalline structure.

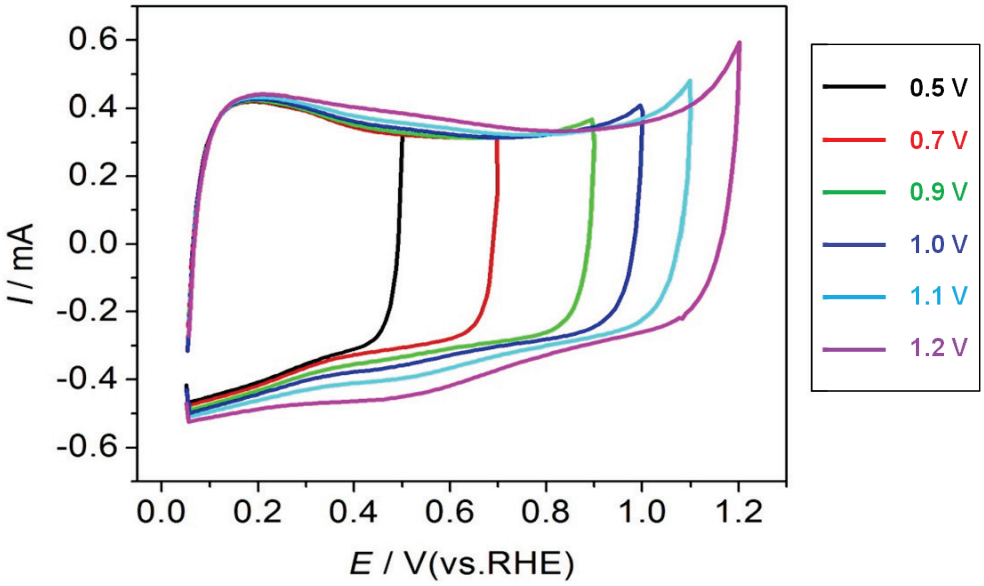

Figure 4.5. Rotating disc electrochemical (RDE) results for $Ti_{0.9}W_{0.1}O_2$/carbon composites with Nafion on glassy carbon electrode in N_2-saturated 0.1 M H_2SO_4 show the composite is a conducting material. Various potentials (0.5-1.2 V) were applied with constant sweep rate of 50 mV/s.

Supporting Informaton

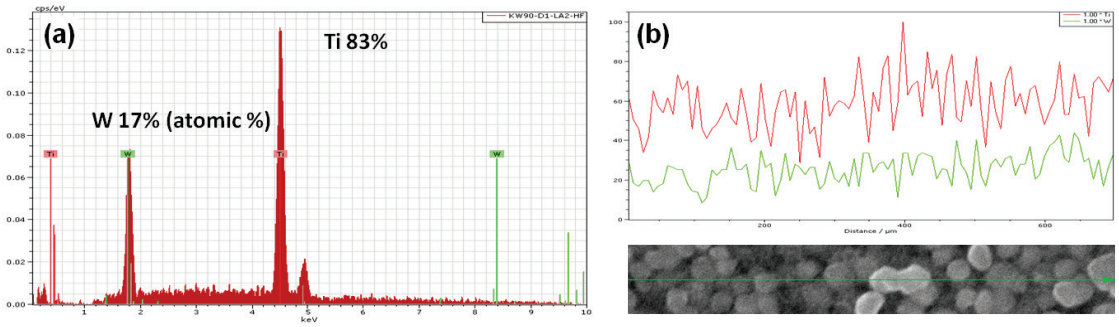

Figure S1. EDX analysis for $Ti_{0.9}W_{0.1}O_2$/carbon composites show an atomic composition of Ti (83 %) and W (17 %) (a). The EDX line scan reveals that Ti and W atoms are distributed uniformly over the particles, which suggests a homogeneous mixture of the oxides (b).

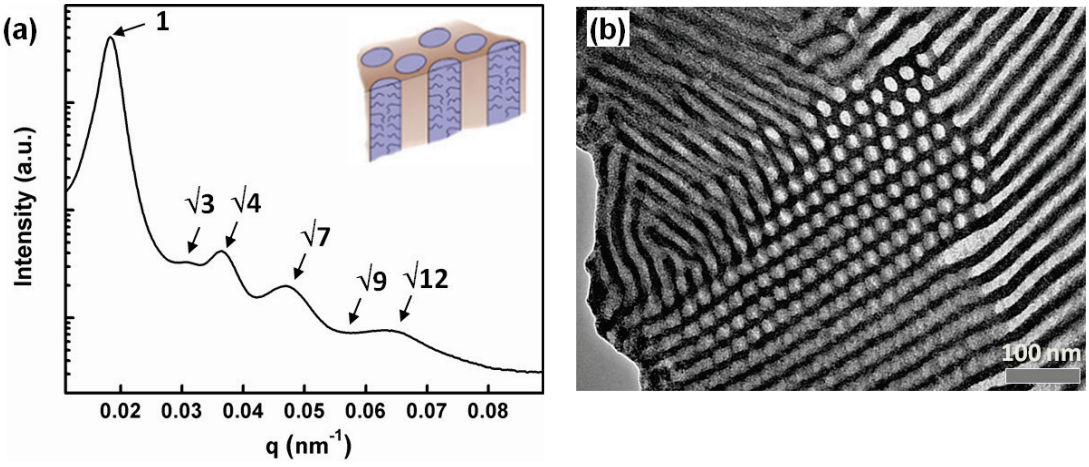

Figure S2. Representative SAXS pattern and corresponding TEM image for an as-made mixed oxide film with 30 % tungsten. The SAXS pattern was indexed with a hexagonal lattice with peak positions at q/q* = 1, √3, √4, √7, √9, √12, The first order peak at q* reflects a d_{10}-spacing of 34.3 nm (a). The TEM image shows a well-ordered hexagonal structure (b).

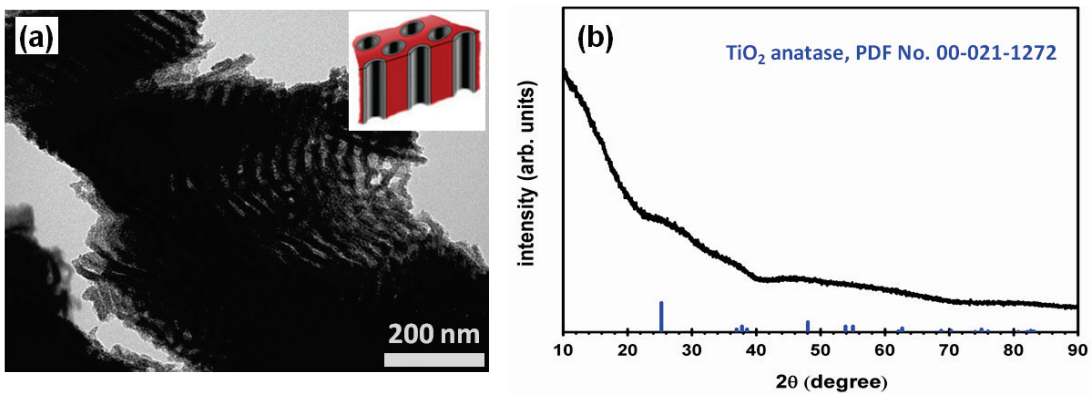

Figure S3. TEM image (a), and wide angle X-ray diffraction (2) results for amorphous mixed oxide and carbon composite for 30 % tungsten after first heat treatment at 500 °C for 4 hrs under nitrogen.

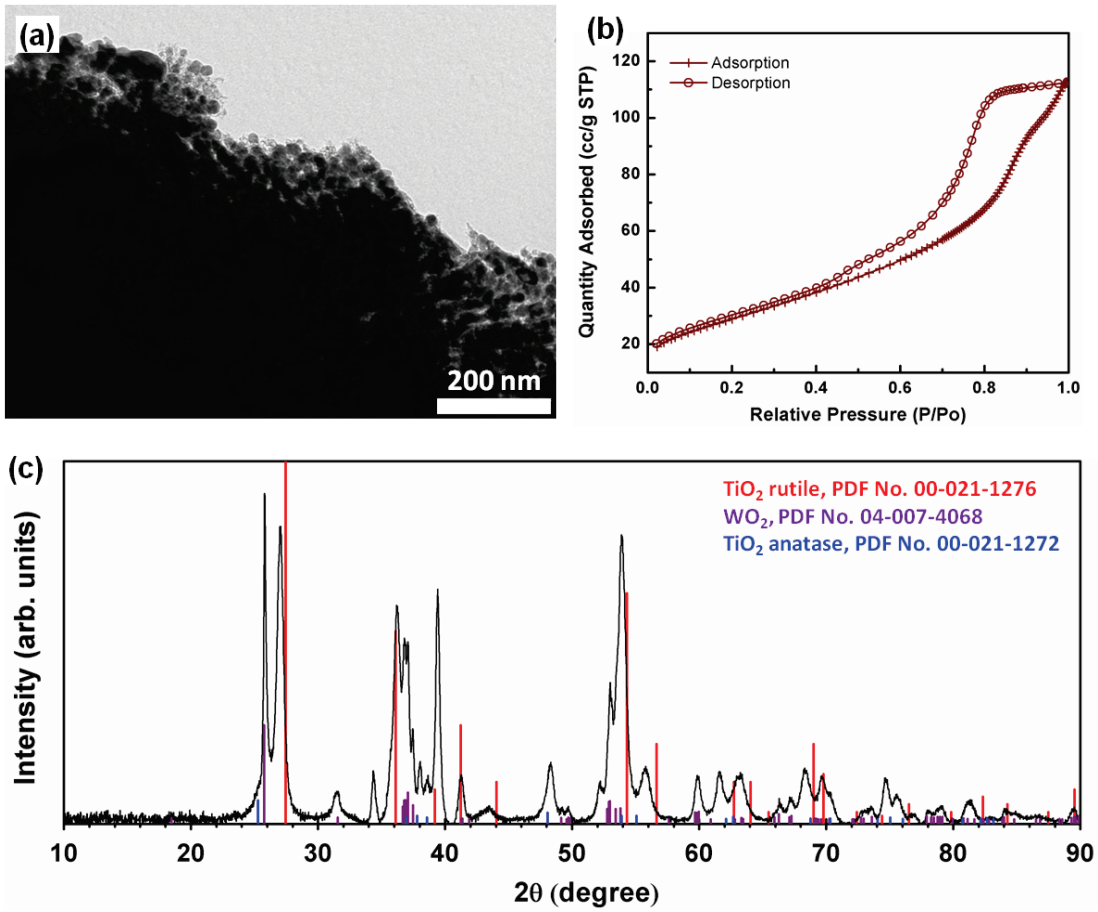

Figure S4. TEM image (a), nitrogen adsorption/desorption isotherms (b), and XRD analysis (c) for $Ti_{0.7}W_{0.3}O_2$/carbon composites. The ordered structure appeared to be destroyed (a) but nitrogen physisorption measurements show a BET surface area of 104.5 m2/g and a BJH mean pore size of ~ 15 nm (b). XRD indicates that this composite has a mixed crystalline phase of rutile $Ti_{0.7}W_{0.3}O_2$ and WO_3.

References

1. MacKay, D.J.C., *Sustainable Energy - without the hot air*. 2008: UIT Cambridge.
2. Bates, F.S., *Polymer-Polymer Phase-Behavior.* Science, 1991. **251**(4996): p. 898-905.
3. Bates, F.S. and G.H. Fredrickson, *BLOCK COPOLYMER THERMODYNAMICS - THEORY AND EXPERIMENT.* Annual Review of Physical Chemistry, 1990. **41**: p. 525-557.
4. Templin, M., et al., *Organically modified aluminosilicate mesostructures from block copolymer phases.* Science, 1997. **278**(5344): p. 1795-1798.
5. Simon, P.F.W., et al., *Block copolymer-ceramic hybrid materials from organically modified ceramic precursors.* Chemistry of Materials, 2001. **13**(10): p. 3464-3486.
6. Renker, S., et al., *Nanostructure and shape control in polymer-ceramic hybrids from poly(ethylene oxide)-block-poly(hexyl methacrylate) and aluminosilicates derived from them.* Macromolecular Chemistry and Physics, 2004. **205**(8): p. 1021-1030.
7. Garcia, B.C., et al., *Morphology Diagram of a Diblock Copolymer-Aluminosilicate Nanoparticle System.* Chemistry of Materials, 2009. **21**(22): p. 5397-5405.
8. Alberius, P.C.A., et al., *General predictive syntheses of cubic, hexagonal, and lamellar silica and titania mesostructured thin films.* Chemistry of Materials, 2002. **14**(8): p. 3284-3294.
9. Antonelli, D.M. and J.Y. Ying, *SYNTHESIS OF HEXAGONALLY PACKED MESOPOROUS TIO2 BY A MODIFIED SOL-GEL METHOD.* Angewandte Chemie-International Edition in English, 1995. **34**(18): p. 2014-2017.
10. Lee, J., et al., *Direct access to thermally stable and highly crystalline mesoporous transition-metal oxides with uniform pores.* Nature Materials, 2008. **7**(3): p. 222-228.
11. Orilall, M.C., et al., *One-Pot Synthesis of Platinum-Based Nanoparticles Incorporated into Mesoporous Niobium Oxide-Carbon Composites for Fuel Cell Electrodes.* Journal of the American Chemical Society, 2009. **131**(26): p. 9389-9395.
12. Orilall, M.C. and U. Wiesner, *Block copolymer based composition and morphology control in nanostructured hybrid materials for energy conversion and storage: solar cells, batteries, and fuel cells.* Chemical Society Reviews, 2011. **40**(2): p. 520-535.
13. Oskam, G., et al., *The growth kinetics of TiO2 nanoparticles from titanium(IV) alkoxide at high water/titanium ratio.* Journal of Physical Chemistry B, 2003.

107(8): p. 1734-1738.

14. Smarsly, B., et al., *Highly crystalline cubic mesoporous TiO2 with 10-nm pore diameter made with a new block copolymer template.* Chemistry of Materials, 2004. **16**(15): p. 2948-2952.
15. Stefik, M., et al., *Ordered Three- and Five-ply Nanocomposites from ABC Block Terpolymer Microphase Separation with Niobia and Aluminosilicate Sols.* Chemistry of Materials, 2009. **21**(22): p. 5466-5473.
16. Stefik, M., et al., *Networked and chiral nanocomposites from ABC triblock terpolymer coassembly with transition metal oxide nanoparticles.* Journal of Materials Chemistry, 2012. **22**(3): p. 1078-1087.
17. Yang, P.D., et al., *Generalized syntheses of large-pore mesoporous metal oxides with semicrystalline frameworks.* Nature, 1998. **396**(6707): p. 152-155.
18. Crossland, E.J.W., et al., *Block Copolymer Morphologies in Dye-Sensitized Solar Cells: Probing the Photovoltaic Structure-Function Relation.* Nano Letters, 2009. **9**(8): p. 2813-2819.
19. Docampo, P., et al., *Control of Solid-State Dye-Sensitized Solar Cell Performance by Block-Copolymer-Directed TiO2 Synthesis.* Advanced Functional Materials, 2010. **20**(11): p. 1787-1796.
20. Nedelcu, M., et al., *Block copolymer directed synthesis of mesoporous TiO2 for dye-sensitized solar cells.* Soft Matter, 2009. **5**(1): p. 134-139.
21. Wan, J.L., et al., *Nanostructured non-oxide ceramics templated via block copolymer self-assembly.* Chemistry of Materials, 2005. **17**(23): p. 5613-5617.
22. Kamperman, M., et al., *Ordered mesoporous ceramics stable up to 1500 degrees C from diblock copolymer mesophases.* Journal of the American Chemical Society, 2004. **126**(45): p. 14708-14709.
23. Warren, S.C., et al., *Ordered mesoporous materials from metal nanoparticle-block copolymer self-assembly.* Science, 2008. **320**(5884): p. 1748-1752.
24. Li, Z.H., et al., *Metal Nanoparticle-Block Copolymer Composite Assembly and Disassembly.* Chemistry of Materials, 2009. **21**(23): p. 5578-5584.
25. Bashyam, R. and P. Zelenay, *A class of non-precious metal composite catalysts for fuel cells.* Nature, 2006. **443**(7107): p. 63-66.
26. Steele, B.C.H. and A. Heinzel, *Materials for fuel-cell technologies.* Nature, 2001. **414**(6861): p. 345-352.
27. Mathias, M.F., *Two Fuel Cell Cars In Every Garage.* The Electrochemical Society Interface, 2005. **14**: p. 24-35.
28. Pourbaix, M., *Atlas of Electrochemical Equilibria in Aqueous Solutions*. 1974: NACE International.

29. Aryanpour, M., R. Hoffmann, and F.J. DiSalvo, *Tungsten-Doped Titanium Dioxide in the Rutile Structure: Theoretical Considerations.* Chemistry of Materials, 2009. **21**(8): p. 1627-1635.

30. Wang, D.L., et al., *Highly Stable and CO-Tolerant Pt/Ti0.7W0.3O2 Electrocatalyst for Proton-Exchange Membrane Fuel Cells.* Journal of the American Chemical Society, 2010. **132**(30): p. 10218-10220.

31. Subban, C.V., et al., *Sol-Gel Synthesis, Electrochemical Characterization, and Stability Testing of Ti0.7W0.3O2 Nanoparticles for Catalyst Support Applications in Proton-Exchange Membrane Fuel Cells.* Journal of the American Chemical Society, 2010. **132**(49): p. 17531-17536.

32. Subban, C., et al., *Catalyst supports for polymer electrolyte fuel cells.* Philosophical Transactions of the Royal Society a-Mathematical Physical and Engineering Sciences, 2010. **368**(1923): p. 3243-3253.

33. Allgaier, J., et al., *Synthesis and characterization of poly[1,4-isoprene-b-(ethylene oxide)] and poly[ethylene-co-propylene-b-(ethylene oxide)] block copolymers.* Macromolecules, 1997. **30**(6): p. 1582-1586.

34. Warren, S.C., F.J. Disalvo, and U. Wiesner, *Nanoparticle-tuned assembly and disassembly of mesostructured silica hybrids.* Nature Materials, 2007. **6**(2): p. 156-U23.

35. Schafer, H., *Chemical transport reactions*. 1964, New York: Academic Press.

CHAPTER 5

MORPHOLOGY DIAGRAM OF ABC TRIBLOCK TERPOLYMER AND INORGANIC NANOPARTICLE SYSTEM: TOWARD THE ORDERED NETWORK STRUCTURES

Abstract

The self-assembly based structure direction of inorganic metal oxides using block copolymers is a promising route to functional composite nanomaterials. ABC triblock terpolymers have been previously reported to enable a greater variety of morphologies than simple AB diblock copolymers and allow wider composition windows for ordered network structures that have advantages such as 3-D connectivity and enhanced mechanical properties. In this work, the morphology space of inorganic nanocomposites was investigated comprehensively and systematically using poly(isoprene-*b*-styrene-*b*-ethylene oxide) (ISO) and aluminosilicate sol nanoparticles. Over eighty nanocomposites with different compositions were synthesized and the morphologies were characterized by a combination of small-angle X-ray scattering (SAXS) and transmission electron microscopy (TEM) measurements. The ternary morphology map of ISO and aluminisolicate sol was successfully constructed, which reveals at least eight distinct morphologies. In particular, this triblock terpolymer was able to provide wide composition windows (2-10 vol %) for ordered network morphologies, allowing these network structures to be more easily accessible experimentally. This morphology map could be used as a model to predict the structure direction of other functional inorganic materials and a highly ordered network titania composite with core-shell double gyroid structure (cs-G^D) was

demonstrated as an example.

Introduction

The self-assembly based nanostructure formation by block copolymers (BCPs) has received increasing attention due to their ability to attain the ordered mesostructures at the 2-50 nm length scale[1, 2]. Amphiphilic diblock copolymers of the form AB and triblock copolymers of the form ABA, where A and B represent chemically distinct polymer blocks have been extensively studied as structure-directing agents by co-assembly with functional inorganic materials that selectively swell a specific block of the BCP[3, 4]. The size of inorganic sol nanoparticles have to be smaller than a characteristic length, i.e. the root-mean-square end-to-end distance of the interacting polymer block for the successful nanostructure formation based on self-assembly of block copolymers [5]. This approach can result in well-ordered organic-inorganic hybrid materials including silicates[6-11], transition metal oxides [7, 12-18], non-oxide ceramics[19, 20], and metals[21, 22].

ABC triblock terpolymers are reported to dramatically increase the number of morphologies that can be achieved by the addition of a chemically distinct C block[23-28]. This variety in complexity makes morphological predictions of a given triblock terpolymer more challenging. These predictions are based on five independent parameters; the volume fractions of blocks A and B, f_A and f_B, and the products of $\chi_{AB}N$, $\chi_{BC}N$, and $\chi_{AC}N$ where χ_{ij} is the so-called Flory-Huggins interaction parameter between the blocks i and j, and N is the degree of polymerization. If χ_{AC} is greater than either χ_{AB} or χ_{BC} the system is said to be non-frustrated, resulting in morphologies that

are core-shell versions of the diblock counterparts i.e. core-shell hexagonal and core-shell double gyroid[28]. A frustrated system results if χ_{AC} is smaller than either χ_{AB} or χ_{BC}, yielding decorated morphologies that seek to increase the number of A-C interfaces[23].

On top of the morphological variety, ABC triblock terpolymers present much wider composition windows (4-14 vol %) for ordered network morphologies[28, 29] than AB diblock copolymer systems (2-6 vol %)[30], allowing these networked morphologies to be more easily accessible to the experimentalist[28]. Because of their three-dimensional (3-D) connectivity, high surface area and superior mechanical properties ordered network structures are advantageous, e.g. in many energy device applications such as fuel cells, batteries, supercapacitors and solar cells that are all electrochemical systems with reactions and transport problems[27]. For example, Crossland *et al.* reported the first successful application of a block copolymer directed ordered bicontinuous gyroid network titania film in a solid-state dye-sensitized solar cell (ssDSC) where the highly ordered pore structure is advantageous for uniform infiltration of an organic hole transporting materials[31].

Complex and ordered network materials designed using co-assembly of ABC triblock terpolymers have the potential for facile synthesis of novel device architectures. Accessibility of networked morphologies, including the alternating gyroid (G^A) and the core-shell double gyroid (CS-G^D) phases, allows for the practical application of these materials with triply continuous pathways. For example, such an architecture would provide an ideal platform for high energy and power density lithium ion batteries[32, 33] where one block acts as a positive electrode, a second

block acts as a conducting electrolyte, and the third block acts as a negative electrode. Additionally, this architecture would be well suited for nano- and ultra-filtration membranes because these morphologies do not require specific alignment to achieve a pathway from the top surface of a film to the bottom surface, typically a major challenge for copolymer derived membranes. Moreover, the periodic nature of triblock terpolymers suggest that membranes derived from these materials would have excellent molecular weight cut-offs due to highly uniform pore sizes. Gobius du Sart *et al.* demonstrated the coassembly of a poly(*tert*-butoxystyrene-*b*-styrene-*b*-4-vinylpyridine) with the small organic molecule pentadecylphenol to form a core-shell gyroid film[34]. Subsequent removal of the small molecule yielded nanochannels across the film, presenting the possibility for membrane-type applications.

Despite all these advantages, so far there are only a few reported examples of ABC triblock terpolymer derived inorganic materials[35-39] including a recent demonstration of bicontinuous and mesoporous titania films for ssDSCs[35]. In contrast, AB diblock copolymer directed inorganic hybrid systems have been extensively studied. For a particular model system, i.e. poly(isoprene-*b*-ethylene oxide) (IO) structure directing aluminosilicate sol nanoparticles, a morphology diagram was established by mapping out a substantial part of the phase space[11]. Such morphology maps are of interest as first order guides for other block copolymer-oxide nanoparticle systems and may also serve as the basis for comparison with theoretical treatments of the phase space of block copolymer-nanoparticle mixtures. In the reported IO directed aluminosilicate morphology diagram, the composition windows for ordered hybrid network morphologies are very small and not all IOs give

rise to network structures upon addition of inorganic sols.

Herein we report a comprehensive and systematic study of the morphologies of ABC triblock terpolymer–directed inorganic hybrids using poly(isoprene-*b*-styrene-*b*-ethylene oxide) (ISO) and aluminosilicate sols as a model system. Over eighty nanocomposites with different compositions were synthesized from four ISO triblock terpolymers with different compositions (f_I, f_S, f_O) and two diblock copolymers by adding increasing amounts of inorganic sol to each block copolymer. The resulting morphologies were characterized by a combination of small-angle X-ray scattering (SAXS) and transmission electron microscopy (TEM) measurements. We particularly emphasized exploration of the composition windows for ordered network morphologies that are promising for applications including energy devices. Removal of the organic phase by plasma etching produced freestanding nanostructured aluminosilicate materials. Finally, using titania sols as an example, we show that the results of this ABC triblock terpolymer based hybrid morphology map provide a useful guide for the morphology search of hybrids from other oxides.

Experimental Section

Triblock Terpolymer Synthesis

The poly(isoprene-*b*-styrene-*b*-ethylene oxide) (ISO) was synthesized by sequential anionic polymerization similar to a previous report[23]. Briefly, benzene was distilled over *n*-butyllithium into a reactor under static vacuum ($\leq 10^{-2}$ mbar). *Sec*-butyl-lithium was then added as the initiator. Isoprene was distilled after stirring over n-butyl-lithium and added to a reactor and allowed to polymerize for 12 hours. Styrene was

then distilled over CaH_2 and subsequently added to the reactor. After an additional 12 hours the polymer was end-capped with a terminal hydroxyl group using ethylene oxide and subsequently dried and redissolved in chloroform, then washed 3 times with water. The polymer was dried again and redissolved in THF before being reinitiated with potassium naphthalide. Finally, ethylene oxide was distilled over n-butyl-lithium and added to the reactor before terminating with methanolic HCl. The different terpolymers had a total molar mass between 23 and 45 kg/mol and the PEO content was controlled between 11 and 17 vol %. Besides terpolymers, poly(isoprene-*b*-ethylene oxide) (IO) and poly(styrene-*b*-ethylene oxide) (SO) diblock copolymers were synthesized with similar molar mass (~35 kg/mol) and PEO content (13/14%). Characterization results for all polymers are shown in Table 5.1 displaying polydispersity indices of less than 1.07. The component volume fractions were calculated using the density of homopolymers at 140 °C[40].

Sample Preparation

Bulk film samples were prepared by dissolving the polymer in tetrahydrofuran (THF) or a mixture of 1:1 THF:chloroform by volume. A predetermined quantity of aluminosilicate sol was added to the polymer solution and stirred briefly before transfer to a covered polytetrafluoroethylene dish at 50°C. The aluminosilicate sol was prepared using a two-step acid catalyzed hydrolysis of 3-(glycidyloxypropyl) trimethoxysilane and aluminum sec-butoxide as previously described[8, 9]. The films were subsequently heated to 130°C for 1 hour to further crosslink and densify the aluminosilicate component. For the ISO-titania hybrid material, the polymer was in 8

ml of THF with stirring for about 1 hour. A titanium-containing sol was prepared separately by the addition of 0.4 ml titanium(IV) isopropoxide to 0.129 ml hydrochloric acid (37%) under vigorous stirring followed by addition of 2 ml THF after 5 min stirring. After another 5 min, the predetermined amount of sol was added to the polymer solution and subsequently stirred for an hour. Then the films were cast and annealed as described before.

Transmission Electron Microscopy (TEM)

All bulk films were cut into thin slices of ~50-70 nm thickness at -60 °C using a Leica Ultracut UCT microtome and floated on the surface of a solution of water and dimethysiloxane (4:6 by volume). The slices were collected onto 400 mesh copper TEM grids and stained using sublimed osmium tetroxide vapor for 1 hour. A Fischione model 1020 Ar-O plasma cleaner was used for 3 minutes on nanocomposite slices to remove the polymer. All slices were imaged using a Technai T12 transmission electron microscope operating at 120 kV.

Small Angle X-Ray Scattering (SAXS)

SAXS data on nanocomposite samples and most neat polymer films were collected at the Cornell High Energy Synchrotron Source (CHESS) with a multilayer monochromater (λ=1.547 Å) with a 2D area detector and a sample-to-detector distance of 1.61 m. SAXS data for the ISO3 neat polymer film was collected using a Rigaku RU300 with a copper rotating anode (λ=1.54 Å) operated at 40 kV and 50 mA. SAXS data is presented as 1D plots of radially integrated intensity versus the

scattering vector q, where $q=\frac{4\pi\sin\theta}{\lambda}$ and 2θ is the total scattering angle.

Results and Discussion

The morphology space of poly(isoprene-*b*-styrene-*b*-ethylene oxide) (ISO) triblock terpolymer directed inorganic hybrids was investigated by the addition of inorganic aluminosilicate sol nanoparticles that are known to selectively swell the O block[8, 9]. For the preparation method used here the size of aluminosilicate sol nanoparticles was previously reported as less than 2 nm with average size of 1 nm[5]. The root-mean-square end-to-end distance of the PEO block is greater than 6 nm for all block copolymers studied here as shown in Table 5.1, thereby matching the size requirement for successful BCP self-assembly directed inorganic nanostructure formation[5]. Over eighty nanocomposite samples were prepared from the block copolymers using THF as a solvent for which the O + oxide volume fractions were varied from 11-75 vol % (see Table 5.2). For each sample the resulting hybrid morphology was characterized by a combination of SAXS and TEM measurements. The strategy for mapping out the morphology space of these hybrids, which is a quasi ternary morphology space for components I, S and O+oxide, was to synthesize ISO triblock terpolymers with increasing relative PS to PI volume fractions (0.16/0.73 for ISO1; 0.36/0.49 for ISO2; 0.52/0.31 for ISO3; and 0.74/0.15 for ISO4, see Table 5.1) covering, in roughly equal intervals, the I/S composition space. At the same time these terpolymers were chosen to have low and comparable PEO volume fractions (here 11-17 vol%) which could subsequently be increased by adding increasing amounts of aluminosilicate sol

nanoparticles to each triblock terpolymer thereby covering, for each terpolymer, the composition window towards the O+oxide vertex of the ternary morphology map (see Figure 5.3 below). In addition to the four ISO terpolymers, IO and SO diblock copolymers with similarly low PEO volume fractions (14 and 13 vol.% for IO1 and SO1, respectively, see Table 5.1) were synthesized in order to cover the IO (left) and SO (right) composition edges of the ternary composition map (see Figure 5.3 below).

Figure 5.1 presents the morphology characterization of the neat block copolymer film and selected nanocomposites from ISO3 (f_I = 0.31, f_S = 0.52, f_O = 0.17). The structure directing neat ISO3 terpolymer was first characterized before the addition of any inorganic material to determine the baseline morphology. Figure 5.1a shows the radially integrated 1D SAXS pattern of the unstained neat polymer film. Dashed lines corresponding to $(q/q^*)^2$ = 2, 6, 8, 10, 12, 14, 16, 18 etc. as expected for an alternating gyroid (G^A) lattice are marked in this pattern. and are consistent with the observed peak positions. The appearance of a weak peak at $(q/q^*)^2 = 4$ is attributed to structural heterogeneity in the pure polymer film as was already observed and discussed in a previous study[37]. Figure 5.1b shows a TEM image of the terpolymer sample stained with osmium tetroxide and displaying 3-fold symmetry. The osmium tetroxide selectively stains the I block, causing it to appear dark in the bright field TEM image, while the S and O blocks appear lighter. The inset in Figure 5.1b displays a simulated TEM projection of the (111) plane of a polymer thin film containing the same volume fractions and is darkened to mimic the staining contrast in the polymer sample. The similarities between the TEM and simulated images in addition to the SAXS pattern analysis for this material are suggestive of a G^A structure. A simulated

unit cell of the G^A structure is shown in Figure 5.1c with the I block in red, the S block in green, and the O block in blue. From this simulation, I and O blocks form minority gyroid struts of opposite chirality embedded in a (majority) matrix of S, resulting in a triply continuous, periodic structure.

Incorporating inorganic aluminosilicate sol nanoparticles into a specific block of the terpolymer is achieved by the selective hydrophilic interaction of the sol nanoparticles with the O block. Swelling of this block changes the relative volumes of each component in the system. Mixing in of increasing amounts of aluminosilicate sol resulted in five distinct nanocomposite morphologies from ISO3 as shown in Figure 5.1d-p. Low aluminosilicate loadings where the O + oxide comprised 21 and 27 vol % of the film resulted in a networked morphology. The radially integrated, 1D SAXS pattern for the hybrid with 27 vol % sol loading, shown in Figure 5.1d, exhibits broad peaks that cannot be unambiguously assigned to a lattice. For comparison the SAXS pattern has vertical dashed lines indicating the expected peak positions for a G^A lattice. When characterized by TEM, at the local level the OsO_4 stained sample displays a periodic mesostructure (Figure 5.1e) while the corresponding plasma cleaned sample reveals a periodic, continuous network of aluminosilicate struts (Figure 5.2f). Here the aluminosilicate sol selectively swells the O domains into struts, resulting in a self-supported, continuous, inorganic framework after removal of the polymer by plasma treatment. Other than being a networked morphology, the structure cannot be definitively assigned to a lattice such as G^A ($I4_132$) or equilateral O^{70} (*Fddd*) reported for similar composites previously [37].

Aluminosilicate loadings resulting in O + oxide volumes of 33 and 39 vol % all

formed a three phase lamellar structure. Figure 5.3g shows the SAXS pattern for the 33 vol % sample with markings at $(q/q^*)^2$ = 1, 4, and 9 for a 1-dimensional lamellar lattice. The observed peaks clearly index well with these markings. Figure 5.3h shows a TEM image of the same sample stained with OsO_4 where the darkest stripes correspond to the stained I block, the grey areas correspond to the O+oxide domains, while the white stripes correspond to the S block. The lamellar structure does not sustain itself after the polymer is etched out by oxygen plasma as shown in Figure 5.1i.

The second tricontinuous network structure in the hybrid composition space explored for ISO1 terpolymer occurred when the O + oxide domains made up 50 and 55 vol % of the film. Figure 5.4j shows the SAXS pattern for the 50 vol % sample with markings at peak positions of $(q/q^*)^2$ = 6, 8, 14, 16, 20 etc. as expected for the core-shell G^D lattice. The experimental peaks are clearly consistent with these markings. A forbidden peak is seen at $(q/q^*)^2$ = 2, however, and we attribute the appearance of this peak to uniaxial compression along the z-axis of the film occurring upon drying as previously reported for SAXS patterns of cubic, continuous structures[31, 41]. The specific compression for the present film along the z-axis was determined by measuring SAXS patterns both parallel and perpendicular to the film normal and determined to be 15.5 %. Figure 5.1k shows a TEM image of the same sample stained with OsO_4 exhibiting the typical "wagon-wheel" projection along the (111) plane, which is consistent with the simulated TEM image for this projection (see inset). Plasma cleaning leaves dark aluminosilicate domains behind that form an ordered network structure (Figure 5.1l).

Further increasing the amount of aluminosilicate sol added to ISO3 to 60-65

vol % yielded an O+oxide composition resulting in an inverse hexagonal morphology. Figure 5.1m shows the experimental SAXS pattern for the sample with O+oxide of 60 vol %. The pattern also exhibits dashed vertical lines for the expected peak positions of a hexagonal lattice with $(q/q^*)^2$ = 1, 3, 4, 7, 9, 12, 13 and 16. The observed peaks correspond well to the expected reflections. TEM images of the stained sample, shown in Figure 5.1n, corroborate assignment to an inverse hexagonal structure with the I block composing the core, the S block composing the shell, and the O + oxide domains forming the majority matrix. Figure 5.1o shows a TEM image of the same sample after plasma cleaning, more clearly revealing the contrast of the O+oxide inverse hexagonal matrix. Finally, an inverse micellar morphology appears when the O+oxide composition is further increased to 73 vol %. Observed reflexes in the experimental SAXS patterns are not sharp enough to be indexed unambiguously to a BCC lattice (see dashed vertical lines in Figure 5.1p) but the corresponding bright field TEM images of the stained and plasma cleaned sample clearly indicate a micellar structure (Figure 5.1q and r).

Neat terpolymer ISO2 (f_I = 0.49, f_S = 0.36, f_O = 0.15) exhibited a lamellar structure as revealed by SAXS measurements (Figure S2 in supplementary information) consistent with previously reported data [28]. Characterization results for aluminosilicate composites with two very different O+oxide compositions of 22 vol % (ISO2-2) and 50 vol % (ISO2-8) are presented in Figure 5.2. These two compositions fall into ranges for which networked morphologies were identified in case of ISO1, *vide supra*. The experimental SAXS patterns for both hybrids are shown in Figure 5.2a and c. For comparison, dashed vertical lines indicate expected peak positions for

double gyroid (G^D, Q230) lattices. In both cases experimental and expected peak positions are in good agreement. Peaks at $(q/q^*)^2 = 2, 4$ are again attributed to a uniaxial compression of the hybrids during film formations, *vide supra*. Simulated core-shell G^D unit cells are illustrated for both composites in the right upper corner of the SAXS patterns, see Figure 5.2a and c, where the I block is shown in red, the S block in green, and the O+oxide block in blue. For the lower O+oxide volume fraction (22 vol %) the O+oxide component turns into the core strut domains with a S shell embedded in an I matrix, see the simulated unit cell in Figure 5.2a. For the composite with O+oxide volume fraction of 50 vol % the morphology is inverted and the O+oxide domains now make up the majority matrix component of the hybrid material with I in the minority core strut domains surrounded by S shells, see the simulated unit cell in Figure 5.2c. At the same time the unit cell size (d_{100}) increases from 82.4 nm to 88.7 nm due to higher loading with oxide. It is noticeable that the grain size of the double gyroid structures is quite large, up to several micrometers for both minority and majority O+oxide composites, as can be inferred from the bright field TEM images of Figure 5.2b and d. In case of the minority O+oxide composite the 6-fold symmetry of the projection in the inset is highlighted in yellow (Figure 5.2b).

Characterization results for aluminosilicate nanocomposite materials directed from all four ISO terpolymers along with those directed from SO1 and IO1 copolymers are summarized in Table 5.2. The compositions of each of the nanocomposites are based on volume fractions but the table also shows the weight fractions of the aluminosilicate sol used to prepare each hybrid. Composite morphologies of ISO-aluminosilicate hybrids identified in this study include the

sphere (Sph), the hexagonal cylinder (Hex), the alternating gyroid (G^A), the core-shell double gyroid (CS-G^D), the lamellar (Lam), the inverse core-shell double gyroid (iCS-G^D), the inverse hexagonal cylinder (iHex), and the inverse micellar structure, i.e. eight different morphologies. The resulting ternary morphology diagram of ISO triblock terpolymer directed aluminosilicate hybrids based on volume fractions is presented in Figure 5.3. This comprehensive morphology map covers a large fraction of the composition space of the I-S-O+oxide ternary system. Individual terpolymers show up to six different well-defined morphologies upon addition of the aluminosilicate sol. This feature nicely demonstrates the versatility of the approach as accessing up to six different morphologies by adding varying amounts of sol to the same terpolymer is much easier as compared to synthesizing six different terpolymers in order to cover the same morphology space.

Depending on the I and S compositions, the ISO-aluminosilicate hybrid system provides wide O+oxide composition windows of 2.3-10 vol % for ordered network morphologies such as CS-G^D and G^A. Blue lines in the morphology map of Figure 5.3 tentatively indicate regions in phase space of such network structures. The sequence of composites directed from all four ISO triblock terpolymers show both minority and majority O+oxide based network structures. For example, ISO3 ($f_I < f_S$) shows the windows of ~10 vol % in the minority and ~5 vol % in the majority inorganic regions, although the network morphology in the minority region is not definitively identified at the moment. Similarly, the windows are ~6 vol % in the minority and ~2 vol % in the majority regions from ISO2 ($f_I > f_S$), and ISO4 ($f_I << f_S$) shows ~5 vol % window in the majority. The network structure was also observed from one sample each in the

minority region from ISO4 and both in the minority and majority regions from ISO1 ($f_I >> f_S$). In contrast to the terpolymers, only one of the sequences of composite morphologies directed from the two diblock copolymers IO1 and SO1 shows a network morphology (see Figure 5.3). This is in the SO directed sequence where for a specific composition an inverse double gyroid structure is observed, i.e. a structure in which the O+oxide domains constitute the majority phase in the hybrid. For the hybrids directed by IO1 no networked phase was found. At first sight this seems to be in contradiction to a previously published study of the morphology diagram of IO diblock copolymer directed aluminosilicate hybrids in which both, minority and majority O+oxide based network structures were identified[11]. Closer inspection of the data in that study reveals, however, that the composition windows for these network structures were quite small and that the molecular weights and/or IO compositions of the IO copolymers leading to these networks were quite different to the present study. We thus speculate that in the present study we either did not sample composition space of the IO1/aluminosilicate composites careful enough or that the molecular weight or composition of IO1 was not appropriate to identify network structures. In any case, the results on the diblock copolymer based composites emphasize the importance of moving to ABC triblock terpolymers in order to conveniently access networked morphologies.

The sequence of morphologies of composites along each isopleths, i.e. composites obtained by adding varying amounts of aluminosilicate sol to the same terpolymer, is the same as expected from the phase diagram of ISO terpolymer itself (disregarding biphasic regions with mixed morphologies)[25, 28]. This finding

suggests that consistent with previous results on IO diblock copolymer directed aluminosilicates, the resulting terpolymer directed hybrid materials, if not constituting equilibrium structures, are at least exhibiting very close to equilibrium type structures. As expected for multicomponent systems, biphasic mixed morphologies could clearly be identified for some regions of phase space. As an example Figure 5.4 shows the SAXS patterns and the corresponding bright field TEM images for hybrid samples ISO2-7 and ISO1-9. While observed peak positions in the SAXS patterns are consistent with a hexagonal lattice, TEM images of the same materials clearly indicate a mixed morphology consisting of regions with inverse hexagonal structure and regions with lamellar structure. Although SAXS patterns often suggest pure phases (see comparison of SAXS data for composites ISO1-9, ISO2-7, ISO3-5, and ISO4-8 in the Supporting Information) it is therefore difficult to entirely exclude the existence of minority regions in the sample with structures of adjacent phases in the morphology map. While for simplicity the morphology diagram in Figure 5.3 only depicts one such biphasic region in phase space between the lamellar and inverse gyroidal phases, such biphasic regions exist between all adjacent phases.

To the best of our knowledge this work constitutes the first comprehensive study of the morphology space of self-assembled organic-inorganic hybrids structure directed by ABC triblock terpolymers. Such studies could be used, e.g. as the basis for comparison with theoretical predictions of block copolymer-nanoparticle phase behavior [42]. The morphology map of Figure 5.3 for the system ISO and aluminosilicate sol nanoparticles could further be used as a first-order guide to help predict the structure of other functional inorganic hybrid materials such as transition

metal oxide sols structure directed by ISO triblock terpolymers. For example, titanium dioxide (titania) is a particularly interesting transition metal oxide that has been applied in many areas such as photovoltaics, photocatalysis, membranes, optics and so forth. In order to demonstrate the usefulness of the morphology map in Figure 5.3 as a guide for other hybrids we prepared titania composites according to a protocol described in the experimental section. The characterization results of a particular composite with highly ordered core-shell double gyroid morphology structure directed from terpolymer ISO2 are summarized in Figure 5.5. The O+oxide composition (24.6 vol %) of the composite is within the window for the minority network from ISO2 on the morphology map as shown in Table 5.3. The SAXS pattern in Figure 5.5b is indexed with Q230 symmetry and the bright field TEM images show a highly ordered network structure with grain sizes of approximately several hundred nanometers, see Figure 5.5a. Figure 5.5c and d show 4-fold and 3-fold symmetry projections, respectively, that are characteristic for a structure with cubic symmetry. In fact the 3-fold symmetry projection shows the wagon-wheel pattern, typical for materials with double gyroid morphology.

Conclusions

We have explored the morphology space of ABC triblock terpolymer poly(isoprene-*b*-styrene-*b*-ethylene oxide) structure directing an inorganic aluminosilicate sol that selectively swells the O block. A ternary morphology diagram was successfully constructed from over eighty nanocomposites that shows at least eight distinct hybrid morphologies. Adding increasing amounts of inorganic sol to the same terpolymer

provides, in several cases, access to six different composite morphologies. The accessibility of multiple nanostructured materials from the same terpolymer makes this approach very attractive as it prevents time-consuming synthesis of multiple triblock terpolymers to access the same phase space. In particular, the ISO-aluminosilicate system provides wide composition windows for ordered network morphologies such as alternating gyroid (G^A) and core-shell double gyroid (G^D). As demonstrated through a titania composite with network morphology, the morphology map could be used as a first-order guide to predict the structure direction of other functional inorganic hybrid materials. It may also serve as a basis for comparison with theoretical predictions of the phase space of triblock terpolymer directed composite materials.

Table 5.1. Synthesis and characterization results of PI-*b*-PS-*b*-PEO (ISO), PS-*b*-PEO (SO) and PI-*b*-PEO (IO) block copolymers

	ISO1	**ISO2**	**ISO3**	**ISO4**	**SO1**	**IO1**
Overall M_n, g/mol	38,332	43,321	23,180	45,409	37,230	33,566
PI, g/mol	26,236	19,393	6,282	5,808	-	27,893
PS, g/mol	6,900	16,637	12,401	33,898	32,000	-
PEO, g/mol	5,196	7,291	4,497	5,703	5,230	5,673
Volume fraction[a]						
PI	0.73	0.49	0.31	0.15	-	0.86
PS	0.16	0.36	0.52	0.74	0.87	-
PEO	0.11	0.15	0.17	0.11	0.13	0.14
PDI	1.07	1.07	1.05	1.07	1.03	1.09
R_o of PEO, nm[b]	6.46	7.65	6.01	6.77	6.48	6.75

[a] Volume fraction was calculated based on the previously reported density of each block, i.e. $\rho_{PI} = 0.830$, $\rho_{PS} = 0.969$ and $\rho_{PEO} = 1.064$ cm^3/g. [40]
[b] R_o was calculated based on the equation, $R_0 = 0.595\sqrt{}N$.[40]

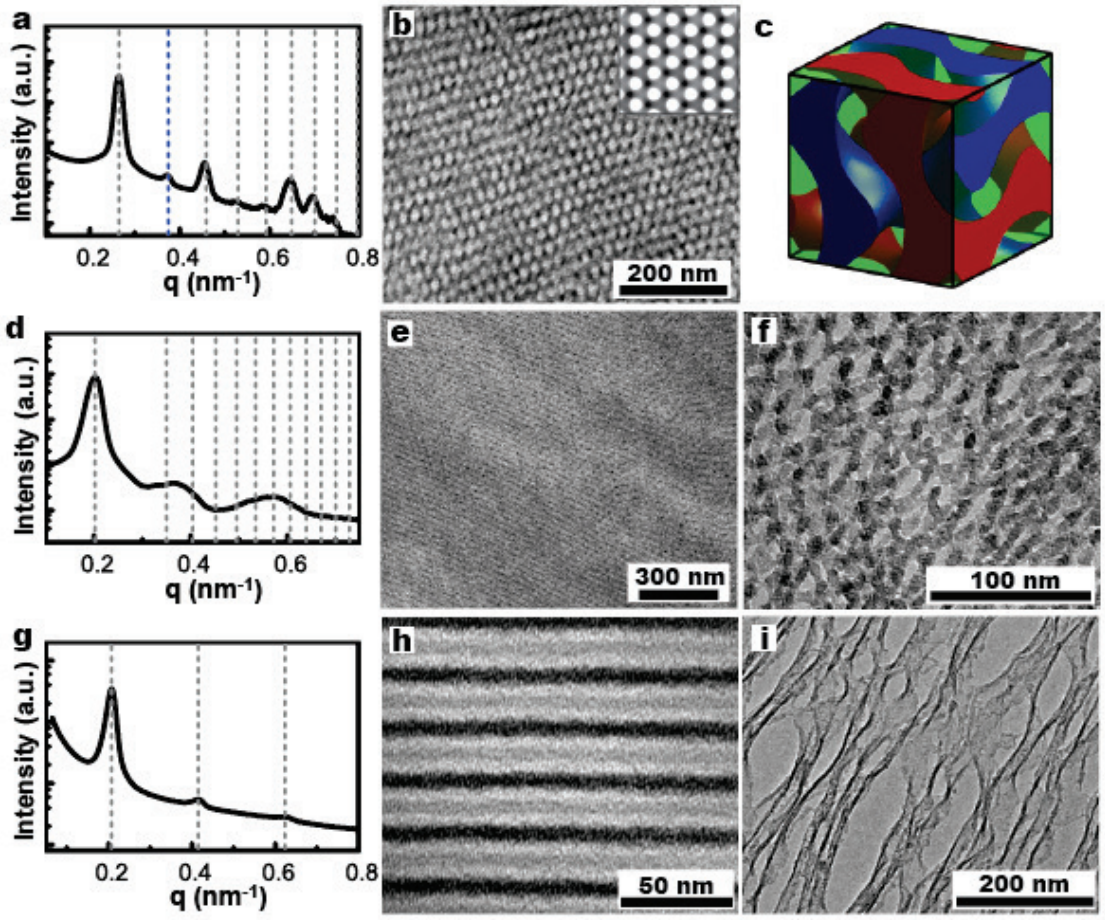

Figure 5.1. Representative SAXS patterns and corresponding bright field TEM images of ISO3 neat polymer film (a,b) and ISO3-aluminisilicate nanocomposites from low to high inorganic loadings: ISO3-2 (d,e,f), ISO3-3 (g,h,i), ISO3-6 (j,k,l), ISO3-8 (m,n,o) and ISO3-10 (p,q,r). Samples in the middle column were stained with OsO4 to enable contrast between the I block (dark), S block (white) and O+Oxide domain (grey) (a,e,h,k,n,q) and samples on the right were oxygen plasma treated to leave aluminosilicate structures by removal of ISO polymer (f,i,l,o,r). The morphologies identified from radially integrated 1D SAXS patterns (a,d,g,j,m,p) are consistent with the respective TEM images. The inset in (b) shows a simulated TEM projection for a G^A (111) plane and a simulated unit cell in (c) represents the G^A structure of ISO neat polymer with the I, S, and O domains in red, green, and blue, respectively.

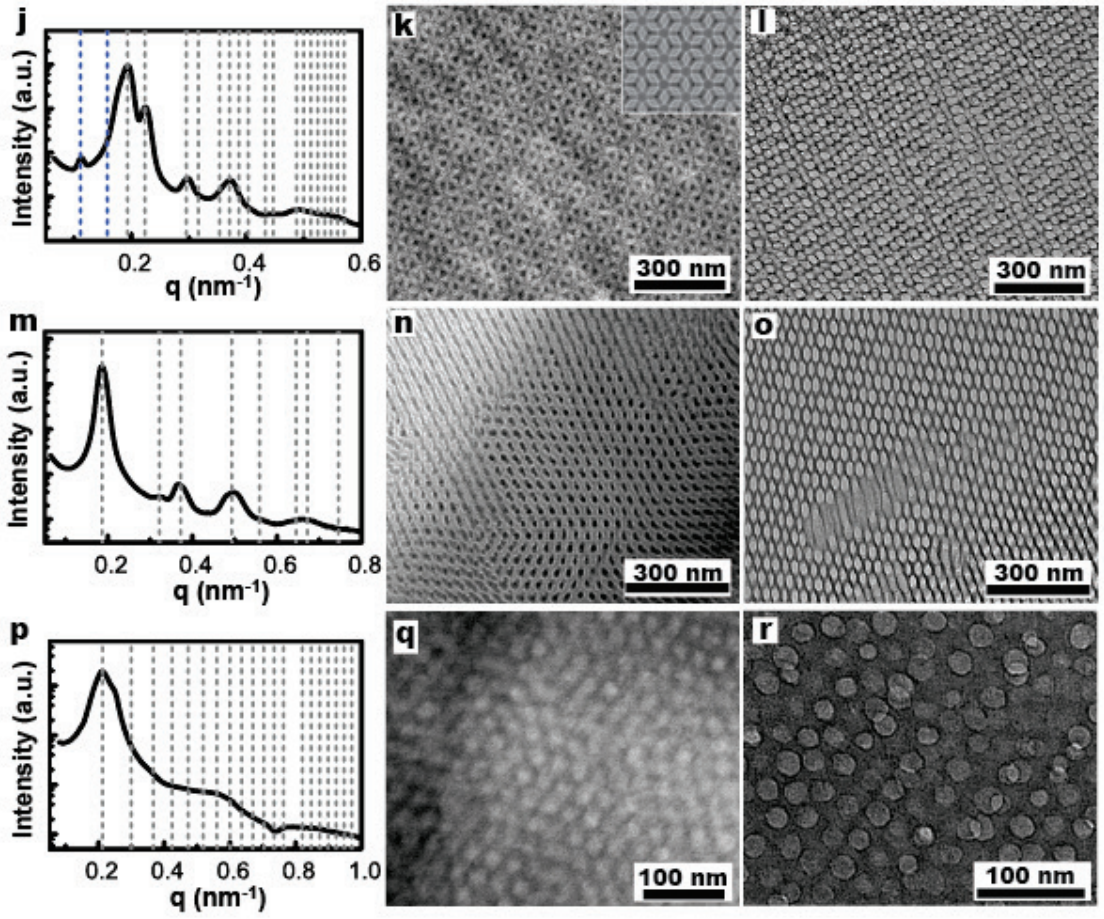

Figure 5.1. (continued)

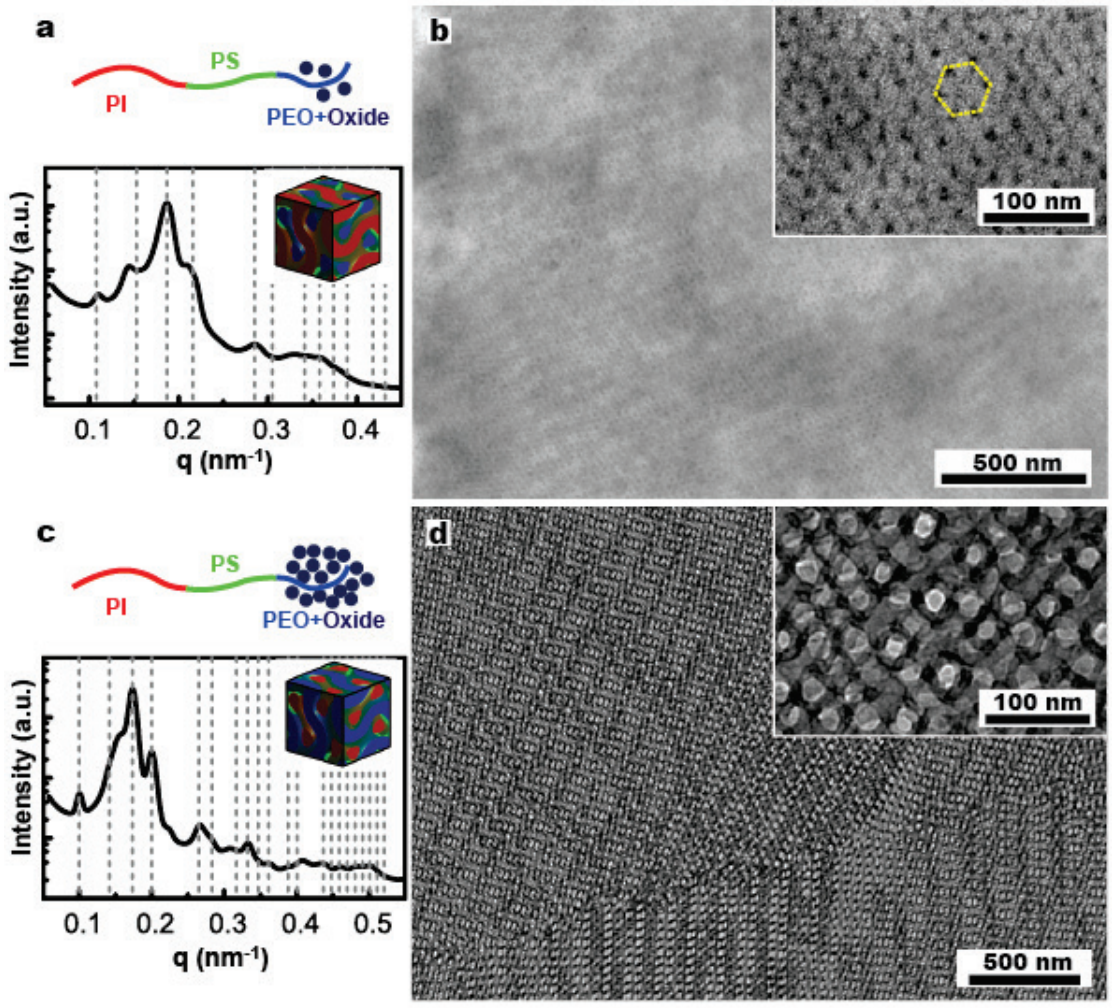

Figure 5.2. Representative SAXS patterns and corresponding bright field TEM images for CS-G^D structures with minority (ISO2-2: a,b) and majority (ISO2-8: c,d) aluminosilicate domains derived from polymer ISO2. In the composite with minority aluminosilicate domains the struts consist of O+oxide (blue), while the I (red) and S (green) blocks form matrix and shell domains, respectively. For the larger amount of oxide the gyroid structure is inverted and the O+oxide domains now become the matrix, compare the model unit cells in (a) and (c). At the same time the unit cell size (d_{100}) increases from 82.4 nm (a) to 88.7 nm (c) due to a greater degree of swelling. The dark domains in the TEM images correspond to domains of O+oxide. For both composites as revealed by TEM (b,d) the grain size expands up to several micrometers. In case of the composite with minority aluminosilicate domains for clarity the 6-fold symmetry projection is highlighted in the inset (b).

Table 5.2. Composition, suggested morphologies, and measured d-spacings of ISO/IO/SO + aluminosilicate nanocomposites

	volume fraction[a]			weight fraction		d-spacing
	I	S	O+Oxide	of oxide	morphology	(nm)[b]
ISO1	0.725	0.163	0.112	0.000	Hexagonal	29.0
ISO1-1	0.665	0.150	0.185	0.132	Hexagonal	31.7
ISO1-2	0.616	0.139	0.245	0.231	Hexagonal	33.2
ISO1-3	0.591	0.133	0.276	0.278	Q230	85.4
ISO1-4	0.568	0.128	0.305	0.321	Lamellar	38.8
ISO1-5	0.538	0.121	0.341	0.373	Lamellar	34.1
ISO1-6	0.517	0.116	0.366	0.407	Lamellar	40.0
ISO1-7	0.476	0.107	0.417	0.471	Lamellar	36.4
ISO1-8	0.461	0.104	0.435	0.494	Lamellar	36.8
ISO1-9	0.413	0.093	0.494	0.563	Hex+Lam	
ISO1-10	0.378	0.085	0.537	0.610	Inv Q230	96.7
ISO1-11	0.342	0.077	0.581	0.656	Inv hexagonal	43.5
ISO1-12	0.300	0.068	0.632	0.707	Inv hexagonal	39.7
ISO1-13	0.250	0.056	0.693	0.764	Inv micellar	50.2
ISO1-14	0.222	0.050	0.728	0.795	Inv micellar	51.4
ISO2	0.493	0.362	0.145	0.000	Lamellar	32.8
ISO2-1	0.463	0.340	0.197	0.097	Q230	78.9
ISO2-2	0.452	0.332	0.215	0.129	Q230	82.4
ISO2-3	0.430	0.316	0.254	0.194	Q230	91.0
ISO2-4	0.416	0.306	0.278	0.233	Lamellar	36.0
ISO2-5	0.378	0.278	0.344	0.333	Lamellar	38.8
ISO2-6	0.345	0.253	0.402	0.414	Lamellar	38.5
ISO2-7	0.320	0.235	0.445	0.471	Hex+Lam	
ISO2-8	0.287	0.211	0.502	0.540	Inv Q230	88.7
ISO2-9	0.274	0.202	0.524	0.567	Inv Q230	93.5
ISO2-10	0.246	0.180	0.574	0.623	Inv hexagonal	42.5
ISO2-11	0.221	0.163	0.616	0.668	Inv hexagonal	39.4
ISO2-12	0.198	0.145	0.657	0.710	Inv hexagonal	41.5
ISO2-13	0.168	0.124	0.708	0.760	Inv micellar	46.9
ISO3	0.308	0.520	0.172	0.000	Q214	33.5
ISO3-1	0.292	0.495	0.213	0.077	Network(Q214)	41.8
ISO3-2	0.272	0.460	0.269	0.174	Network(Q214)	44.0
ISO3-3	0.248	0.420	0.332	0.277	Lamellar	30.2
ISO3-4	0.226	0.383	0.391	0.364	Lamellar	31.6
ISO3-5	0.202	0.342	0.456	0.454	Hex+Lam	
ISO3-6	0.187	0.316	0.498	0.508	Inv Q230	79.5
ISO3-7	0.168	0.285	0.547	0.569	Inv Q230	82.1
ISO3-8	0.147	0.249	0.604	0.635	Inv hexagonal	33.7
ISO3-9	0.129	0.218	0.654	0.689	Inv hexagonal	32.0
ISO3-10	0.100	0.170	0.730	0.767	Inv micellar	41.9
ISO4	0.148	0.739	0.113	0.000	Spherical	28.5
ISO4-1	0.134	0.672	0.194	0.135	Hexagonal	26.9
ISO4-2	0.124	0.619	0.257	0.233	Unidentified	
ISO4-3	0.116	0.582	0.301	0.297	Q230	82.3

ISO4-4	0.112	0.559	0.329	0.334	Lamellar	33.3
ISO4-5	0.105	0.527	0.368	0.386	Lamellar	34.0
ISO4-6	0.103	0.513	0.384	0.407	Lamellar	33.8
ISO4-7	0.094	0.468	0.438	0.475	Lamellar	34.8
ISO4-8	0.088	0.441	0.471	0.514	Hex+Lam	
ISO4-9	0.081	0.403	0.516	0.566	Inv Q230	79.8
ISO4-10	0.072	0.361	0.567	0.621	Inv Q230	85.3
ISO4-11	0.065	0.324	0.611	0.667	Inv hexagonal	36.2
ISO4-12	0.057	0.287	0.656	0.712	Inv hexagonal	37.0
ISO4-13	0.048	0.241	0.710	0.763	Inv micellar	46.0
ISO4-14	0.042	0.208	0.750	0.799	Inv micellar	55.5
SO1	0.000	0.870	0.130	0.000	Unidentified	
SO1-1	0.000	0.802	0.198	0.115	Spherical	34.3
SO1-2	0.000	0.741	0.259	0.211	Hexagonal	26.3
SO1-3	0.000	0.696	0.304	0.277	Hexagonal	28.6
SO1-4	0.000	0.647	0.353	0.346	Unidentified	
SO1-5	0.000	0.614	0.386	0.390	Lamellar	31.6
SO1-6	0.000	0.564	0.436	0.453	Lamellar	31.6
SO1-7	0.000	0.513	0.487	0.515	Lamellar	32.4
SO1-8	0.000	0.467	0.533	0.570	Hex+Lam	
SO1-9	0.000	0.413	0.587	0.629	Inv Q230	77.0
SO1-10	0.000	0.365	0.635	0.679	Unidentified	
SO1-11	0.000	0.320	0.680	0.725	Inv hexagonal	32.2
SO1-12	0.000	0.274	0.726	0.769	Inv micellar	44.9
SO1-13	0.000	0.229	0.771	0.810	Inv micellar	44.4
IO1	0.863	0.000	0.137	0.000	Spherical	34.9
IO1-1	0.802	0.000	0.198	0.118	Hexagonal	34.9
IO1-2	0.748	0.000	0.252	0.211	Hexagonal	37.5
IO1-3	0.705	0.000	0.295	0.281	Hexagonal	39.8
IO1-4	0.633	0.000	0.367	0.388	Lamellar	45.9
IO1-5	0.580	0.000	0.420	0.459	Lamellar	46.5
IO1-6	0.493	0.000	0.507	0.566	Hex+Lam	
IO1-7	0.437	0.000	0.563	0.629	Inv hexagonal	46.2
IO1-8	0.387	0.000	0.613	0.681	Inv hexagonal	46.0
IO1-9	0.296	0.000	0.704	0.769	Inv micellar	52.1
IO1-10	0.253	0.000	0.747	0.807	Inv micellar	52.3

[a]Volume fraction was calculated based on the previously reported density of silicate sol (1.5 g/cm^3) [7].

[b]Lattice dimensions, d, calculated as $d=2\pi/q^*$ are based on lamellar (10), hexagonal (100), Q230 (001), Q214 (001) and spherical BCC (001) planes.

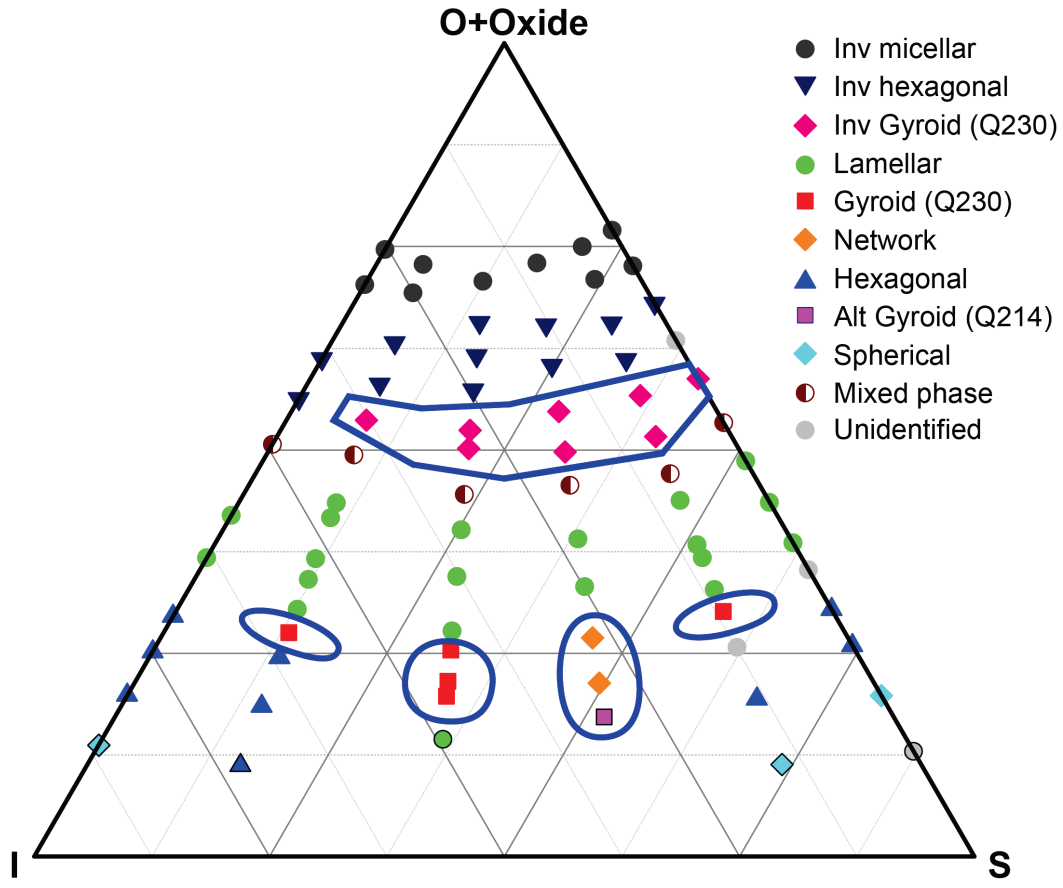

Figure 5.3. Morphology diagram for poly(isoprene-*b*-styrene-*b*-ethylene oxide) directed aluminosilicate sol nanoparticle hybrids based on volume fractions. As indicated by the different symbols, eight distinct morphologies along with mixed morphologies were identified based on a combination of SAXS and TEM data. The lowest point in each line of data symbolizes the mophology of the neat block copolymer. Regions of ordered network morphologies are highlighted by enclosed blue lines. Both, minority and majority (O + oxide) network morphologies were observed for all ISO triblock terpolymer directed hybrids. The composition windows of O+oxide for these network morphologies are about 2-13 vol%, depending on the specific I/S composition. For the diblock copolymers SO1 and IO1, only a majority network morphology was identified for SO1 based hybrids while in this study none were identified for IO diblock copolymer based hybrids. Please note that while only one region of biphasic behavior is indicated, such biphasic regions should exist between all adjacent phases.

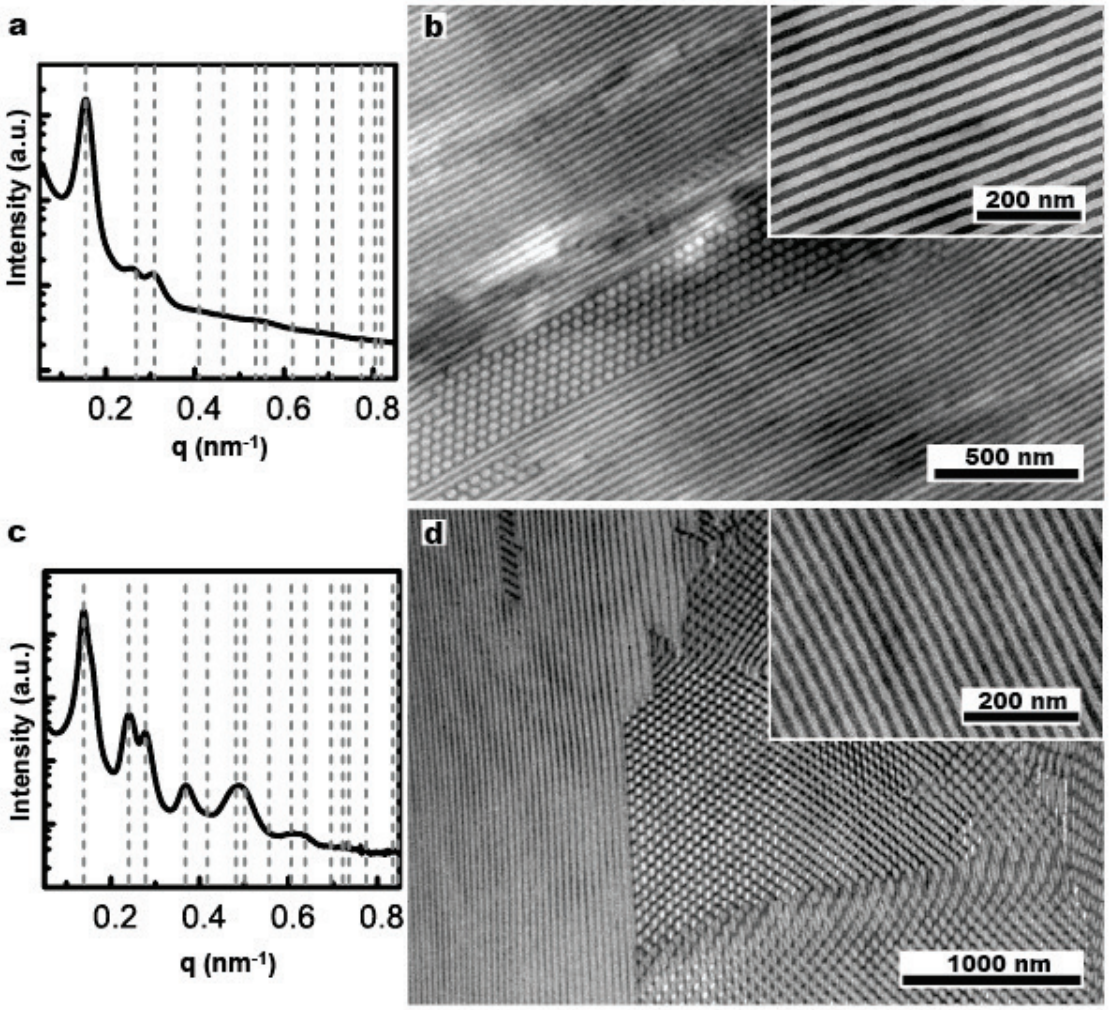

Figure 5.4. SAXS patterns and corresponding bright field TEM images for ISO2-7 (a,b) and ISO1-9 (c,d) composites. The SAXS patterns were both indexed with hexagonal symmetry ($q/q^* = 1, \sqrt{3}, \sqrt{4}, \sqrt{7}, \sqrt{9}, \sqrt{12}, \sqrt{13}, \sqrt{16}, \sqrt{19}$ etc.). A hexagonal phase is not predicted between lamellar and inverse double gyroid (Q230) phases from theoretical and experimental ISO phase diagrams [25, 28]. Indeed, TEM measurements of these samples suggest mixed morphologies of hexagonal and lamellar structures.

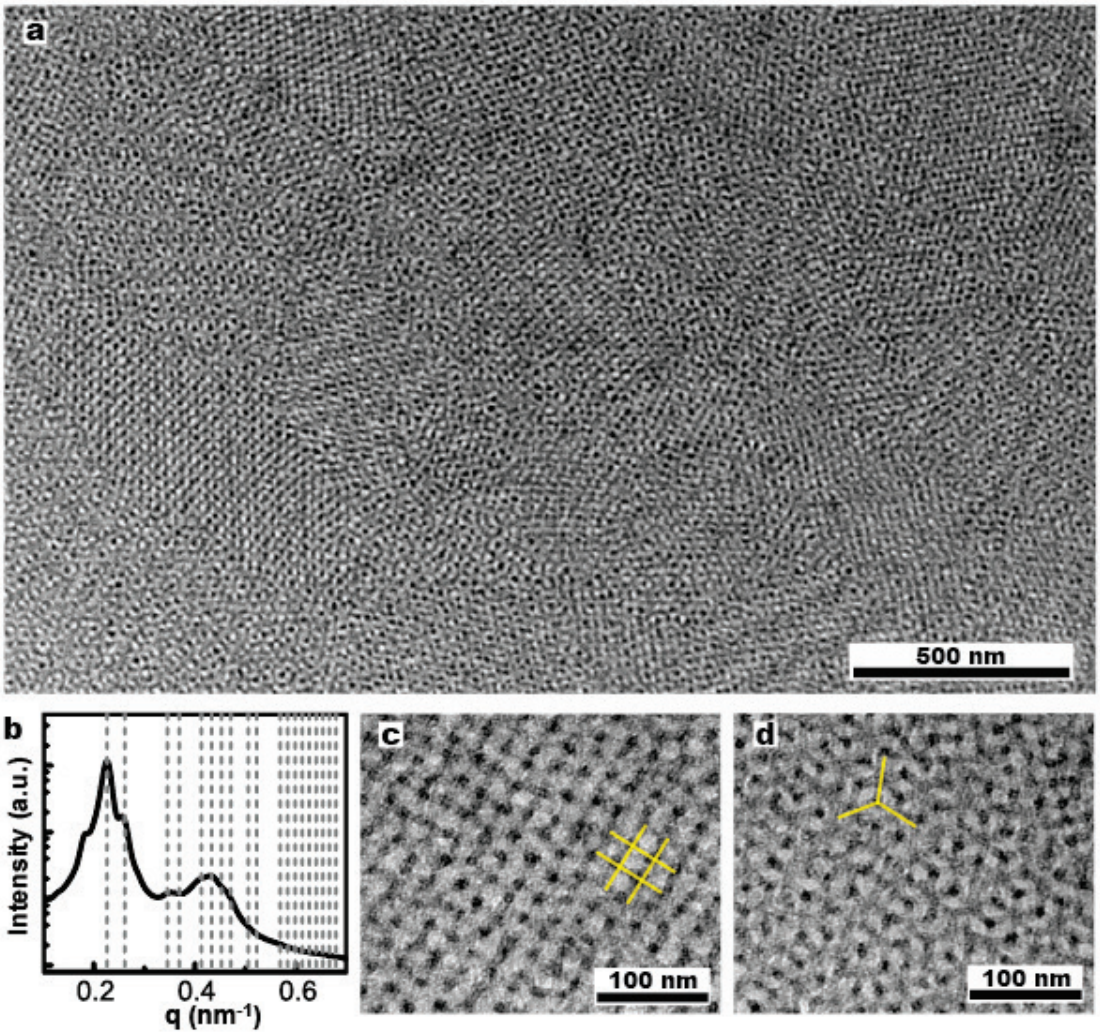

Figure 5.5. Representative bright field TEM images (a,c,d) for ISO2-T1 composite and the corresponding radially integrated 1D SAXS pattern indexed for a double gyroid structure (Q230). Dark strut domains represent O+oxide domains while the light parts are domains of I and S blocks. The estimated grain size of this highly ordered titania network is about or greater than 500 nm (a). The 4-fold symmetry (c) and wagon-wheel or 3-fold symmetry (d) projections are indicative of the (100) and (111) planes of the double gyroid morphology, respectively.

Table 5.3. Composition and morphology of ISO2-TiO_2 hybrid material

	volume fraction[a]			weight fraction		d-spacing
	I	S	O+Oxide	of oxide	morphology	(nm)
ISO2-T1	0.435	0.319	0.246	0.210	Q230	68.1

[a]The volume fractions for this sample were calculated based on the previously reported density of titania sols (1.8 g/cm3) [7].

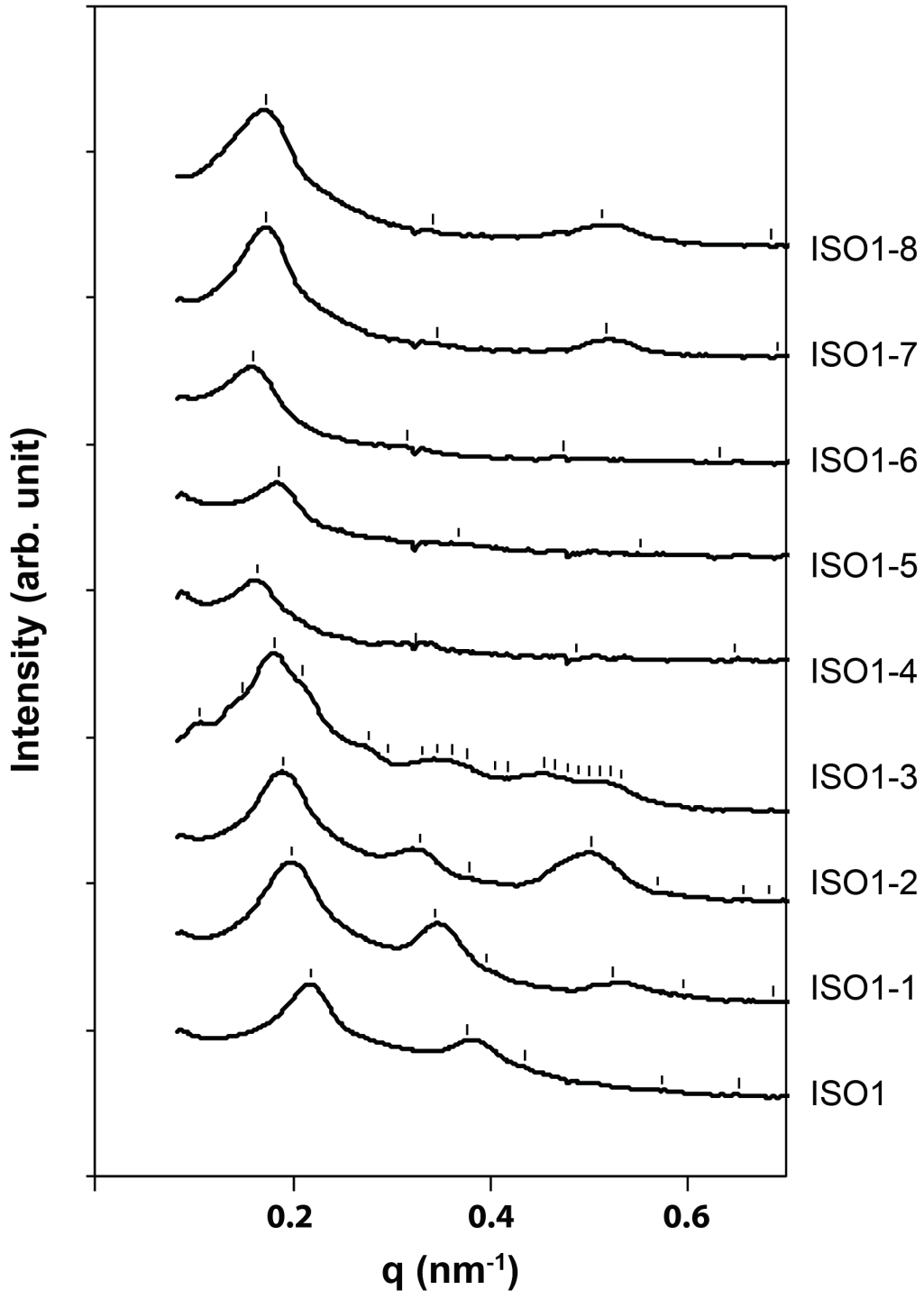

Figure S1. The SAXS patterns of ISO1 and aluminosilicate composites.

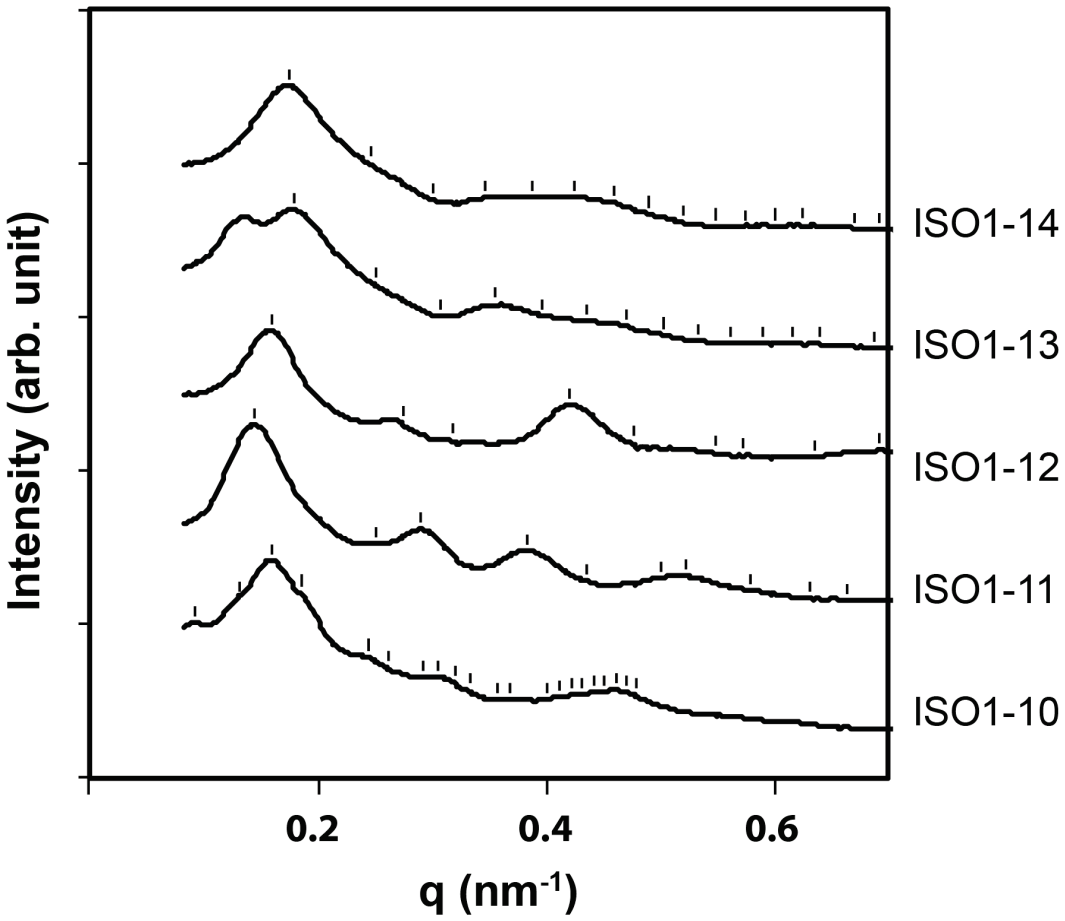

Figure S1. (Continued)

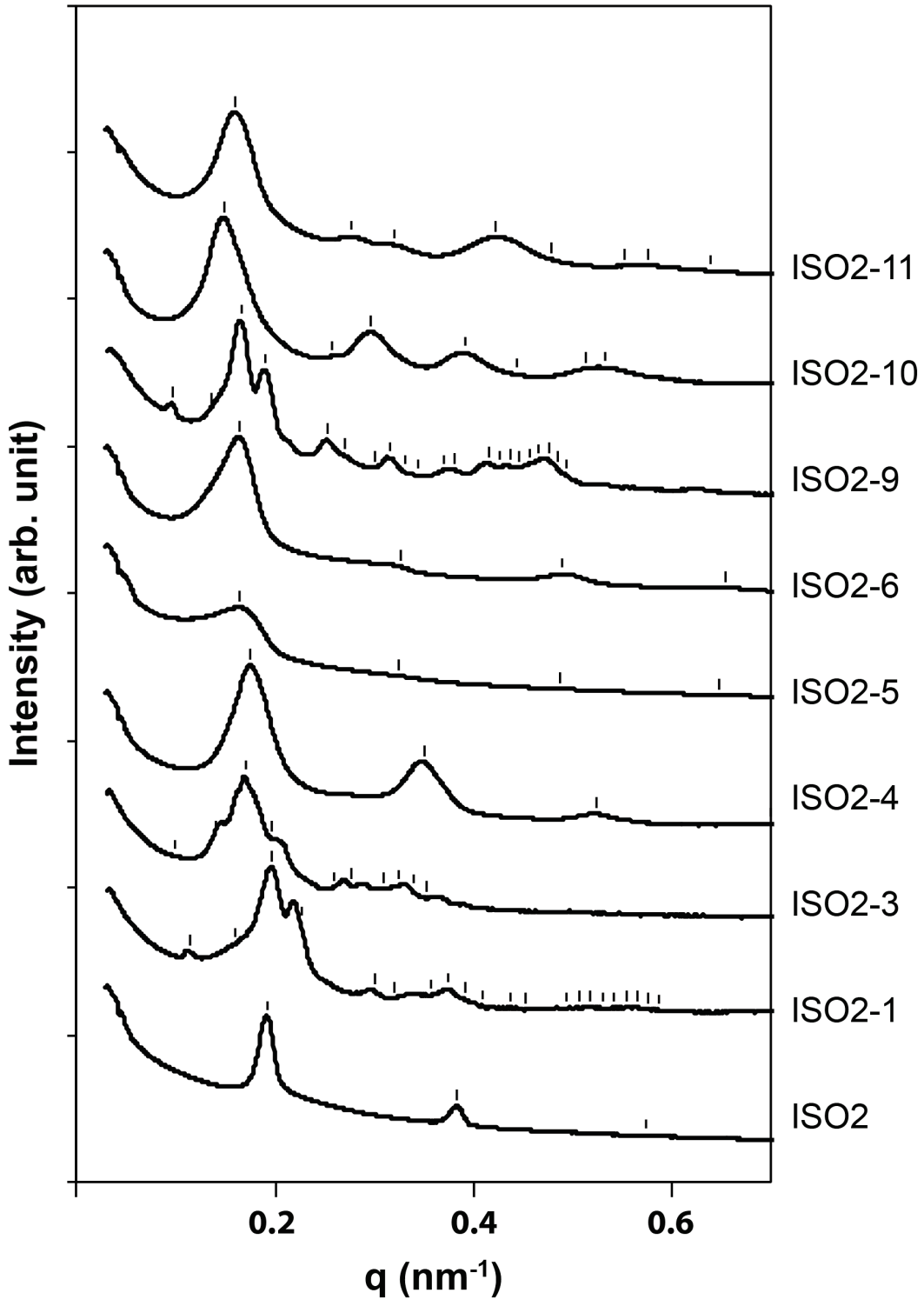

Figure S2. The SAXS patterns of ISO2 and aluminosilicate composites.

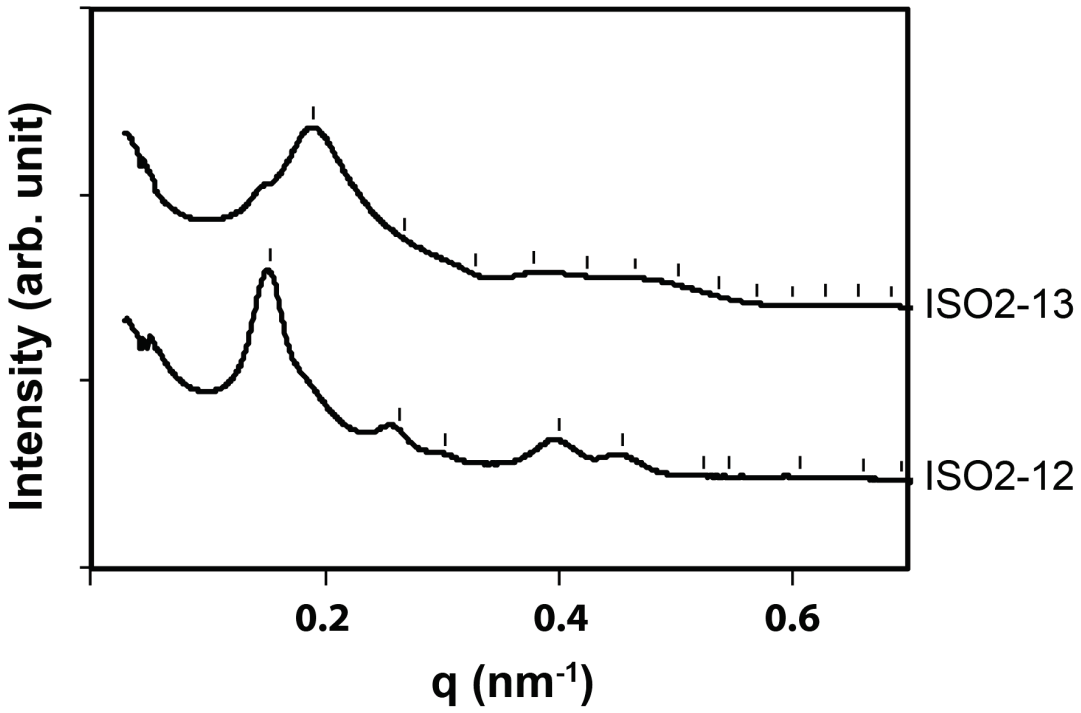

Figure S2. (Continued)

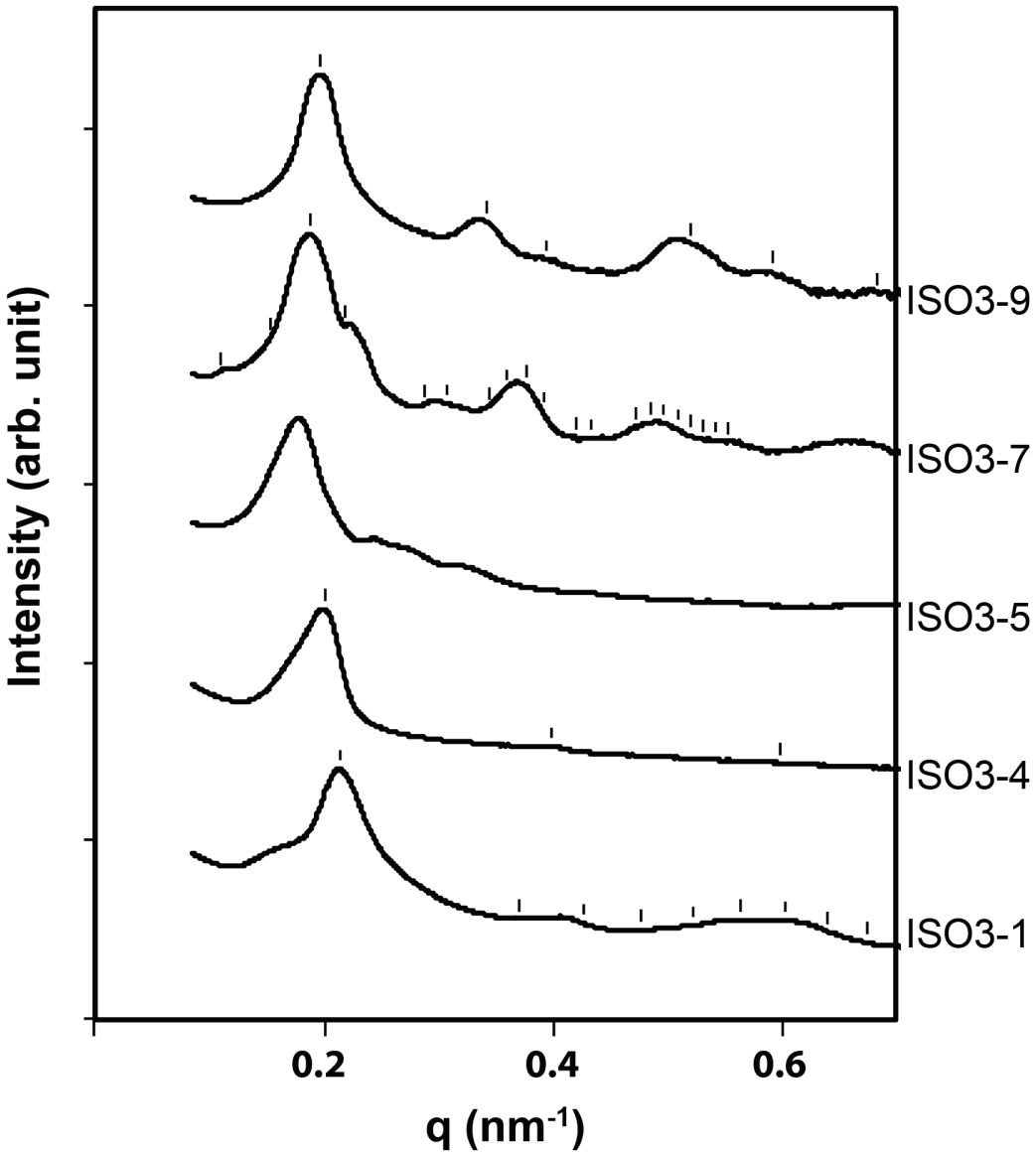

Figure S3. The SAXS patterns of ISO3 and aluminosilicate composites.

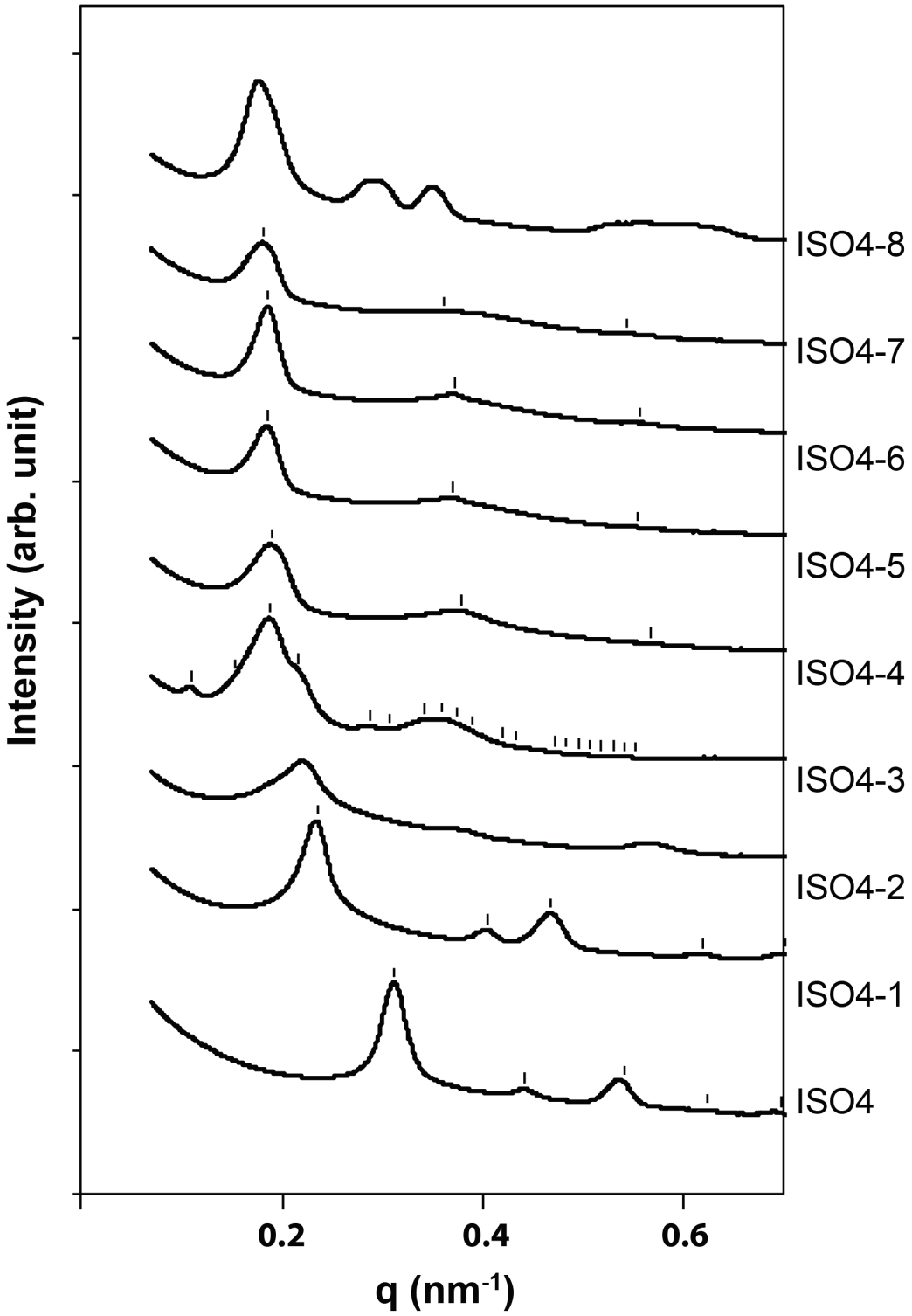

Figure S4. The SAXS patterns of ISO4 and aluminosilicate composites.

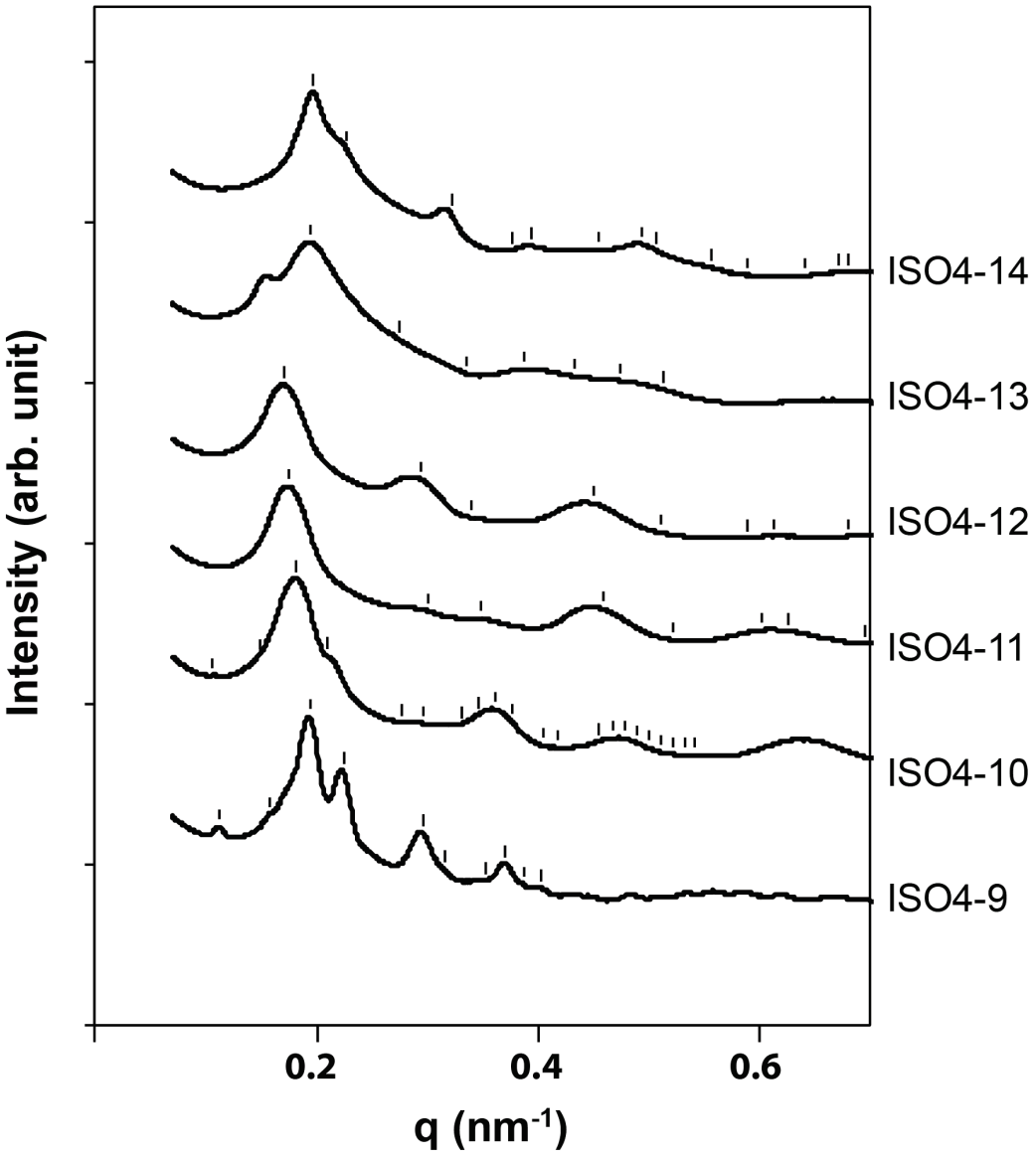

Figure S4. (Continued)

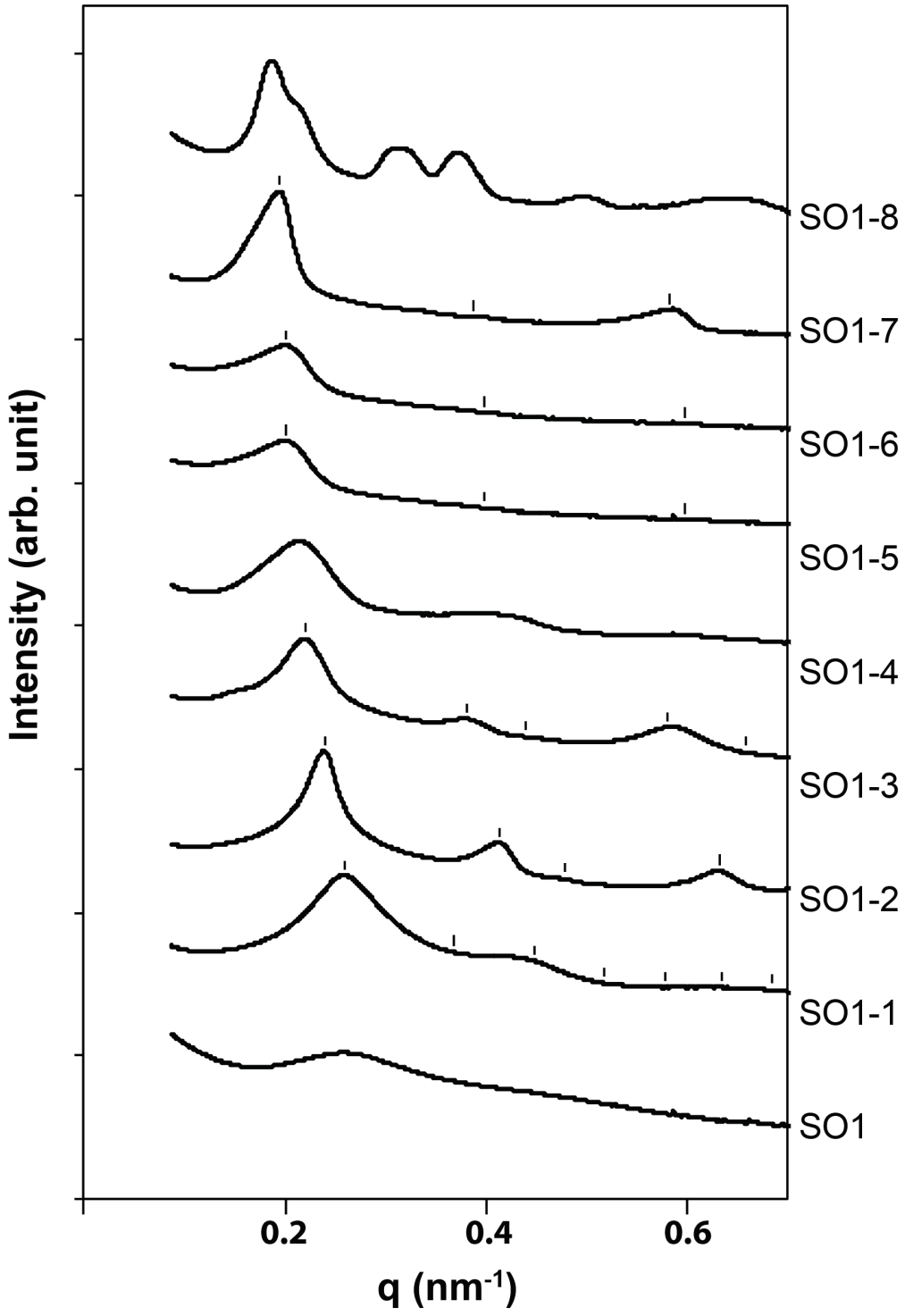

Figure S5. The SAXS patterns of SO1 and aluminosilicate composites.

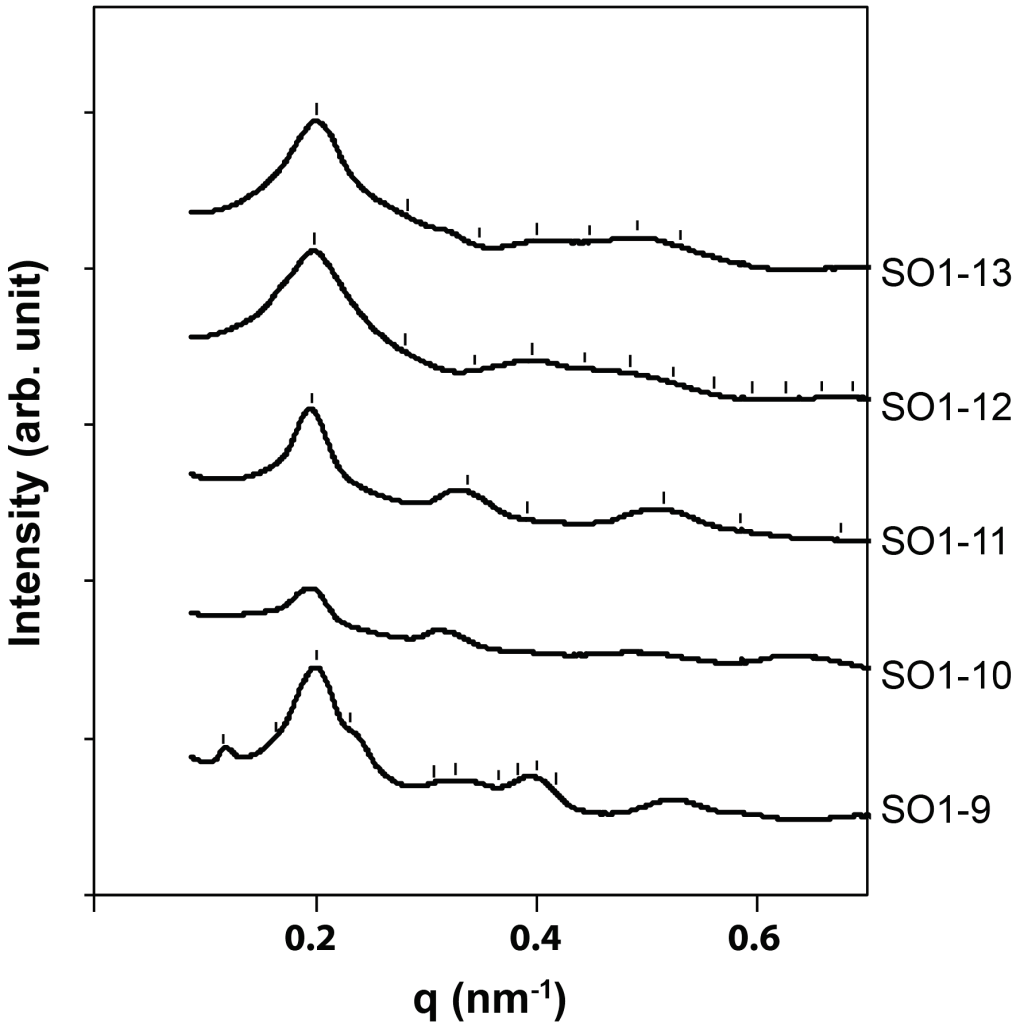

Figure S5. (Continued)

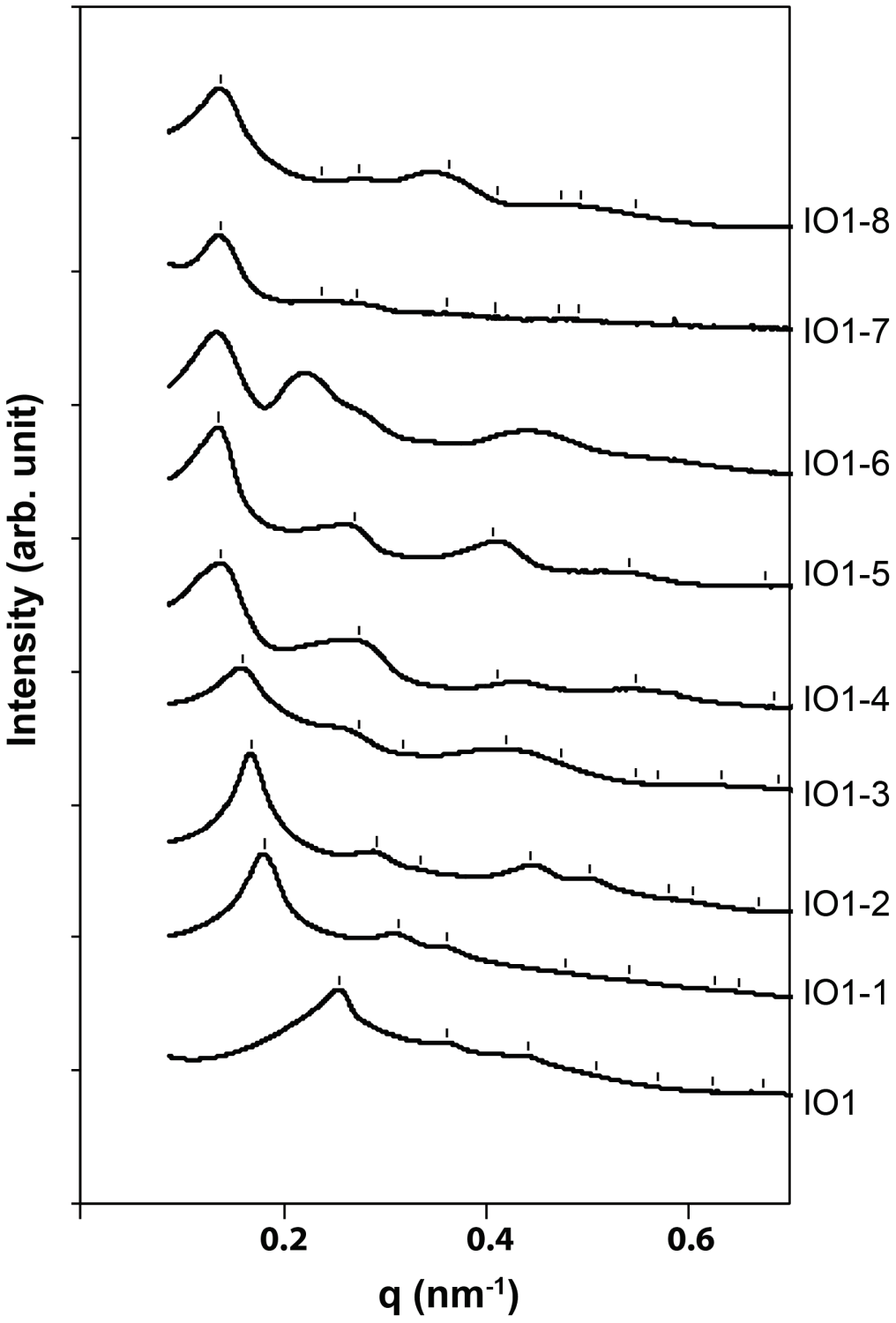

Figure S6. The SAXS patterns of IO1 and aluminosilicate composites.

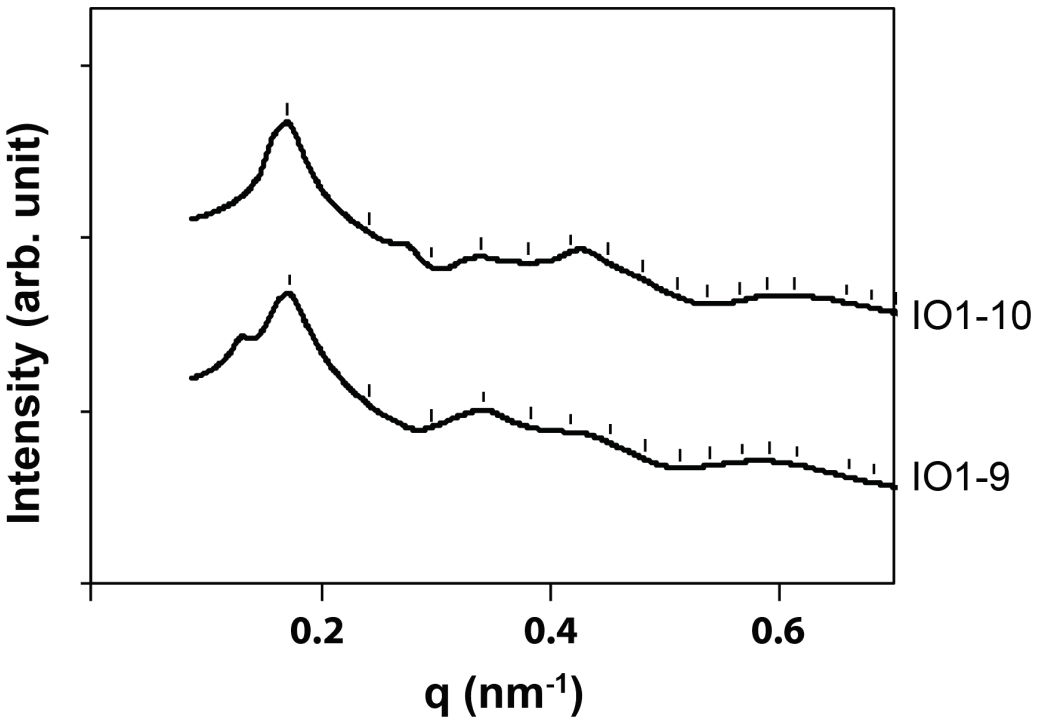

Figure S6. (Continued)

References

1. Bates, F.S., *Polymer-Polymer Phase-Behavior.* Science, 1991. **251**(4996): p. 898-905.
2. Bates, F.S. and G.H. Fredrickson, *Block Copolymer Thermodynamics - Theory and Experiment.* Annual Review of Physical Chemistry, 1990. **41**: p. 525-557.
3. Lazzari, M., G. Liu, and S. Lecommandoux, *Block copolymers in nanoscience*. 2006, Weinheim Chichester: Wiley-VCH ;John Wiley [distributor]. xix, 428 p.
4. Hamdoun, B., et al., *New nanocomposite materials.* Journal De Physique Ii, 1996. **6**(4): p. 493-501.
5. Warren, S.C., F.J. Disalvo, and U. Wiesner, *Nanoparticle-tuned assembly and disassembly of mesostructured silica hybrids.* Nature Materials, 2007. **6**(2): p. 156-U23.
6. Zhao, D.Y., et al., *Triblock copolymer syntheses of mesoporous silica with periodic 50 to 300 angstrom pores.* Science, 1998. **279**(5350): p. 548-552.
7. Alberius, P.C.A., et al., *General predictive syntheses of cubic, hexagonal, and lamellar silica and titania mesostructured thin films.* Chemistry of Materials, 2002. **14**(8): p. 3284-3294.
8. Templin, M., et al., *Organically modified aluminosilicate mesostructures from block copolymer phases.* Science, 1997. **278**(5344): p. 1795-1798.
9. Simon, P.F.W., et al., *Block copolymer-ceramic hybrid materials from organically modified ceramic precursors.* Chemistry of Materials, 2001. **13**(10): p. 3464-3486.
10. Renker, S., et al., *Nanostructure and shape control in polymer-ceramic hybrids from poly(ethylene oxide)-block-poly(hexyl methacrylate) and aluminosilicates derived from them.* Macromolecular Chemistry and Physics, 2004. **205**(8): p. 1021-1030.
11. Garcia, B.C., et al., *Morphology Diagram of a Diblock Copolymer-Aluminosilicate Nanoparticle System.* Chemistry of Materials, 2009. **21**(22): p. 5397-5405.
12. Antonelli, D.M. and J.Y. Ying, *SYNTHESIS OF HEXAGONALLY PACKED MESOPOROUS TIO2 BY A MODIFIED SOL-GEL METHOD.* Angewandte Chemie-International Edition in English, 1995. **34**(18): p. 2014-2017.
13. Oskam, G., et al., *The growth kinetics of TiO2 nanoparticles from titanium(IV) alkoxide at high water/titanium ratio.* Journal of Physical Chemistry B, 2003. **107**(8): p. 1734-1738.
14. Yang, P.D., et al., *Generalized syntheses of large-pore mesoporous metal oxides with semicrystalline frameworks.* Nature, 1998. **396**(6707): p. 152-155.

15. Orilall, M.C. and U. Wiesner, *Block copolymer based composition and morphology control in nanostructured hybrid materials for energy conversion and storage: solar cells, batteries, and fuel cells.* Chemical Society Reviews, 2011. **40**(2): p. 520-535.

16. Orilall, M.C., et al., *One-Pot Synthesis of Platinum-Based Nanoparticles Incorporated into Mesoporous Niobium Oxide-Carbon Composites for Fuel Cell Electrodes.* Journal of the American Chemical Society, 2009. **131**(26): p. 9389-9395.

17. Lee, J., et al., *Direct access to thermally stable and highly crystalline mesoporous transition-metal oxides with uniform pores.* Nature Materials, 2008. **7**(3): p. 222-228.

18. Smarsly, B., et al., *Highly crystalline cubic mesoporous TiO2 with 10-nm pore diameter made with a new block copolymer template.* Chemistry of Materials, 2004. **16**(15): p. 2948-2952.

19. Wan, J.L., et al., *Nanostructured non-oxide ceramics templated via block copolymer self-assembly.* Chemistry of Materials, 2005. **17**(23): p. 5613-5617.

20. Kamperman, M., et al., *Ordered mesoporous ceramics stable up to 1500 degrees C from diblock copolymer mesophases.* Journal of the American Chemical Society, 2004. **126**(45): p. 14708-14709.

21. Warren, S.C., et al., *Ordered mesoporous materials from metal nanoparticle-block copolymer self-assembly.* Science, 2008. **320**(5884): p. 1748-1752.

22. Li, Z.H., et al., *Metal Nanoparticle-Block Copolymer Composite Assembly and Disassembly.* Chemistry of Materials, 2009. **21**(23): p. 5578-5584.

23. Bailey, T.S., H.D. Pham, and F.S. Bates, *Morphological behavior bridging the symmetric AB and ABC states in the poly(styrene-b-isoprene-b-ethylene oxide) triblock copolymer system.* Macromolecules, 2001. **34**(20): p. 6994-7008.

24. Bates, F.S., *Network phases in block copolymer melts.* Mrs Bulletin, 2005. **30**(7): p. 525-532.

25. Chatterjee, J., S. Jain, and F.S. Bates, *Comprehensive phase behavior of poly(isoprene-b-styrene-b-ethylene oxide) triblock copolymers.* Macromolecules, 2007. **40**(8): p. 2882-2896.

26. Epps, T.H., et al., *Ordered network phases in linear poly(isoprene-b-styrene-b-ethylene oxide) triblock copolymers.* Macromolecules, 2004. **37**(22): p. 8325-8341.

27. Meuler, A.J., M.A. Hillmyer, and F.S. Bates, *Ordered Network Mesostructures in Block Polymer Materials.* Macromolecules, 2009. **42**(19): p. 7221-7250.

28. Tyler, C.A., et al., *SCFT study of nonfrustrated ABC triblock copolymer melts.* Macromolecules, 2007. **40**(13): p. 4654-4668.

29. Bailey, T.S., et al., *A noncubic triply periodic network morphology in poly(isoprene-b-styrene-b-ethylene oxide) triblock copolymers.* Macromolecules, 2002. **35**(18): p. 7007-7017.

30. Floudas, G., et al., *Poly(ethylene oxide-b-isoprene) diblock copolymer phase diagram.* Macromolecules, 2001. **34**(9): p. 2947-2957.

31. Crossland, E.J.W., et al., *A Bicontinuous Double Gyroid Hybrid Solar Cell.* Nano Letters, 2009. **9**(8): p. 2807-2812.

32. Bruce, P.G., B. Scrosati, and J.M. Tarascon, *Nanomaterials for rechargeable lithium batteries.* Angewandte Chemie-International Edition, 2008. **47**(16): p. 2930-2946.

33. Guo, Y.G., J.S. Hu, and L.J. Wan, *Nanostructured Materials for Electrochemical Energy Conversion and Storage Devices (vol 20, pg 2878, 2008).* Advanced Materials, 2008. **20**(23): p. 4384-4384.

34. du Sart, G.G., et al., *Nanoporous Network Channels from Self-Assembled Triblock Copolymer Supramolecules.* Macromolecular Rapid Communications, 2011. **32**(4): p. 366-370.

35. Docampo, P., et al., *Triblock-Terpolymer-Directed Self-Assembly of Mesoporous TiO2: High-Performance Photoanodes for Solid-State Dye-Sensitized Solar Cells.* Advanced Energy Materials, 2012. **2**(6): p. 676-682.

36. Stefik, M., et al., *Ordered Three- and Five-ply Nanocomposites from ABC Block Terpolymer Microphase Separation with Niobia and Aluminosilicate Sols.* Chemistry of Materials, 2009. **21**(22): p. 5466-5473.

37. Stefik, M., et al., *Networked and chiral nanocomposites from ABC triblock terpolymer coassembly with transition metal oxide nanoparticles.* Journal of Materials Chemistry, 2012. **22**(3): p. 1078-1087.

38. Toombes, G.E.S., et al., *Hexagonally patterned lamellar morphology in ABC triblock copolymer/aluminosilicate nanocomposites.* Chemistry of Materials, 2008. **20**(10): p. 3278-3287.

39. Toombes, G.E.S., et al., *Self-assembly of four-layer woodpile structure from zigzag ABC copolymer/aluminosilicate concertinas.* Macromolecules, 2008. **41**(3): p. 852-859.

40. Fetters, L.J., et al., *Connection between Polymer Molecular-Weight, Density, Chain Dimensions, and Melt Viscoelastic Properties.* Macromolecules, 1994. **27**(17): p. 4639-4647.

41. Finnefrock, A.C., et al., *The plumber's nightmare: A new morphology in block copolymer-ceramic nanocomposites and mesoporous aluminosilicates.* Journal of the American Chemical Society, 2003. **125**(43): p. 13084-13093.

42. Hur, K., et al., *Predicting Chiral Nanostructures, Lattices and Super lattices in Complex Multicomponent Nanoparticle Self-Assembly.* Nano Letters, 2012.

12(6): p. 3218-3223.